The Theory of Everything

Foundations, Applications and Corrections to General Relativity

Michael Scott Peck

Original: July 24th, 2012 | Final: May 20th, 2013 | Copyright 2013 | Contact

Abstract: Corrections to general relativity are derived from classical theory and applied to the standard model. The perspective offered is the conceptual inverse of Einstein's theory, where particles exist as localized fields. These vacuum fields undergo affine transformations that are locally invariant with respect to the space-time metric. It is demonstrated that the proper vacuum solution to the Einstein-Maxwell field equations is the limit of the single particle vacuum field solution. The existence of event horizon within Einstein's field equations is linked to the application of point-like sources in the local field theory. With vacuum field theory, it is observed that event horizon can no longer form without infinite classical energy. Gravitational waves are also discussed relative to the use of point-like sources in Einstein's field equations and similar geometric field theories. Methods for determining the space-time metric of any object on a per particle basis are provided. The continuous model of the universe is further introduced, where the solutions to several grand cosmological problems are discussed. It is demonstrated that an asymptotically flat universe will appear linear with respect to local observers. The inferred accelerated expansion is an illusion due to local geodesics deflecting towards the center of an asymptotically flat, linear universe. With recent constraints on the abundance of faint blue galaxies and observed evolution, ΛCDM is found to be off in galactic number densities by $70\% \pm 15\%$ and $104\% \pm 25\%$ at $0.5z$ and $1.0z$ respectively. These galaxies are also observed to be similar to local disk and irregular populations, where ΛCDM underestimates their size by $200\% - 300\%$ prior to $0.7z$. This implies that an expanding model predicts the incorrect shape of the universe, which induces systematic lensing errors. After eliminating all viable explanations, an expanding universe is conclusively ruled out. The purposed model however agrees with all observations by applying only classical assumptions. The shape of the universe for example supports a central core, which is responsible for the cosmic background radiation. It is further argued that Einstein's field equations are incompatible with such universe due to predictions of event horizon.

Table of Contents

Preface

Due to the diversity of subjects discussed, this page is meant to provide an overview of the paper. The two theories included herein are referred to as vacuum field theory and the continuous model of the universe. These deeply interrelated theories are necessary for complete consistency between general relativity and cosmology. The cosmological aspects are further applied to rule out various theories of general relativity. The foundations of vacuum field theory arise from three postulates with respect to a unified field theory. These postulates however are only introduced for additional insight, as vacuum field theory can be derived from classical laws of physics. The first is a $1/r$ gravitational potential for any particle, e.g. an electron or proton. The second is Einstein's equivalence principle, where a particle in one local frame will be identical to itself in any other local frame.

Rather than particles being point-like sources, it is argued that they instead exist as localized fields throughout chapters **1** and **2**. The foundations of vacuum field theory can be viewed in terms of waves travelling through a relative medium. The medium is an energy density with respect to the localized field interpretation of particles. It is demonstrated that the gravitational and electric potential of a charged, non-composite particle are directly proportional to vacuum energy density. After applying the Lorentz transformation to $1/r$ fields, deceleration of a charged particle is directly related to a change in vacuum energy density in the form of bremsstrahlung. The field dynamics within classical electrodynamics are mimicking those of vacuum field theory. It is therefore possible to formulate theories with point-like sources that agree with observations. The underlying vacuum energy density however defines a locally isotropic space-time metric for general relativity. It would therefore be incorrect to treat the space-time metric as an additional medium for the continuum limit of point-like sources to influence. By knowing how each particle's field varies due to the background field induced by all others in consideration, the effective space-time metric can be determined for objects on a per-particle basis. With the per-particle method provided in chapter **2**, it is observed that conical singularities or event horizon can no longer form without infinite energy. The application of point-like sources and coupling to space-time metric is responsible for the predictions of event horizon and gravitational waves in modern general relativity. Direct proof for the localized nature of particles will therefore arise from a null detection of gravitational waves with direct methods. Although a null result would invalidate the coupling of point-like sources to a space-time metric, the cosmological aspects already rule out any theory that allows event horizon from finite energy.

The cosmological model is the central discovery of this paper, where it is demonstrated that the universe is asymptotically flat. In other words, the inferred accelerated expansion is an illusion due to local geodesics deflecting towards the center of the universe. With redshift arising from relative motion and gravitational potential, the observed state of the universe can only be fit by accelerated expansion or an asymptotically flat shape. All observations are further in agreement with a linear, asymptotically flat universe as discussed throughout chapter **3**. These include galactic number densities, angular size versus the absolute magnitude of faint blue galaxies and time-dependence. Although Hawking radiation is theorized to exist with respect to event horizon, the $3000\,K$ temperature of the cosmic background radiation would require the core to be many orders of magnitude less massive than the Moon. Countless galaxies and clusters are however continuously flowing towards the center of the universe. The central core must therefore be more massive than any local object, i.e. the observed cosmic background radiation offers direct proof against the existence of event horizon.

1. Foundations

Throughout the history of modern physics, many attempts at developing a viable unified theory have been made. These attempts have diverse underlying principles, most lacking physical interpretation. Without providing the entire unified field theory, it is possible to reformulate general relativity with three fundamental postulates. These postulates are derived from classical principles, which are further discussed relative to the standard model and Einstein field equations (EFE). Methods are derived that allow the effective space-time metric of any object to be determined. These require a revision of general relativity for several reasons, which are discussed throughout the first and second chapters.

(**1**) EFEs are based upon a continuum limit of point-like sources, which act locally on the space-time metric. The metric is in return mimicking the localized nature of particles; i.e. similar to classical electrodynamics, space-time acts as a medium for waves. However, the actual field general relativity depicts is the underlying vacuum energy density. This includes contributions from classical and semi-classical fields, although only the electromagnetic field is thoroughly discussed herein. It is argued that the principle of locality is invalid and particles exist as localized field rather than point-like objects.

(**2**) Special relativity demands that a particle's field will deform from variations in relative motion. General relativity should be restricted to similar mechanisms. When multiple particles interact, the field of each is deformed due to its locally invariant nature with respect to the space-time metric.

(**3**) All massive particles are known to display electromagnetic behavior; however, EFEs decouple mass from the electromagnetic field. Therefore, the Schwarzschild solution cannot represent realistic objects, as even neutrons display non-zero magnetic dipole moments and electromagnetic form factors.

Postulate I: Classical forces are mathematical constructs, approximating the time dependence of vacuum fields. At this introductory level of vacuum field theory, the focus is directed at both classical and free field force(s). Classical force is a time-dependent variation that acts upon a point-like particle. Regardless if the discussion is general relativity or electrodynamics, force determines the time-dependence of momentum and position. Some theories also produce abstract fields that are related to position and momentum. For example, quantum mechanics provides probabilistic wave functions of an underlying semi-classical system.

In a free field theory, force refers to the action at each point in space; this is not necessarily in a classical sense. For example, say a field existed that represented a single electron. Regardless of the underlying complexity, the electron will have a classical location in space. In addition to the finite energy density at the particle's classical position, all other points in space will have finite energy density. The introduction of another electron displaced from the original would further vary the underlying field at all points in space. The force(s) between these two localized fields arise from the infinitesimal action of the effective field at each point in space. Particles are therefore localized entities displaying action at a distance.

References to quantization throughout this paper refer to reducing the localized nature of particles to point-like objects. Classical forces are then applied to determine the time dependence of position and momentum in quantum systems. This is achieved by applying the Lorentz transformation or space-time metric to a scalar field; the scalar field is related to vacuum energy density. The vacuum energy density of a single particle can further be approximated with classical theory, i.e. $1/r$.

Postulate II: All particles consist of localized vacuum fields. This is relevant to the concept of field-particle duality, where all particles display decaying fields and point-like structure. Under the most fundamental considerations, objects would cease to exist if matter was not localized. This concept can further be extended to what it means for a field to be localized. Localization requires that the underlying energy is self-reinforced, i.e. any stable vacuum field will not dissipate over time. For this to be plausible, at least two forms of field energy must exist. A complex scalar-vector field is defined below; however, this is inadequate for an interacting theory. Additional degrees of freedom are instead required for time-dependent evolution. The main objective of this paper is to bridge the gap between electrodynamics and general relativity. These additional degrees of freedom can therefore be ignored by applying classical forces.

Vacuum energy density is related to a complex scalar-vector field ψ that is conserved throughout interactions. Due to this conservation, the envelope of fields can be approximated with linear wave-like equations. Furthermore, classical physics requires for the far-field of massive particles to decay as E_0/r in Planck units; this is later discussed in section (**1.3**). With the wave function $\psi = \emptyset + i\vec{v}$, a complex Helmholtz equation (**1**) is needed. It is superficially similar to the Schrodinger equation of a free particle, but does not depict probability.

$$(\nabla^2 + k^2)\psi = 0 \tag{1}$$

Equation (**1**) can be divided into both real (**2**) and imaginary (**4**) parts.

$$(\nabla^2 + k^2)\emptyset = 0 \tag{2}$$

In spherical coordinates, solutions to (**2**) involve spherical harmonics and Bessel functions (**3**).

$$\emptyset_{lm} = j_l(kr)Y_{lm}(\theta, \varphi) \tag{3}$$

The complex component of equation (**1**) takes a similar form (**4**).

$$(\nabla^2 + k^2)\vec{v} = 0 \tag{4}$$

Solutions to (**4**) can be determined from the scalar component via (**5**).

$$\vec{v}_{lm} = \frac{1}{k}\nabla\emptyset_{lm} \tag{5}$$

Conservation of vacuum energy can be achieved by introducing the continuity equations (**6**) and (**7**). These relate to an underlying geometric structure after reducing the additional degrees of freedom. The equations however do not depict the correct time dependence of vacuum fields, which can instead be approximated with classical theory. All that is required after the quantization of a localized field is the Lorentz transformation and assumption of $1/r$ gravitational potentials. The application of a single scalar-vector field is important due to the quantization process. It is therefore assumed that $\emptyset$ remains constant at the classical position of a massive, non-composite particle. These variables are further related to a scalar invariant and motion of a point contained within $\mathbb{R}^3$.

$$\frac{1}{c}\frac{d\emptyset}{dt} = -\nabla \cdot \vec{v} - \|\nabla\emptyset\| \tag{6}$$

$$\frac{1}{c}\frac{d\vec{v}}{dt} = \nabla\emptyset + (\nabla \cdot \vec{v})\hat{v} \tag{7}$$

The complex Hamiltonian density ψ defines the vacuum energy density at any point in space with a quaternion norm (**8**).

$$\mathbb{V}(r) \equiv \sqrt{\psi\psi^*} = \sqrt{(\emptyset)^2 + (v)^2} \tag{8}$$

The linear wave solutions can be quantized with equation (**9**), i.e. the point of maximum field energy depicts the classical energy.

$$E \equiv \int_0^\infty \sqrt{\psi\psi^*}\delta(r)dr \tag{9}$$

Postulate III: The vacuum field is the result of transforming the non-linear geometric degrees of freedom. A crucial metaphysical aspect of matter is usually overlooked in modern physics, i.e. what do particles physically consist of? Initial attempts tried to attribute a physical substance to matter, or material upon space that formed particles. However, this perspective is plagued by cyclic reasoning, i.e. if such substance existed, what would be the physical essence of it? Indeed this reasoning is no different from the modern concept of fields. For example, electromagnetic fields are mathematical constructs created in abstract to understand the universe at the quantized level. At any scale however, one fundamental property of the universe is undeniable; i.e. space itself.

In the classical perspective space is a rigid, time-independent structure that quantized mechanics is founded upon. Switching to the more abstract view of general relativity, the properties of space vary from the Euclidean model. It becomes possible to deform space, varying the location of a continuum of points in a smooth manner. However, Einstein's view of relativity is incompatible with quantum mechanics and the cosmological model discussed in chapter **3**. He also applied the only physical property of the universe to a single classical force, i.e. gravity. It is demonstrated in section (**1.4**) that general relativity can be reinterpreted as a tool for quantization. Einstein's perspective is therefore the conceptual inverse of vacuum field theory. This opens a profound path to unification, as an underlying geometric structure can be used to depict all classical forces. Therefore, unification no longer refers to the energy scale where classical forces merge into one, but instead the manifestation of all forces from a single unified field. The essence of matter can now be attributed to something that is physically real rather than a mathematical construct.

Assuming tensors and/or a geometric foundation are capable of fulfilling the first two postulates, the necessity for additional degrees of freedom is clear. The vacuum field represents the energy of an underlying geometric structure, although the actual structure is beyond this papers scope. Regardless, acknowledging its existence offers an intuitive explanation for the universe. It is trivial that a geometric structure should be time-dependent if it does exist. Therefore, in the most general sense matter is nothing more than fluctuations of space itself. These are much smaller than the macroscopic world, as vacuum field theory indicates structure at the Planck scale. Without assuming Planck scale fluctuations of space are responsible for fields and matter, there is literally no other way of writing a unified field theory. For example, the standard model applies several scalar-vector fields to complete symmetries and fill gaps; however, they are solely mathematical constructs.

As earlier theories developed, the original aether became a resistive medium throughout space rather than mysterious substance that formed particles. This transition was the product of the corpuscle theory of light, attributed to Newton. It was later argued against with the Michelson-Morrison experiment, which tested for a variation in the speed of light relative to the local motion of Earth. This concept of anisotropy is flawed, which had been pointed out by Hendrik Lorentz[A]. As an object's momentum varies in a local frame, the field is transformed in such a way that any anisotropic affects cancel. Motion is instead relative to the vacuum field of all other particles and aether only becomes conceptually crucial for a single particle universe. In other words, the scalar vacuum energy density creates a relative medium upon space, which must further be applied to determine the effective space-time metric.

1.1. Space

When describing the dynamics of particles in a gravitational field, general relativity is a useful theory. However, the theory can be interpreted in two unique perspectives. The first is the mainstream view, where the four-dimensional manifold is to be taken literally; i.e. the coupled entity of space-time physically exists. Gravitational acceleration within this perspective is not induced by the curvature of space, but instead the curvature of time. The curvature of spatial components only varies the path of particles in motion or under classical force. Regardless, the physical existence of space-time is crucial for not only Einstein's interpretation, but also the validity of mainstream astronomy and cosmological models. The undermining of this perspective however originates from the predictions of singularities and gravitational waves. The use of quantized point sources in the geometric Laplace equation (EFEs) produces these artifacts. Particles instead exist as localized fields rather than point-like sources and must be treated as so.

The second view insists that the universe does not physically exist as a four-dimensional space-time manifold. Space and time should instead be treated as two independent entities; i.e. space is depicted by a classical manifold mapped to physical locations, while time is a manifestation of relativity or event comparison. Within this perspective, the vacuum field of each particle is relative to a Euclidean reference space ($\eta_{\mu\nu}$), which can be arbitrarily chosen. Upon this reference space or frame, particles exist as localized scalar-vector fields. Affine transformations are applied to the field of each particle rather than varying the metric of space, in agreement with the principles of special relativity and electrodynamics. Any reference space is further held static so that it does not allow metric or gravitational waves.

In differential geometry, a metric is defined that maps all points (ξ^{α}) bound to a manifold in space to a curvilinear coordinate system (x^{α}), or vice-versa. This can be defined as an infinitesimal variation in distance between two points in space, with respect to the original configuration. A two dimensional example is depicted in figure 1.1. It is always valid to vary the points on a manifold as long as they never overlap; this is referred to as a Riemann manifold. This deformation is possible due to the infinitesimal property of nature, i.e. there exist an infinite number of infinitesimal intervals between two points in space.

In another perspective or the one previously argued for is the deformation of a ruler, which consists of a linear lattice of atoms. These atoms contain many quantized particles, although each is relatively localized at a single point in space. When vacuum energy density increases, each particle's field must remain locally invariant with respect to the space-time metric. The space-time metric is therefore encoding the deformations or affine transformations experienced by localized fields, which can further be treated as point-like objects. In a situation where the gravitational potential is increasing with respect to time, distance from the perspective of the ruler remains constant. However, an observer in the reference space will note that length contraction of the ruler has taken place. Only the lattice of atoms becomes deformed with respect to the reference state rather than space itself.
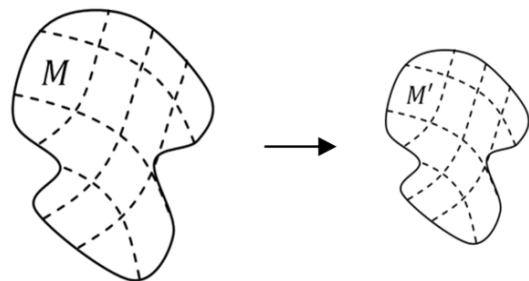
Figure 1.1. A smoothly connected manifold (M) is transformed from an initial state (M) to a final state (M').

1.2. Time

Quantization or the transformation of a localized field into a point-like object allows for the creation of systems. A system exists in a finite region of space and may contain many quantized particles, usually coupled to kinematic equations. Therefore, systems are time-dependent and obey classical energy conservation, i.e. Lagrangian formulations. Within classical mechanics, the trajectory of a particle through a potential can be determined with the Lagrangian equation (**10**); where L is the kinetic energy minus potential.

$$\frac{d}{dt}\left(\frac{\partial L}{\partial \dot{q}_i}\right) - \frac{\partial L}{\partial q_i} = 0 \qquad (\mathbf{10})$$

The 1-dimensional Lagrangian can be written as (**11**), where V is the classical potential.

$$L = \frac{1}{2}m_0\dot{x}^2 - V(x) \qquad (\mathbf{11})$$

In this perspective, time is a comparative scalar related to a change in position with respect to some constant rate of observation. It allows for a coupling between quantized energy and the rate at which quantized fields move through space.

Relativity introduces additional complexity as the rate of observation can vary between different scenarios. Both special and general relativity require a Lorentz scalar, where an increase in vacuum energy density forces a field to evolve at a decreased rate. This time dependence of classical variables is seen throughout various phenomenon including decay rates, classical kinematics and intrinsic spin. For example, it is experimentally known that an unstable particle has a relatively longer half-life when moving with respect to a background field. Particle decay depends upon internal degrees of freedom, which cannot be explained by classical mechanics. The longer half-life is instead modeled by relativity, where all variables evolve at a decreased rate. When quantum mechanics is discussed, it is demonstrated that the intrinsic spin rate of an electron also decreases as vacuum energy density increases. The Dirac equation is further related to relativistic field dynamics, discussed throughout section (**1.6**). It is clear that time is more fundamental than the kinematics of point particles, i.e. time is a scalar quantity that depicts change in abstract variables.

Under certain conditions, it is possible for time to be undefined. If no energy exists, then there is nothing to compare and space at all scales becomes Euclidean ($\eta_{\mu\nu}$). The other extreme is a region of infinite vacuum energy density such as an event horizon or conical singularity. Time in this situation is undefined because the underlying field(s) cannot evolve. At this limit, quantum mechanics fails under classical considerations since the observables become static. Einstein's field equations allow such anomalies due to the use of point-like sources in a local geometric field theory. This results in the non-linearity between vacuum energy density and space-time metric. The only way to produce infinite vacuum energy density in vacuum field theory is with infinite classical energy, which is impossible.

EFEs are more abstract with respect to time, or space-time. For example, time-dependent variations in the stress-energy tensor can produce gravitational waves. By applying quantized mass and momentum in such a local field theory, the field of point-like sources becomes geometric in nature. EFEs provide the framework to determine the time dependence of these localized fields, in which some scenarios allow quantized variables to be transformed into geometric waves. General relativity is however depicting the vacuum energy density of field(s) responsible for classical forces. Time in a more general sense is therefore a comparative scalar between the various variables of a quantized system or underlying field theory.

1.3. Energy

Effective energy is defined from quantized rest mass and momentum (**12**).

$$E = \sqrt{(pc)^2 + (m_0 c^2)^2} \qquad (12)$$

Returning to the classical wave-like equation (**1**), effective energy can also be written as a quaternion norm. With a particle's scalar-vector field (ψ), quantized energy is related to the vacuum energy density (**13**). From the third axiom, this density is related to the underlying geometric degrees of freedom. The goal is to transform the non-linear geometric structure into a scalar-vector field that is linearly proportional to classical energy.

$$\nabla(r) \equiv \sqrt{\psi\psi^*} \qquad (13)$$

In order to quantize the vacuum field, similar methods are applied with respect to the linear wave approach (**9**); i.e. applying a Dirac delta defines quantized energy (**14**).

$$E \equiv \int_0^\infty \nabla(r)\delta(r)dr \qquad (14)$$

The wave function can be written as (**15**), where quantized mass depicts the scalar field and momentum replaces the vector component. Scalar mass no longer exists solely at the particle's center, as it is a fundamental part of all field solutions.

$$\psi(0) \propto c^2 m_0 + ic\vec{p} \qquad (15)$$

With the quaternion norm used to define vacuum energy, it possible for scalar mass to be negative. Relative to the Dirac equation, the charge conjugate is applied to ensure only positive mass exists. Negative scalar mass however always results in positive vacuum energy density, which depicts the gravitational force. Thus ∇ will always be positive and the quantized scalar field will have the same sign as charge for non-composite massive particles.

With the second axiom and the expected inverse distance far-field, a spherically symmetric solution is possible. This is derived from the classical wave-like equation and is only meant to approximate the field's envelope. After applying spherical Bessel functions, two linear wave solutions are found for non-composite particles in Planck units (**16**). These solutions have an E_0/r far-field with energy density at the classical position proportional to E_0.

$$\nabla(r) = E_0 \sqrt{\left(\pm\frac{\sin(r)}{r}\right)^2 + \left(\mp\frac{\sin(r)}{r^2} \pm \frac{\cos(r)}{r}\right)^2} \qquad (16)$$

The approximate wavelength that corresponds to an electron or positron is therefore 2π in Planck units. In SI units however the wavelength is $2\pi l_p$, where Planck length is defined as (**17**).

$$l_p = \sqrt{\frac{\hbar c_0}{\Delta}} \cong 1.616199 \cdot 10^{-35} \, m \qquad (17)$$

As previously stated, the scalar-vector notation is not adequate for time-dependent evolution; i.e. (**16**) finds no real application beyond approximating the far-field vacuum energy envelope. In general, solutions for actual electrons and positrons are only approximated by equation (**1**) and the resulting linear solutions (**16**). All that is required by the purposed postulates is for vacuum energy density to be indefinitely localized in space, creating a stable $1/r$ far-field. Planck units are used due to a relation between the space-time metric and vacuum energy density. This effectively sets $G_0 = \hbar_0 = c_0 = k_e = k_B = 1$; i.e. the far-field gravity-electric potential of an electron is defined as (**18**), where σ is the charge to mass ratio. Classical energy variations from this potential are now directly proportional to variations in vacuum energy density or $\nabla \cong E_0/r$.

$$U = \nabla(1 \pm \sigma) \quad : \sigma = -15.15612(63)\frac{q_p}{m_p} \qquad (18)$$

Energy (**12**) can be reformulated by introducing the Lorentz scalar defined by (**19**), which is relative to a local frame of reference or space-time metric.

$$\gamma = \sqrt{1 + \left(\frac{v}{c}\gamma\right)^2} = \frac{1}{\sqrt{1 - \left(\frac{v}{c}\right)^2}} \tag{19}$$

The Lorentz factor scales rest energy, resulting in the effective quantized energy (**20**).

$$E = E_0 \gamma \tag{20}$$

The Lorentz factor (**19**) is simply the ratio of energy to rest energy, and has a range from 1 to ∞. For agreement between a relative and general frame, a scalar field γ_g is introduced. Generalization of γ_g is achieved by looking for a function similar to γ with a range from 1 to ∞. This is accomplished by first defining the reference vacuum energy density (**21**), which any observer will consistently measure as constant. Δ plays the role of E_0 as defined in (**20**), which is a product of quantized energy being proportional to vacuum energy density.

$$\Delta = \frac{c_0{}^4}{G_0} \tag{21}$$

The net vacuum energy density is defined as (**22**). There also exists a simple relation (**23**) between Δ and $\overline{\Delta}$ similar to $E = E_0 \gamma$.

$$\overline{\Delta} = \Delta + \nabla \tag{22}$$

$$\overline{\Delta} = \Delta \, \gamma_g \tag{23}$$

The domain can also be extended from 0 to ∞ when considering reference frames within a local field. However, all applications within this paper use a reference frame where the local source is removed ($r \to \infty$), or as $\nabla \to 0$. To ensure equivalence as previously purposed, the correct equation meeting all requirements is (**24**).

$$\gamma_g \equiv \frac{\overline{\Delta}}{\Delta} = 1 + \frac{\nabla}{\Delta} = \frac{1}{1 - \frac{\nabla}{\overline{\Delta}}} \tag{24}$$

Newtonian energy principles (**25**) can be derived by equating $\gamma_g = \gamma$. The general Lorentz scalar is defined relative to $\boldsymbol{\eta}_{\mu v}$, while the velocity within γ is with respect to $\boldsymbol{g}_{uv}$.

$$\frac{E}{E_0} = 1 + \frac{\Delta E}{E_0} = \frac{\overline{\Delta}}{\Delta} = 1 + \frac{\nabla}{\Delta} \tag{25}$$

Special relativity defines force as the change in proper momentum with respect to metric time (**26**). The following notation will be used for common variables; $u = d\boldsymbol{x}'/d\tau$ is proper velocity, $v = d\boldsymbol{x}'/dt'$ is metric velocity and $w = d\boldsymbol{x}/dt$.

$$\vec{f} = \frac{d\vec{p}}{dt'} = \frac{\gamma^3 m_0 v a}{c_0{}^2}\vec{v} + \gamma m_0 \vec{a} \tag{26}$$

The equations can be simplified by considering an object moving at escape velocity along the gradient of ∇. If ∇ is a single static particle, the escape velocity (**27**) relative to the particle's field is derived via $\gamma = \gamma_g$. Taking the limit of (**27**) as $r \to \infty$ is $\|\vec{v}\| = 0$, while the limit as $M \to \infty$ results in $\|\vec{v}\| = c_0$. When transforming (**27**) to the frame relative to a distant observer or Δ, the velocity as $M \to \infty$ is $\|\vec{w}\| = 0$ implying infinite vacuum energy density. This is a consequence of $\nabla \to \infty$ rather than $M \to \infty$.

$$\|\vec{v}\| = c_0 \sqrt{\frac{2G_0 M}{rc_0{}^2 + G_0 M} - \left(\frac{G_0 M}{rc_0{}^2 + G_0 M}\right)^2} \tag{27}$$

Acceleration is derived by differentiating (**27**) with respect to t' and applying the chain rule. The derivative with respect to r' can be transformed to r by applying another chain rule (**28**).

$$\frac{d}{dr'} = \frac{dr}{dr'}\frac{d}{dr} = \frac{1}{\gamma_g}\frac{d}{dr} \tag{28}$$

Acceleration relative to the space-time metric at escape velocity is therefore equal to (**29**).

$$a = \frac{d^2 r'}{dt'^2} = -\frac{G_0 M}{r^2 \gamma_g{}^4} \tag{29}$$

1.4. Continuum Mechanics

A localized field can be represented as a group of sections or wave fronts, where the space-time metric is applied for the quantization process. This reference to quantization is not with respect to quantum gravity, but instead the transformation of localized fields into point-like objects. From the perspective being argued within this paper, the proper view is that of localized fields deforming due to the presence of other localized fields. Classical mechanics are therefore replaced by continuum mechanics and resulting metric(s). For example, a finite manifold (M) can be equipped with an arbitrary metric ($g^{\mu\nu}$). The metric will then undergo affine transformations as depicted in figure 1.2. For simplicity, each manifold is smoothly connected and semi-rigid. Manifolds of this type are useful for describing vacuum fields, although the concept is further complicated by intrinsic spin. Relative to vacuum field theory, each particle exists as an independent manifold ($g^{\mu\nu}$) that is equipped with a scalar field. The scalar field or vacuum energy density is in return relative to the preferred reference frame. Each localized vacuum field also has a reference state (O) with respect to the space-time metric. With special relativity and classical electrodynamics, it is known that additional energy or momentum induces length contraction of the underlying field(s). This can be extended to general relativity by applying the spatial components of the contravariant metric tensor. Figure 1.3 demonstrates how general relativity allows for the quantization of a localized field.
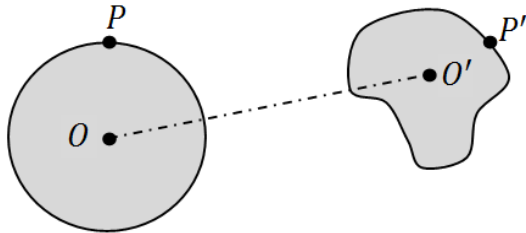
Applying the contravariant and covariant metrics together results in any underlying field to be transformed back to the $\eta_{\mu\nu}$ state; this is due to the equivalence principle and equation (**30**).

$$g^{\mu\beta} g_{\beta\nu} = \delta_\nu^\mu \qquad (\mathbf{30})$$

Transforming each field in this manner allows for quantization, where the velocity of each point upon the field is equivalent in both direction and magnitude. The dynamics of the field can therefore be reduced to the point-like particle perspective. Without quantization, each point along a particle's manifold will travel at various velocities. This will further require continuum mechanics to determine the proper translation, rotation and deformation.

A particle's manifold will vary depending upon the background vacuum energy density that it resides in. Under realistic considerations, the particle also influences the gravitational potential generated by the background field. If the effective energy and proper velocity of each particle is known, then it is possible to determine the effective space-time metric of any object; this is discussed in chapter **2**. If a particle is moving with respect to a local field, both special and general transformations must be applied. From (**30**), it was shown how wave fronts become equivalent to the $\eta_{\mu\nu}$ frame when space-time is deformed. Any Lorentz boost (**38**) must be applied relative to this configuration and then mapped from $g_{\mu\nu} \rightarrow \eta_{\mu\nu}$. This ensures that all field transformations are invariant for local observers; i.e. any stationary observer will view space relative to the space-time metric.

Figure 1.2. A finite 2-dimensional manifold in depicted in an initial (O) and final state (O'). Several affine transformations are applied including translation, rotation and deformation.

Figure 1.3. Sections of two manifolds $g^{\mu\nu}$ are depicted relative to a specific reference frame. (Left) The frame is with respect to the Euclidean frame $\eta_{\mu\nu}$. (Right) The frame is with respect to the deformed space-time metric $g_{\mu\nu}$.

Assuming a particle's classical position is with respect to the preferred reference frame ($\eta_{\mu\nu}$), r_n denotes an independent coordinate system for each. The notation can be simplified by introducing ∇_{mn}, which is the non-effective field from particle m to a point in the nth coordinate system. The effective field from particle m at the same point relative to the nth coordinate system is $\bar{\nabla}_{mn}$. Equation (**31**) is based upon the equivalence principle, where each particle is relative to the effective background field or space-time metric.

$$\bar{\nabla}_{mn}(r_n) \equiv \begin{cases} m = n : 0 \\ m \neq n : \bar{\nabla}_m(r_n) \end{cases} \tag{31}$$

The effective field of particle n due to all other particles is defined by equation (**32**),

$$\bar{\nabla}_n(r_n) = \nabla_n(r'_n) \tag{32}$$

where r'_n is determined by integration (**33**).

$$r'_n = r_n + \frac{1}{\Delta} \int_0^{r_n} \left(\sum_{m=1}^{N} \bar{\nabla}_{mn}(r_n) \right) dr_n \tag{33}$$

Relative to the Euclidean line element (dS), the transformed radial coordinate is defined as (**34**).

$$r'_n = \int_0^{r_n} \gamma_g(\vec{r}_n) \, dS = \int_0^{r_n} ds \tag{34}$$

The line element can be written in terms of the metric tensor (**35**).

$$(ds)^2 = g_{\mu\nu} dx^\mu dx^\nu \tag{35}$$

If only a single non-composite particle existed, $\gamma_g = 1$ and the field would be in the original configuration with respect to the co-moving frame. Therefore, the field of a single electron or positron would exhibit the E_0/r far-field envelope in agreement with classical theory. The maximum value of this localized field is proportional to E at the classical position.

If a point or region of infinite vacuum energy density (∇) exists, γ_g also becomes infinite. The previous mapping (**33**) fails at boundaries of infinite vacuum energy density or points beyond them. For example, if the field of an external particle is calculated, any radial lines at or beyond the singularity will be mapped to the event horizon. The wave fronts or sections also become non-continuous, violating the assumption of smoothly connected vacuum field manifolds. It is known from classical electrodynamics, QED and QCD that particles exist as localized fields. Due to these fields following the metric of space-time, they become restricted to any boundary of infinite vacuum energy. Since these fields are in return responsible for all classical forces including gravity, a black hole with event horizon would lack an external field. This is contradictory to EFEs, where objects with event horizon display external fields.

Finite black holes are predicted to exist with respect to vacuum field theory, although their surfaces must have finite vacuum energy density. Therefore, black holes should not only demonstrate external fields, but also nearly perfect black body spectrums. With vacuum field theory, it is literally impossible to create a point of infinite vacuum energy density from finite classical energy. From the methods herein, the effective field of any object can now be determined down to the Planck scale. With the advent of QCD and resulting states of dense quark matter, it is now possible to model the finite fields of quark stars and black holes. The name given to black holes remains valid since they demonstrate near perfect black body spectrums and immense gravitational fields. Energy will escape over time due to relativistic jets and free field radiation. The non-existence of event horizon and singularities is later discussed with respect to the cosmic background radiation and observed shape of the universe.

1.5. Electromagnetic Fields

Relativistic electrodynamics provides additional insight into how the vacuum field of a particle varies due to relative velocity. As the momentum of a uniformly charged particle increases, the electric field lines and magnitude loss isotropy. The electric field in terms of the particle's classical position is given by (**36**)[B], where $\theta = 0°$ is parallel with $\vec{v}$.

$$\vec{E} = k_e \frac{q\vec{r}}{r^3 \gamma^2 \left(1 - \left(\frac{v}{c_0}\right)^2 \sin^2(\theta)\right)^{3/2}} \tag{36}$$

The magnitude of the electric field is therefore (**37**).

$$E = k_e \frac{q\gamma}{r^2} [\gamma^2 \cos^2(\theta) + \sin^2(\theta)]^{-3/2} \tag{37}$$

As the particle's momentum increases, the electric field is compressed in the direction of motion. The magnitude of the field perpendicular to motion also increases, while the electric field tangent to the particle's trajectory weakens. As the limit of $v \to c$ is approached the field becomes compressed into a cylindrical plane of infinite vacuum energy density, depicted in figure 1.4. These field dynamics with respect to the Lorentz transformation are crucial to the application of point-like sources in classical electrodynamics. This however does not indicate that the use of point-like sources in other field theories is valid.
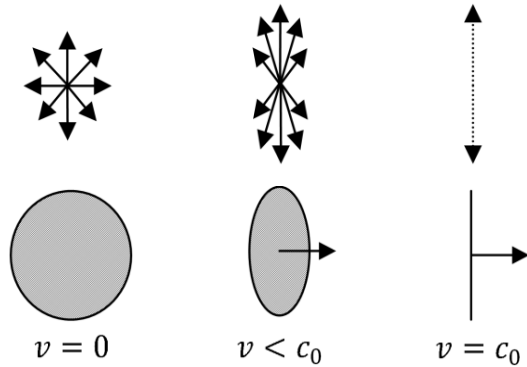
Figure 1.4. (Top) The electric field of an electron is provided in several states: (Bottom) An electron's manifold undergoing length contraction in the direction of motion.

For a massive non-composite particle, vacuum energy density is not proportional to the electric field. The electric potential can instead be related to vacuum energy density as demonstrated by equation (**18**). Returning to the foundations of vacuum field theory, there is a distinction between quantized energy and vacuum energy density. This is because quantized energy is with respect to the amount of vacuum energy density at the classical position. It is important to notice however that the gravitational potential is both equal to vacuum energy density and the variations in classical energy due to a potential. Since quantized energy has only two components, the classical dynamics of a point-like particle can therefore be retained. The remaining field dynamics are derived by applying a Lorentz transformation to the vacuum field of a particle.

The Lorentz transformation Λ (**38**)[B] allows mathematically defined objects to be transformed in space-time. The objects in this case are individual manifolds equipped with a scalar field, which depicts the vacuum energy density of each particle.

$$\Lambda \equiv \begin{bmatrix} \gamma & -\gamma\beta_i & -\gamma\beta_j & -\gamma\beta_k \\ -\gamma\beta_i & (1+\beta_{ii}) & \beta_{ij} & \beta_{ik} \\ -\gamma\beta_j & \beta_{ij} & (1+\beta_{jj}) & \beta_{jk} \\ -\gamma\beta_k & \beta_{ik} & \beta_{jk} & (1+\beta_{kk}) \end{bmatrix} \tag{38}$$

Where $\beta_{\mu v}$ is defined as (**39**).

$$\beta_{\mu v} = \frac{(\gamma - 1)\beta_\mu \beta_v}{\beta^2} = (\gamma - 1)\frac{v_\mu v_v}{\|\vec{v}\|^2} \tag{39}$$

In general any 4-vector can be transformed via (**40**), including the electromagnetic 4-potential.

$$R' = \Lambda R \tag{40}$$

Two consecutive Lorentz boost can be determined with matrix multiplication (**41**).

$$\Lambda(\vec{v}_1 + \vec{v}_2) = \Lambda(\vec{v}_1)\Lambda(\vec{v}_2) \tag{41}$$

With respect to the electromagnetic nature of matter, vacuum field theory would be incomplete without discussing photons. From the approximate field of a non-composite massive particle (**16**), vacuum energy density is determined from the classical gravitational potential and linear wave-like equation (**1**). This says nothing about how the electromagnetic field relates back to the unified scalar-vector field. There is also a distinction between individually localized photons and free electromagnetic energy. Classically, an electro-magnetic field can be described in terms of a superposition of waves. However, there is no guarantee that these are individual packets of vacuum energy. Unlike the electric field, super-positioned vacuum fields do not display field interference; i.e. positive and negative electric field contributions will result in no electric field, while vacuum energy density is always positive. It is therefore possible to use Fourier series to create a super-position of many waves, although these will not represent actual particles. Two processes in nature provide insight into the distinction between free electromagnetic energy and localized photon (or quantized particle); these are electron-positron annihilation and bremsstrahlung.

Electron-positron annihilation demonstrates the particle nature of the electromagnetic field, where a particle and its anti-particle produce gamma rays after colliding. The localized scalar fields of the electron and positron cancel, creating two or more massless photon. Assuming conservation of energy, the resulting photons will split quantized energy. Since the total vacuum energy of a single electron is infinite, only the conservation of classical energy can be considered. The gamma rays resulting from the annihilation process also remain localized in space indefinitely. This has implications for the CMBR, or black body spectrum observed in all directions of local space.

Each photon or localized packet of electro-magnetic energy remains localized due to the reinforcement of vacuum energy density. Assuming the symmetry of a photon is cylindrical, Bessel functions of the first kind (**42**) are applied perpendicular to the direction of propagation.

$$J_n(x) = \sum_{m=0}^{\infty} \frac{(-1)^m}{m!\,\Gamma(m+n+1)} \left(\frac{x}{2}\right)^{2m+n} \tag{42}$$

If a linear wave equation is used similar to (**1**), the gradient of the scalar component must have the opposite sign of the vector field. This will essentially require for the central region of the field to have quantized mass. Therefore, the linear-wave approximations cannot be taken literally. An actual photon will have no scalar mass at the classical position, and will therefore be anti-symmetric with respect to the vacuum scalar field. The wave equation is instead applied to approximate the far-field envelope under consideration of vacuum energy conservation. The exact nature of the underlying vacuum field is therefore irrelevant, as only vacuum energy density is required with respect to general relativity. Applying the linear wave approximation (**1**), a photons field perpendicular to propagation is (**43**).

$$\mathbb{V} = E_0\sqrt{(\pm J_0)^2 + (\mp J_1)^2} \approx \frac{E_0}{\sqrt{r}} \tag{43}$$

In order to determine the 3-dimensional vacuum energy density of a single photon, the envelope in the z-direction is required. Without a rigorous method capable of providing the exact vacuum field of a photon, the linear wave approximation must once again be applied. The vacuum field of an individually localized photon in Planck units is therefore (**44**), where coordinates are with respect to the particle's classical position.

$$\mathbb{V}(r,\theta,z) = E_0 e^{-|z|}\sqrt{(J_0)^2 + (J_1)^2} \approx \frac{E_0}{\sqrt{r}} e^{-|z|} \tag{44}$$

Bremsstrahlung is the second case of electromagnetic energy, where a charged particle passing close to another emits braking radiation. Unlike the previous case, electromagnetic energy is radiated as a free field over a range of frequencies. The free field should be treated as an independent manifold with respect to other localized fields and particles. In other words, the free electromagnetic field is locally invariant with respect to the space-time metric. This emission of electromagnetic energy in the framework of point-like sources is similar to the gravitational waves in general relativity. In general, theories that couple fields to point-like sources will generate waves upon the respective medium due to variations in a quantized source.

The emission of electromagnetic energy can further be related to a variation in vacuum energy density. For the non-relativistic case, the radial Poynting flux is defined as (**45**)[B].

$$\vec{S} = \vec{n} \frac{q^2 a^2}{4\pi r^2 c_0{}^3} \sin^2(\theta)$$ (**45**)

The electromagnetic energy radiated per unit solid angle is therefore (**46**)[B].

$$\frac{dW}{dt d\Omega} = \frac{q^2 a^2}{4\pi c_0{}^3} \sin^2(\theta)$$ (**46**)

The first order approximation of bremsstrahlung indicates that a charged particle will emit a free field electromagnetic dipole. It is important to realize that electromagnetic energy in this situation is not localized, but continuous over a range of angles and frequencies. It is distinct from the annihilation case, where two photons are emitted at unique angles in order to preserve quantized energy. With results from chapter **2**, the effective vacuum far-field of a moving electron is defined by (**47**).

$$\bar{\nabla} = \nabla(x', y', z') = \frac{E_0 \gamma}{\sqrt{(x)^2 + (y)^2 + (z\gamma)^2}}$$ (**47**)

Relative to quantized energy, the Lorentz scalar is the only free variable. Therefore γ will assume two states, i.e. prior to bremsstrahlung (γ_1) and after (γ_2). The variation of vacuum energy density between these states can be derived by subtracting $\bar{\nabla}(\gamma_2)$ from $\bar{\nabla}(\gamma_1)$, i.e. equation (**48**).

$$\Delta \bar{\nabla}_{EM} = \frac{E_0}{r} \left(\frac{\gamma_1}{\sqrt{(\gamma_1 \cos\theta)^2 + (\sin\theta)^2}} - \frac{\gamma_2}{\sqrt{(\gamma_2 \cos\theta)^2 + (\sin\theta)^2}} \right)$$ (**48**)

The initial and final states from (**47**) are expanded via Taylor expansion at $\gamma = 1$ resulting in (**49**).

$$1 + (\gamma - 1)\sin^2(\theta) - \frac{3}{2}(\gamma - 1)^2 \sin^2(\theta)\cos^2(\theta) + \cdots$$ (**49**)

Ignoring higher order contributions, equation (**49**) reduces to a dipole field approximation (**50**).

$$\Delta \bar{\nabla}_{EM} \cong \frac{E_0}{r}(\Delta\gamma)\sin^2(\theta)$$ (**50**)

The Lorentz transformation derived from classical electrodynamics is therefore directly related to a fundamental scalar field. The electromagnetic field cannot be easily related to vacuum energy, since only the electric potential is proportional to ∇. Therefore, the r^2 in (**45**) is expected, while vacuum energy decays proportional to the inverse distance. The vacuum energy emitted in terms of non-relativistic motion becomes (**51**). In consideration of a unified field theory, all particles would exist upon a single field in space. However, vacuum field theory depicts each localized field as a deformable manifold relative to a reference space ($\eta_{\mu\nu}$). In this perspective, vacuum energy density (∇) radiated due to bremsstrahlung is physically detached from the electron's manifold into a free field described by Maxwell's equations.

$$\dot{\nabla} \cong \frac{m_0 v a}{r} \sin^2(\theta)$$ (**51**)

1.6. Quantum Mechanics

Quantum mechanics was introduced by Erwin Schrodinger, who had initially attempted to create a relativistic theory. Due to the many difficulties related to the relativistic form, the time-dependent Schrodinger equation (**52**)[C] was instead published.

$$i\hbar\dot\psi = H\psi = \left(V - \frac{\hbar^2}{2m}\nabla^2\right)\psi \qquad (52)$$

In consideration of a classical potential such as the electric field produced by a proton, the probability of an electron being detected at any given position is $\psi\psi^*$. This should not be confused with the wave-function attributed to vacuum field theory, which depicts a Hamiltonian density. The wave function of quantum mechanics can be interpreted in various ways. Vacuum field theory agrees with the path-integral approach to quantum mechanics, where each particle has a classical location in space. It attributes no physical meaning to the quantum wave other than probability. This is known as the minimalist perspective or ensemble interpretation attributed to Max Born[D].

In order to comprehend fermion spin and mass, the field of spin 1 particles must be initially discussed. Photons are the most fundamental spin 1 particle and can be either polarized or non-polarized. For a circularly polarized photon, the spin state is either $\pm\hbar$. To simplify the problem, the photon will be reduced to a plane-wave that has a helix shaped electric field. Relative to a massive particle located at a fixed point in space, the propagating EM field will appear to spin around a fixed axis. The electric field however is actually traversing space at the speed of light perpendicular to the spin plane. The field is therefore not spinning with respect to the reference frame. The quantized energy of a photon can be written with respect to the perceived angular frequency or wavelength by equation (**53**). Circular polarization is identical to two super positioned plane-waves, so (**53**) remains true for all photons.

$$E = \hbar w = hf = hc/\lambda \qquad (53)$$

The photon's luminal field can be carried over to fermions. By applying spacetime algebra, it is observed that the field of an electron orbits the spin-plane at the speed of light. If this is true, then there must be kinematic effects due to the coupling between light-like field dynamics and space-like trajectories. The classical structure of the electron is discussed at the end of this section, for now the Dirac equation (**54**)[E] is examined for its connection to relativistic field dynamics.

$$i\hbar\dot\psi = H\psi = (c\boldsymbol{\alpha}\cdot\hat{\boldsymbol{p}} + \beta m_e c^2)\psi \qquad (54)$$

This can be rewritten in a more intuitive way since $m_e c^2$ is actually related to the intrinsic spin (**55**).

$$\frac{i}{c}\frac{\partial\psi}{\partial t} = \left(\boldsymbol{\alpha}\cdot\frac{\hat{\boldsymbol{p}}}{\hbar} + \boldsymbol{\beta}\frac{m_e c}{\hbar}\right)\psi \qquad (55)$$

Setting the rest energy of the electron equal to the spin angular frequency (**53**) results in a spin radius of (**56**); this is the reduced Compton wavelength. The radius (r_e) is constant relative to the metric of space, tracking a set of points along the field.

$$r_e = \hbar/m_e c \qquad (56)$$

In consideration of the quantization process used within relativity, the objective is to demonstrate that tracking a single point upon the electron's field satisfies the equations of motion at the classical position. To simplify the motion of the field, a local orthogonal coordinate system ($\boldsymbol{e}_1, \boldsymbol{e}_2, \boldsymbol{e}_3$) is defined relative to the classical position. Historically, Schrodinger was the first to apply the Heisenberg picture in order to determine the time dependence of the position operator (**57**).

$$: -i\hbar\dot{x}_k = [H, x_k] \qquad : \dot{x}_k = \frac{c}{\hbar}\alpha_k \qquad (57)$$

After integrating (**57**) twice with respect to time, the position operator becomes (**58**).

$$x_k(t) = x_k(0) + \frac{tc^2 p_k}{H} + \frac{i\hbar c}{2H}\left(\alpha_k(0) - \frac{cp_k}{H}\right)\left(e^{-2iHt/\hbar} - 1\right) \tag{58}$$

The last term is the complex quantum oscillation known as zitterbewegung; it is complex due the connection with spinors. Furthermore, the first two terms provide the classical trajectory of the particle, which is the average zitterbewegung path. Applying the Heisenberg picture, particle motion is combined with a non-classical rotation of the field and cannot be directly interpreted in the classical sense. From (**58**), the zitterbewegung angular frequency and radius are (**59**).

$$: w_{zwb} = \frac{2H}{\hbar} = \frac{2m_e c^2}{\hbar} \qquad : r_{zwb} = \frac{c}{w_0} = \frac{\hbar}{2m_e c} \tag{59}$$

Spinors in general require two rotations in order to return to the initial state. Picking half the classical radius upon the spin-plane remains a valid option. It is claimed that the field has an angular velocity equivalent to the speed of light; therefore, the angular frequency also doubles. Choosing the classical radius (**56**) simplifies the situation since it returns to the original state after a single rotation; i.e. the relativistic spin period is defined as (**60**).

$$T_s = \frac{p}{E_0}\frac{h}{m_0 v} = \frac{h\gamma}{E_0} \cong \frac{h}{m_e c^2} \tag{60}$$

To develop a mathematical model of the local coordinate system and spin, spacetime algebra is applied. Geometric (spacetime) algebra allows the geometric product to be defined as (**61**)[F].

$$\boldsymbol{uv} = \boldsymbol{u} \cdot \boldsymbol{v} + \boldsymbol{u} \wedge \boldsymbol{v} \tag{61}$$

The orthogonal reference vectors are related to the initial set by Lorentz spinors (**62**)[F], i.e. $SL(2, C)$.

$$\boldsymbol{e}_\mu = R\boldsymbol{\gamma}_\mu \tilde{R} \tag{62}$$

Spin arises as a bi-vector defined as (**63**)[F], where $\boldsymbol{\gamma}_2\boldsymbol{\gamma}_1$ is the spin plane.

$$S = is\boldsymbol{v} = \frac{\hbar}{2}i\boldsymbol{e}_3\boldsymbol{e}_0 = \frac{\hbar}{2}R\boldsymbol{\gamma}_2\boldsymbol{\gamma}_1\tilde{R} \tag{63}$$

For the free wave solution to the Dirac equation, the Dirac rotor becomes (**64**)[F].

$$R = e^{\Omega\tau/2}R_0 \qquad : \Omega = \frac{2mc^2}{\hbar}\boldsymbol{e}_1\boldsymbol{e}_2 \tag{64}$$

The time dependence of the local coordinates is related to the angular velocity bi-vector via (**65**)[F].

$$\gamma\frac{d\boldsymbol{e}_\mu}{dt} = \pm \Omega \cdot \boldsymbol{e}_\mu \tag{65}$$

On the spin plane $\mu = 1, 2$ resulting in (**66**), where t is relative to metric time.

$$\begin{aligned} : \frac{d\boldsymbol{e}_1}{dt} &= \pm\frac{2m_e c^2}{\gamma\hbar}\boldsymbol{e}_1\boldsymbol{e}_2\boldsymbol{e}_1 = \mp\frac{2m_e c^2}{\gamma\hbar}\boldsymbol{e}_2 \\ : \frac{d\boldsymbol{e}_2}{dt} &= \pm\frac{2m_e c^2}{\gamma\hbar}\boldsymbol{e}_1\boldsymbol{e}_2\boldsymbol{e}_2 = \pm\frac{2m_e c^2}{\gamma\hbar}\boldsymbol{e}_1 \end{aligned} \tag{66}$$

These equations define the time dependence of the local coordinate system attached to the electron's classical position. Since an electron moving at the speed of light violates relativity (**19**), intrinsic spin and zitterbewegung must be field related.

Comparing the Heisenberg approach to the geometric algebra derivation, the only self-consistent interpretation of the Dirac equation is mechanical in nature. The Heisenberg picture demonstrates that the position operator is following a complex, light-like trajectory. Geometric algebra demonstrates that the electron has a classical velocity ($\boldsymbol{v}$) and an attached coordinate system at the local position. In addition, a multivector rotation is an active transformation, which acts on a field independent of the reference coordinate system. The original space-like geodesics must therefore be modified so that the field always follows time-like geodesics. This in return allows the relativistic dynamics of a localized field to be reduced to a point in space-time.

The classical structure of electrons/positrons is required to further the localized field interpretation of the Dirac equation. Quantum theory hides the localized nature of particles through Lorentz transformations. Similar to general relativity, a localized field can be reduced to a point like object. Since the Dirac equation is Lorentz invariant, knowing the trajectory of any point along the field allows all others to be determined. Therefore, it is assumed that the active transformation applied to the spin-plane carries over to all other points along the field. According to classical electrodynamics, which is implied by quantum theory via minimal coupling, a moving electric field will produce a magnetic field equal to (**67**).

$$\vec{B} = \frac{E_0}{c^2}\left(\vec{v} \times \hat{E}\right) \tag{67}$$

The active transformation must be light-like acting on the entire field of the electron; i.e. the magnetic field becomes (**68**).

$$B = \frac{k_e q_e}{c r^2}\hat{\varphi} \tag{68}$$

The classic definition for a magnetic dipole is (**69**), where $\boldsymbol{m}$ is the dipole moment.

$$\vec{B}_{dipole} = \frac{k_m \|\boldsymbol{m}\|}{r^3}\left(2\cos(\varphi)\,\hat{r} + \sin(\varphi)\,\hat{\varphi}\right) \tag{69}$$

Since it is claimed that the Dirac equation is specific to a single point on the spin-plane, equations (**68**, **69**) are combined resulting in (**70**).

$$\frac{k_e q_e}{c} = \frac{k_m \|\boldsymbol{m}\|}{r} \tag{70}$$

Plugging in the classical radius (**56**) as defined in the Dirac equation results in a spin magnetic dipole moment equal to (**71**).

$$m_\mu = \|\boldsymbol{m}\| = q_e c r_e = \frac{q_e \hbar}{m_e} \tag{71}$$

Measuring the magnetic field along the spin-plane (at r_e) results in a magnetic dipole moment that is twice the Bohr magneton (**72**). If the zitterbewegung radius is used instead, the dipole moment becomes equivalent to the Bohr magneton.

$$\mu_B = \frac{q_e \hbar}{2 m_e} \tag{72}$$

It is obvious that the field generated by a spinning electron is not a true magnetic dipole. This is irrelevant until the hyperfine structure, where the nucleus interacts with the electron's far-field. The relativistic electric field also deforms with respect to the appropriate Lorentz transformations, while vacuum energy density must also be included.

Ignoring higher order effects, the approximate evolution of a spin 1/2 quantum system can be described by relativistic field dynamics. Returning to the spin bi-vector, the equation can be expanded with the geometric product (**73**)[G].

$$S = i s \boldsymbol{v} = i(\boldsymbol{s} \cdot \boldsymbol{v} + \boldsymbol{s} \wedge \boldsymbol{v}) \tag{73}$$

The Hodge dual (**74**) allows for an identity between the wedge product and cross product.

$$\boldsymbol{s} \wedge \boldsymbol{v} = *(\boldsymbol{s} \times \boldsymbol{v}) = i(\boldsymbol{s} \times \boldsymbol{v}) \tag{74}$$

The spin bi-vector (**75**) is composed of a real scalar and imaginary vector, relative to the angle between the intrinsic spin and classical velocity.

$$S = i s v[\cos(\beta) + i\hat{n}\sin(\beta)] \tag{75}$$

Figure 1.5 demonstrates how quantum mechanics reduces a field's relativistic spin to a single point in space-time.
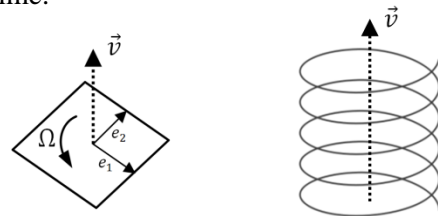
Figure 1.5. For an electron moving in a straight line without external field, $\beta = \pi/2$ to ensure the fields velocity remains c_0.

1.7. Applying Vacuum Fields

Vacuum field theory bridges the gap between general relativity and electrodynamics. It is argued within the previous sections that particles exist as localized field(s). This is contrary to Einstein's field equations, which depict particles as point-like sources. In perspective, EFEs take the quantized attributes of localized fields and couples them to a geometric field equation. The principle of locality is essential to Einstein's interpretation of general relativity, i.e. it allows point-like sources to have a local effect on the surrounding space-time metric. Quantum mechanics on the other hand demonstrates that local hidden variable theories are invalid via Bell's theorem. By applying vacuum field theory, the Dirac equation can be interpreted as a quantized field theory. The non-local hidden variables become visible once spacetime algebra is applied, which reveals the underlying relativistic field dynamics. Ignoring the significance of localized fields rather than point-like sources will result in theories that allow gravitational waves. For example, both EFEs and the Brans-Dicke theory allow these waves. Gravitational waves however have not been ruled out experimentally, although one has never been directly detected. Gravitational waves and the current probability of non-existence are further discussed throughout section (**2.2**).

The Lorentz transformation is a crucial aspect of quantum field theory or classical electrodynamics. Section (**1.5**) demonstrated that an accelerating charged particle emits vacuum energy density. This is related to the emission of electromagnetic energy in terms of bremsstrahlung. Therefore, application of locality in classical electrodynamics is valid because the electric potential is directly related to vacuum energy density. Application of point-like sources in quantum mechanics is also valid when considering the process of quantization. This allows for hidden non-local variables in agreement with Bell's theorem and action at a distance. Quantum mechanics itself is based upon quantized variables such as rest mass, position and momentum. Spin only complicates the situation by offsetting the point of quantization from the classical position, i.e. the electric field will always travel at the speed of light. Satisfying the equations of motion for a point along the field will automatically solve all others.

It is difficult to define vacuum energy density in terms of the additional fields within QFT and the standard model. However, the electric potential is proportional to vacuum energy density with the far-field approximation. The mass of a single fermion is also directly proportional to an underlying scalar field. The energy density at the classical position of a particle is crucial in terms of the quantization process. It allows a localized entity to be reduced to a point-like object, where classical mechanics can be applied. Vacuum energy density can also exist without the presence of classical fields. Neutrons for example are massive compared to electrons, but demonstrate minimal electromagnetic properties. Although the charge of negative and positive quarks can cancel, the underlying vacuum energy density must be conserved. The unified field theory would therefore require classical quantized forces to be abandoned. This is not required to arrive at a theory that predicts the outcome of any experiment. For example, it is always possible to include additional factors into mathematical models for agreement with observations. However, this does not mean the resulting theory will depict what is actually taking place. It will also be difficult if not impossible to arrive at an exact formulation connecting general relativity and the standard model. With vacuum field theory, far-field approximations can instead be applied in order to arrive at a perturbative theory of everything.

The Dirac equation written in covariant form is defined as (76).

$$\left(\gamma^\mu \partial_\mu + i\frac{m_0 c}{\hbar}\right)\psi = 0 \tag{76}$$

In order to include general relativity or external fields into equation (81), $\partial_\mu \to D_a$ is the covariant derivative (77) with respect to the local frame.

$$\left(i\gamma^a D_a - \frac{m_0 c}{\hbar}\right)\psi = 0 \tag{77}$$

The anholonomic Dirac matrices (γ^a) are related to the Dirac matrices (78) by a vierbein field.

$$\gamma^a \equiv e_\mu^a \gamma^\mu \tag{78}$$

The vierbein field is related to the metric tensor via equation (79).

$$g_{\mu\nu} = \frac{\partial \xi^a}{\partial x^\mu}\frac{\partial \xi^b}{\partial x^\nu}\eta_{ab} = e_\mu^a e_\nu^b \eta_{ab} \tag{79}$$

Equation (78) finds its origins from the commuter of the Dirac matrices (80).

$$[\gamma^a, \gamma^b] = 2\eta^{ab} \tag{80}$$

In order to relate the local tetrad frame to the metric, the general commuter is defined as (81).

$$\left[e_\mu^a \gamma^a, e_\nu^b \gamma^b\right] = 2g^{\mu\nu} \tag{81}$$

The local frame is attached to the electron's classical position and remains light-like. Therefore, the Dirac equation with respect to the preferred reference frame ($\mu, \nu, ...$) becomes (82).

$$\left(ie_\mu^a \gamma^\mu D_\mu - \frac{m_0 c}{\hbar}\right)\psi = 0 \tag{82}$$

The covariant derivative (83)[H] includes variations from the metric of space and any external electro-magnetic field defined upon it.

$$D_\mu = \partial_\mu + \frac{1}{4}w_\mu^{ab}\eta_{ab} - \frac{ie}{\hbar c}A_\mu \tag{83}$$

Since Planck units offer a natural scale for vacuum fields, the equations for the remainder of this section are written with $\hbar = c = G = 1$. The metric relative to vacuum field theory in accordance with section (1.5) is isotropic, i.e. it must be defined by a single scalar field (γ_g). Therefore, the vierbein defined in (78) is directly related to the effective vacuum energy density (84).

$$e_\mu^a = \gamma_g = 1 + \overline{\nabla} \tag{84}$$

Neglecting any sub-structure of the nucleus or self-interactions, the static field is approximately (85).

$$\overline{\nabla}_p \approx \frac{m_p}{r} \tag{85}$$

The Dirac equation with an external field is (86).

$$\left[i\gamma^\mu\left(\partial_\mu + \frac{1}{4}w_\mu^{ab}\eta_{ab} - ieA_\mu\right) - \frac{m_0}{\gamma_g}\right]\psi = 0 \tag{86}$$

In order to ensure that the field remains light-like, the spin connection (87)[H] must be introduced into the covariant derivative. The Christoffel symbols ($\Gamma^\nu_{\sigma\mu}$) are further derived from vacuum energy density and resulting space-time metric.

$$w_\mu^{ab} = e_\nu^a \partial_\mu e^{\nu b} + e_\nu^a e^{\sigma b}\Gamma^\nu_{\sigma\mu} \tag{87}$$

The space-time indices can be raised or lowered by applying $g^{\mu\nu}$ or $g_{\mu\nu}$ respectively; i.e. (88).

$$e^{\nu b} = g^{\mu\nu}e_\mu^b = \frac{1}{2}\left[e_\mu^a \gamma^a, e_\nu^b \gamma^b\right]e_\mu^b \tag{88}$$

Solutions that are more exact require for the interaction between individually localized vacuum fields to be accounted for, i.e. the nucleus and electron. This usually involves solving continuous fractions by iteration discussed in section (2.6). Since the inverse distance is an approximation for the far-field, it is also necessary to apply an energy cut-off when the radius is 1 in Planck units. This ensures that vacuum energy density does not surpass the maximum value depicted by quantized or classical energy.

1.8. The Standard Model

The standard model is an extension of quantum field theory, which is based upon classical electrodynamics and special relativity. It includes several other fields such as the electroweak and Higgs, which model weak interactions and mass. Many of the previous principles from the Dirac equation carry over to quantum electrodynamics (QED) and the standard model. The Lagrangian density (**89**)[I] of QED for example consists of the Dirac equation and classical electromagnetic contributions.

$$L_{QED} = \overline{\psi}(i\not{D} - m)\psi - \frac{1}{4}F_{\mu\nu}F^{\mu\nu} \tag{89}$$

QED is formulated with classical fields coupled to spinning light-like manifolds. In this perspective, the mass term offers no additional insight beyond semi-classical Lagrangian dynamics. Due to this, extensions of quantum theory fail to explain the physical essence behind classical fields and mass. This however does not make the theory useless, as experiments can only measure quantized variables including rest mass, position and momentum. The electromagnetic field is also closely related to vacuum field theory and depicts time dependence of quantized charged particles.

The transition from QED to a more general theory requires the addition of neutral currents and weak interactions. The standard model unifies weak interactions and QED with electroweak theory, defined by the $SU(2)_L \times U(1)_Y$ gauge group. Neutral vector bosons A_μ (photon) and Z_μ (Z^0 mass eigenstates) are related to the fields responsible for weak interactions via the Weinberg angle (**90**)[I]. The coupling angle varies according to the energy scale or momentum transfer involved. It is also related to the running coupling constants of $SU(2)_L$ and $U(1)_Y$ (g and g' respectively).

$$\begin{bmatrix} A_\mu \\ Z_\mu \end{bmatrix} = \begin{bmatrix} \cos\theta_W & \sin\theta_W \\ -\sin\theta_W & \cos\theta_W \end{bmatrix} \begin{bmatrix} B_\mu \\ W_\mu^3 \end{bmatrix} \tag{90}$$

The neutral components are included within the interaction Lagrangian density (**91**)[I], along with the running coupling constants. In order to ensure that $SU(2)_L$ invariance in not violated, a current (J_μ^Y) is added which preserves the symmetry.

$$L_{int}^{(W)} = -ig J_\mu^3 W^{3\mu} - i\frac{g'}{2}J_\mu^Y B^\mu \tag{91}$$

The $SU(2)_L \times U(1)_Y$ gauge group (**92**)[I] shares similarities with the 2-dimensional rotors applied in space-time algebra.

$$\psi_L \to \psi'_L = e^{i\theta_a\sigma^a/2}e^{i\beta/2}\psi_L \tag{92}$$

The projections for left-handed and right-handed components are (**93**)[I].

$$: \psi_L = \frac{1}{2}(1+\gamma^5)\psi \qquad : \psi_R = \frac{1}{2}(1-\gamma^5)\psi \tag{93}$$

In canonical form, even sub-algebra solutions ($R_{1,3}^+$) to the Dirac equation for $\psi\tilde{\psi} \neq 0$ are (**94**)[G].

$$\psi = \sqrt{\rho}e^{i\beta/2}R \tag{94}$$

The connection between (**92**) and (**94**) arises because the group of 2D rotors and unitary group $U(1)$ are locally isomorphic. However, there are two unique copies of $U(1)$: $U(1)_{EM}$ and $U(1)_Y$ with generators defined as (**95**)[I] respectively.

$$: Q = \frac{Y}{2} + I_3 \qquad : Q = Y \tag{95}$$

The second component of (**92**) is locally isomorphic to $SO(3)$, although requires two complete rotations in order to return to the original state. The Pauli matrices define the axis of rotation, while θ_a is the gauge parameter; i.e. the amount of rotation on each spin axis. Since the lie algebra of $SU(2)$ and $SO(3)$ are isomorphic, the general rotor in R^3 is defined as (**96**). Thus $i\sigma^a$ are the infinitesimal generators of $SU(2)$, similar to T_a.

$$R = \cos\frac{\theta}{2} + T_3\hat{\boldsymbol{n}}\sin\frac{\theta}{2} \tag{96}$$

Returning to the conical solution of the Dirac equation, the beta factor encodes the angle between the spin-plane and velocity. Furthermore, the rotor determines the rotation of the field with respect to spin-coordinates. Combining these properties with the $SU(2)_L \times U(1)_Y$ gauge demonstrates the degrees of freedom for the underlying field. Either the spin-plane to velocity angle is varied, or an active 3-dimensional rotation is applied with respect to a rotational-axis. Similar to the Dirac equation, the process of quantization is crucial to understanding these transformations. It allows a localized field to be treated as a point-like object. Spin for example allows the quantization process to take place away from the classical position. This allows an active 3-dimensional transformation to be reduced to the motion of a single point in space-time.

It should be no surprise that the standard model is not capable of becoming a unified field theory. Renormalization is the first of many signs that the choice of fields is poor, i.e. classical and/or multiple scalar-vector fields should not be applied. Beyond the initial choice of electromagnetism, the non-classical fields are a consequence of preserving symmetry and/or filling gaps. The standard model also requires a minimum of 19 free parameters and several running coupling constants determined experimentally[J]. Any unified field theory should have zero free variables except for the fundamental constants (c_0, G_0, $\hbar$, k_e), which depict underlying properties of space. For example, the electron rest mass should be determined from the only stable non-composite solution to the unified field theory. Quantized mass takes the particular value due to the non-linear nature of the field, i.e. there is only one stable value. The standard model in original form however does not attribute mass to fermions and other massive particles. An attempt to resolve this absence requires an additional field and resulting scalar particle, i.e. the Higgs field and boson respectively.

The Higgs field was introduced in 1962 by Philip Anderson to compensate for the lack of mass for gauge bosons within the standard model. The relativistic model was further developed in 1964 by independent groups who were awarded the Nobel Prize. The additional field predicted the existence of a Higgs boson, which gives mass to other particles. The mass of the Higgs boson can be theoretically determined from the mass of the top quark and w-boson. Earlier measurements of these particles predicted a Higgs boson with an expected mass of $85^{+54}_{-34} \, GeV$; however, recent world averaged values (March 2012)[K] of the top quark and W-boson vary the preferred value to $94^{+29}_{-24} \, GeV$. The standard model therefore predicts that the mass of the Higgs boson ranges from $70 - 123 \, GeV$ with theoretical methods. These values are relative to the top quark having a bare mass of $173.2 \pm 0.9 \, GeV$ and W-boson of $80.399 \pm 0.023 \, GeV$.

Direct methods of detecting the Higgs boson initially began at CERN with LEP2. Preliminary results from data collected over the year 2000 claimed that four LEP2 experiments were consistent to the 2.9 sigma level ("1.4 in 1000 chance of statistical fluctuation") of a $115 \, GeV$ Higgs boson[L]. This was reported in November 2000, based upon an excess of events over the theoretical background rates. Results were published in December 2001 conserving the previously predicted mass, although the combined probability had decreased to $2.4 \cdot 10^{-3}$[M]. From the four individual experiments, ALEPH provided the most significant results. The excess of events over background was initially placed at 3.4σ, which was further reduced to 3.2σ in the final report. The more recent large hadron collider began operations in November 2009, which also contains multiple experiments for detecting the Higgs boson. Initial results were released in July 2011 with respect to ATLAS and CMS, showing an excess of events around $144 \, GeV$[N]. This was compatible with a Higgs boson at the 2.9 sigma

level. An article published in nature around mid-august of the same year later revised the confidence to a sigma of 2.0[O]. Results that are more recent were published in December of 2011, where ATLAS had a signal at 126 GeV with 3.6 sigma; CMS showed an excess of events around 124 GeV with 2.6 sigma[P]. An additional weak signal was detected by both experiments around 119 GeV with a 2.1 sigma. Figure 1.6 depicts these recent results and theoretical mass as derived from the top quark and W-boson.

Between LEP2 and LHC, there seems to be a disagreement with the observed excess of events. The results of ALEPH demonstrated a sigma that is relatively close to ATLAS. If the Higgs boson exists in accordance to the standard model, both results cannot be correct. This raises concerns over the understanding of background processes and their contribution to excess events. There also lacks a single region that demonstrates a Higgs boson signal, i.e. mass has varied between individual experiments and runs. This of course can be explained by lack of data, both by the results of LEP2 and preliminary results at LHC. Relative to theoretical predictions, there exists a large margin
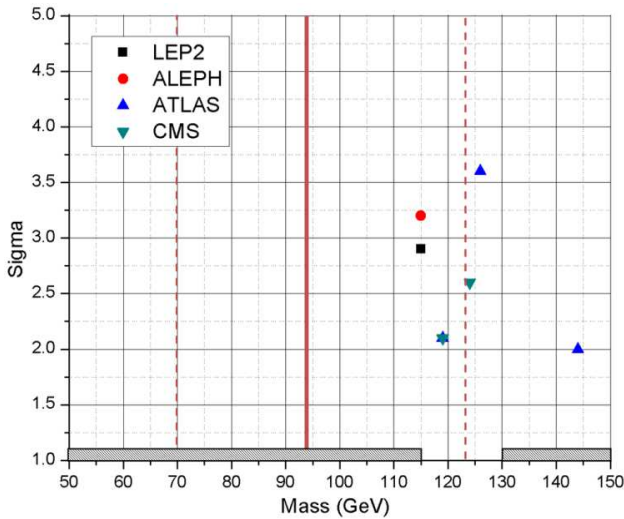
Figure 1.6. The thick red line is the theoretical Higgs mass determined from the top quark and W-boson; dashed lines are error boundaries as of March 2012 for the 68% confidence level[K]. The hatched area at the bottom depicts regions that have already been ruled out by other experiments.

between experimental results and the preferred mass range. Due to the uncertainty of the top quark's mass, recent claims of a Higgs-like particle between 4.5 to 5.0 sigma (125 GeV)[Q] are borderline acceptable up to the 68% confidence level[K]. However, only decay products of the Higgs boson are being directly detected, which coincide with the decay products of other known particles. Even at 6 sigma in agreement with the standard model, there lacks explanation for the physical essence of mass and additional deflection a particle experiences in external fields.

From vacuum field theory, the classical energy (**97**) of a single fermion is proportional to the point of maximum vacuum energy density. It is this central point of a quantized particle that depicts the kinematics of the entire localized field. This is in accordance with the process of quantization and affine transformations previously applied.

$$E = \sqrt{(pc)^2 + (m_0 c^2)^2} \qquad (97)$$

It is also predicted that massive particles such as electrons will have symmetric scalar fields, while massless photons consist of anti-symmetric scalar fields. This symmetry allows massive particles to have a finite amount of scalar mass at the classical position. Massive particles will therefore require momentum to move through an external field due to a localized scalar field rather than a massless scalar-vector field. Mass in QED is not well defined because the Dirac equation uses it to quantize spin. This relativistic spin is in return balanced with the quantized velocity so that all points upon the spin plane move at the local speed of light. The unified field theory should instead reduce to a single scalar-vector field (**98**), where mass is a localized scalar field ($\pm\emptyset$) depicting matter and anti-matter for each pair of fundamental particles.

$$\mathbb{V}(x) = \sqrt{\psi\psi^*} = \sqrt{(\emptyset)^2 + (v)^2} \qquad (98)$$

2. Relativity and Differential Geometry

Vacuum field theory requires a single scalar field determined from quantized variables and affine transformations. From this scalar field, it is possible to define the space-time metric similar to Einstein's field equations. Identical mathematical tools are required for either field theory, i.e. differential geometry and Riemann manifolds are necessary for quantizing a field's motion. Vacuum field theory also explains the mechanism behind gravitational force. Variations in time dependence at each point in space forces a quantized field to accelerate. Similar to section (**1.4**), applying the space-time metric to the particle's manifold ensures the underlying field's time dependence resembles the initial $\eta_{\mu\nu}$ configuration. Differential geometry and Riemann manifolds are therefore indispensable tools for general relativity, regardless of the underlying field theory.

A crucial modification to the theory of general relativity is the coupling between point-like sources and the corresponding space-time metric. If this coupling is poor, artifacts will appear under certain scenarios; i.e. gravitational waves and singularities. After discussing the correct metric from vacuum field theory, it becomes clear that EFEs are using the manifold of space-time in disguise of a localized field. The coupling between EFEs and Maxwell's equations is also poor, i.e. the contributions to the space-time metric are incorrect. The space-time metric should instead include all vacuum energy components, i.e. the electric and neutral fields. EFEs instead decouple these fields from quantized mass, depicting them as separate entities. The Schwarzschild solution in return cannot represent realistic objects since all massive particles display some electromagnetic component. Attempting to produce a proper field solution via the Einstein-Maxwell equations is also incorrect.

With respect to classical electrodynamics, a charged particle will have an effective electric field defined by (**99**). The velocity must be relative to the metric of space-time, or background vacuum energy density due to all other particles.

$$\vec{\mathbf{E}} = q\frac{\vec{r}}{r^3}\frac{\gamma}{(\gamma^2\cos^2(\theta)+\sin^2(\theta))^{3/2}} \qquad (99)$$

The electromagnetic field does not easily transform to a particle's vacuum energy density. However, the electric potential is proportional to $\overline{\nabla}$ with respect to charged particles. Since the electric field lines are parallel with $\hat{r}$, the electric field is proportional to the radial derivative of the effective vacuum energy density (**100**); where σ is the charge to mass ratio and Planck units are applied.

$$\vec{\mathbf{E}} = -\sigma\left(\frac{\partial}{\partial r}\overline{\nabla}\right)\hat{r} \qquad (100)$$

Assuming that the field is only compressed relative to the direction of motion, the effective vacuum field is (**101**).

$$\overline{\nabla} = \frac{E}{r}\frac{1}{\sqrt{(\gamma\cos\theta)^2+(\sin\theta)^2}} \qquad (101)$$

The partial derivative of the transformed field (**101**) is therefore (**102**).

$$-E_0\frac{\vec{r}}{r^3}\frac{\gamma}{(\gamma^2\cos^2(\theta)+\sin^2(\theta))^{3/2}} \qquad (102)$$

Equation (**100**) is equivalent to the effective electric field of a moving charged particle (**103**).

$$-\sigma\left(\frac{\partial}{\partial r}\overline{\nabla}\right)\hat{r} = q\frac{\hat{r}}{r^2}\frac{\gamma}{(\gamma^2\cos^2(\theta)+\sin^2(\theta))^{3/2}} \qquad (103)$$

Vacuum energy density is therefore directly related to the electric potential of a non-composite massive particle. This connection allows localized fields to be treated as point-like sources in electrodynamics.

2.1. General Relativity

The foundational aspects of general relativity discussed over the previous sections are sufficient for understanding the coupling between EFEs and classical electrodynamics. The Maxwell-Einstein field equations are introduced (**104**)[R], where $T^{\mu\nu}$ is the electromagnetic stress-energy tensor.

$$R^{\mu\nu} - \frac{1}{2}g^{\mu\nu}R = \frac{2G_0}{c_0{}^2\mu_0}T^{\mu\nu} \qquad (104)$$

The Reissner-Nordstrom metric (**105**) is a static solution to the Maxwell-Einstein field equations. It defines the gravitational field around a charged, non-rotating, spherically symmetric object.

$$g_{\mu\nu} = \begin{bmatrix} \gamma'_g{}^{-2} & 0 & 0 & 0 \\ 0 & \gamma'_g{}^2 & 0 & 0 \\ 0 & 0 & r^2 & 0 \\ 0 & 0 & 0 & r^2\sin^2\theta \end{bmatrix} \qquad (105)$$

Where γ'_g is (**106**)[S] and the Schwarzschild radius is defined as $r_s = 2E/\mathbb{\Delta}$.

$$\gamma'_g{}^2 = \frac{1}{1 - \frac{r_s}{r} + \left(\frac{k_eQ}{r\mathbb{\Delta}}\right)^2} \qquad (106)$$

This is the limit as $\overline{\mathbb{\Delta}} \to \mathbb{\Delta}$ relative to the vacuum field definition (**107**), after the proper electric field contribution (**18, 100**) is taken into consideration.

$$\gamma_g{}^2 = \frac{1}{\left(1 - \frac{\mathbb{V}}{\overline{\mathbb{\Delta}}}\right)^2} \overset{\overline{\mathbb{\Delta}} \to \mathbb{\Delta}}{=} \frac{1}{1 - \frac{r_s}{r} + \left(\frac{\mathbb{V}}{\mathbb{\Delta}}\right)^2} \qquad (107)$$

It is no coincidence that equations (**106**, **107**) have similar form. Vacuum field theory unifies mass and external fields into a single entity. A simple case would be that of an electron, which is spherically symmetric with respect to any co-moving frame. According to the second axiom, the conservation of vacuum energy creates an E/r far-field via the linear wave-equation (**1**). Since the electromagnetic field is based upon classical dynamics, it should not

contribute to vacuum energy density with respect to a charged particle; i.e. the EM components are already included in (**24**). The Reissner-Nordstrom metric for a single particle therefore reduces to the derived vacuum far-field of a charged particle after proper field contributions are considered.

Returning to electromagnetic fields, quantized conservation laws can be written as (**108**)[B]. The electromagnetic stress-energy tensor ($T^{\mu\nu}$) is once again related to classical mechanics.

$$\partial_\nu T^{\mu\nu} + \eta^{\mu\alpha}f_\alpha = 0 \qquad (108)$$

The field tensor (**109**)[B] is derived from the electromagnetic four-potential, it is therefore related to quantized lagrangian dynamics and should not contribute to the vacuum energy density. Once again, there is a distinction between vacuum energy density and quantized energy due to classical force.

$$F^{\mu\nu} = \partial^\mu A^\nu - \partial^\nu A^\mu \qquad (109)$$

The four-potential (**110**)[B] is proportional to the scalar and vector potentials.

$$A^\alpha = \left(\frac{\emptyset}{c_0}, \mathbf{A}\right) \qquad (110)$$

Einstein's field equations apply quantized densities in order to determine the curvature and metric of space-time. The quantized source term on the right side of EFEs (**111**) allows for mass and momentum to be applied in a continuum limit. The left side couples the quantized source(s) to a local geometric field or space-time metric.

$$R_{\mu\nu} - \frac{1}{2}g_{\mu\nu}R = \frac{8\pi G_0}{c_0{}^4}T_{\mu\nu} \qquad (111)$$

With the foundations offered from vacuum field theory, it is clear that Einstein's field equations contain several flaws. Up to this point, the three reasons initially offered for a revision of general relativity have been discussed.

The first was the coupling of point-like sources to the space-time metric. The metric further mimics the underlying vacuum field from which matter originates. Similar to electrodynamics, the coupling of a localized field to a point-like source allows for waves upon the relative medium; i.e. the classical electromagnetic field or space-time metric of general relativity. The vacuum field of a single non-composite particle however is proportional to its electric potential. When the electric potential of a particle varies relative to some background field, so does the underlying vacuum energy. This was previously discussed relative to bremsstrahlung, where this variation was directly related to the variation in vacuum energy density and Lorentz transformation. Since the space-time metric is defined solely by vacuum energy density, it is incorrect to include the electric field of a single particle as a separate entity.

The second flaw is similar to the first, where particles must exist as localized fields rather than point-like objects. Similar to relativistic electro-dynamics, the field of a particle becomes deformed when the background vacuum energy density varies. Therefore, the metric of space-time is of mathematical origin and plays no role in the physical structure of space. An observer will always view space relative to the metric of space-time. However, space does not deform at the large-scale structure as purposed by Einstein. This also pertains to gravitational waves, as it is claimed by the third postulate that matter is Planck scale fluctuations of space. It is contradictory to allow space-time waves from the quantized variables of vacuum fields, when vacuum fields are a representation of Planck scale waves. Furthermore, if vacuum fields were responsible for classical force, objects with event horizon would lack external gravitational fields; this is contradictory to EFEs vacuum solutions.

The third flaw is the incorrect coupling between electrodynamics and classical gravitational field. From section (**2**), it was argued that the electric field is a component of the underlying vacuum field. With the conservation of vacuum energy density or classical theory, a non-composite charged particle should display an E_0/r far-field. The Maxwell-Einstein vacuum solution $(T_{\mu v} = 0)$ gives a squared Lorentz scalar of (**112**).

$$\gamma'_g{}^2 = \frac{1}{1 - 2\frac{\nabla}{\Delta} + \left(\frac{k_e Q}{r\Delta}\right)^2} \tag{112}$$

For a single particle, $T_{\mu v} = 0$ everywhere except at the particle's classical position. Therefore, (**112**) is essentially the far-field solution of a single charged particle. However, the Lorentz scalar does not obey the E_0/r law as derived under the assumption of vacuum energy conservation. According to vacuum field theory, the correct squared Lorentz scalar for a single particle reduces to (**113**).

$$\gamma_g{}^2 = \frac{1}{1 - 2\frac{\nabla}{\overline{\Delta}} + \left(\frac{\nabla}{\overline{\Delta}}\right)^2} = \left(1 + \frac{\nabla}{\Delta}\right)^2 \tag{113}$$

(**113**) is the limit of equation (**112**) as $\overline{\Delta} \to \Delta$ and reduces to the Maxwell-Einstein vacuum solution after proper coupling of the electromagnetic field via equations (**18, 100**).

$$\gamma_g{}^2 = \frac{1}{1 - 2\frac{\nabla}{\Delta} + \left(\frac{\nabla}{\Delta}\right)^2} = \frac{1}{\left(1 - \frac{\nabla}{\Delta}\right)^2} \tag{114}$$

The limit produces a singularity when $\nabla = \Delta$, while the proper vacuum field solution (**115**) is always finite. Without proper electromagnetic contributions, the singularity instead arises when $2\nabla = \Delta$ as demonstrated by the Schwarzschild solution.

$$\gamma_g{}^2 = \frac{1}{1 - 2\frac{\nabla}{\Delta\gamma_g} + \left(\frac{\nabla}{\Delta\gamma_g}\right)^2} = \left(1 + \frac{\nabla}{\Delta}\right)^2 \tag{115}$$

2.2. Gravitational Waves

The existence of gravitational waves is crucial to the validity of EFEs. From a theoretical standpoint, variations in certain stress-energy moments allow quantized variables to transform into metric waves. If these waves do not exist, then the conservation of energy is clearly violated within EFEs. Indirect evidence for gravitational waves comes from the binary system PSR B1913+16. This system consists of orbiting neutron stars that emit pulsed radio signals at nearly constant periods. After measuring these pulses, their arrival was observed to oscillate over a period of about 7.75 hours. Additional observations allowed for the change in epoch of periastron to be measured, which agreed with the predictions of general relativity to within 0.2%[T]. However, it is the assumption that EFEs are correct which defines the plausible attributes of the system. It is possible for PSR B1913+16 to have parameters that vary from EFE solutions, i.e. these observations only provide indirect evidence for the existence of gravitational waves. Complications arise from uncertainties in the structure of neutron stars, their effective field, orbital parameters and classical energy flux.

Direct evidence by physically measuring the distortion due to gravitational waves appears to be the only valid option for proving their existence. Several experiments have been conducted over the previous 52 years; however, only LIGO, GEO600 and VIRGO are discussed due to precession. The probability of detecting a gravitational wave from a BH-BH event is approximated from table 2.2.

TABLE 2.2. Theoretical BH-BH detection rates

ID	Source	Published	BH-BH Detection Rates (yr^{-1})
A	[U]	1999	$0.19^{(b)}$, $400^{(a)(b)}$
B	[V]	2007	2, $500^{(b)}$
C	[W]	2010	$[2 \cdot 10^{-4}, 0.5]$
D	[X]	2010	$[0.05, 4.9]$
E	[Y]	2008	$[0.01, 1.7]$, $[0.11, 18]^{(a)}$
F	[Z]	2011	0.8
G	[AA]	2009	-
H	[AB]	2004	-
I	[AC]	2012	$[0.08, 0.17]^{(a)}$

Note: (a) indicates LIGO IE and (b) are older models.

The theoretical event rates are required for determining the probability of gravitational waves existing. They have varied drastically over the previous 15 years as demonstrated by table 2.3. The running length of each experiment is also provided in table 2.4.

TABLE 2.3. Theoretical event rates

ID	Experiment	Event Rate (yr^{-1})		
		NS-NS	NS-BH	BH-BH
A*	LIGO I	0.03	0.25	0.19
	LIGO IE	50	400	400
B*	LIGO I	100	30	500
B	LIGO I	20	1	2
C	LIGO I	$[2 \cdot 10^{-4}, 0.2]$	$[7 \cdot 10^{-5}, 0.1]$	$[2 \cdot 10^{-4}, 0.5]$
	LIGO II	$[0.4, 400]$	$[0.2, 300]$	$[0.4, 1000]$
DI	LIGO I	0.01	0.02	4.9
	LIGO II	45.1	85.8	$21,425$
DII	LIGO I	0.002	0.01	0.05
	LIGO II	9.5	42.8	242
E	LIGO I	$[0.015, 0.15]$	-	$[0.01, 1.7]$
	LIGO IE	$[0.15, 1.5]$	-	$[0.11, 18]$
	LIGO II	$[20, 200]$	-	$[16, 270]$
F	LIGO I	0.05	0.02	0.8
	LIGO II	$[60, 500]$	80	$2,000$
G	Virgo I	$[0.002, 0.04]$	-	-
	LIGO IE	$[0.02, 0.4]$	-	-
	Virgo+	$[0.25, 5]$	-	-
H	LIGO I	$[0.008, 0.13]$	-	-
	LIGO II	$[40.2, 310.9]$	-	-
I	Virgo+	0.003	$[0.01, 0.02]$	$[0.07, 0.08]$
	Virgo II	$[3.0, 3.6]$	$[12, 19]$	$[35, 92]$
	LIGO S5	0.004	0.02	$[0.08, 0.09]$
	LIGO S6	$[0.008, 0.009]$	$[0.03, 0.04]$	$[0.17, 0.21]$

* indicates older theoretical models.

TABLE 2.4. Experiment runtime

Experiment	Run	Days	Run-Time	NS-NS Range
LIGO I	S1	4.8	$54.6^{[AD]}$	0.08 Mpc
	S2	18.0		0.3 Mpc
	S3	13.2		5.0 Mpc
	S4	18.6		8.6 Mpc
LIGO IE	S5	365	$730^{[AD][AE]}$	12.0 Mpc
	S6	365		~50 Mpc
Virgo I	VSR1	111	$111^{[AF]}$	12.4 Mpc
Virgo+	VSR2	98	$159.3^{[AG]}$	16.8 Mpc
	VSR3	61.3		~50 Mpc
GEO600	S4	28.8	$370.8+^{[AH]}$	~LIGO I (S1)
	S5	342+		~LIGO I (S2)

Note: The more recent runs of GEO600 are included since the detection rates are similar to the earlier LIGO I runs.

The probability of gravitational waves not existing is compared to flipping a loaded coin. When a normal coin is flipped, the probability of it landing tails is 50%. This is equivalent to measuring for gravitational waves over the period required for a single event, and having a 50% chance of detecting one. For a loaded coin, the result will always be tails regardless of N. As the coin is flipped N amount of times, the probability of the coin being loaded increases if the results are always tails. Therefore, the probability that the coin is loaded is equivalent to that of gravitational waves not existing. This probability is defined as (**116**), where N is the expected events per total period.

$$P(Null) = 1 - 2^{-N} \qquad (116)$$

Table 2.5 depicts the probability of gravitational waves not existing for each experiment and model.

TABLE 2.5. Theoretical detection rates by experiment

Experiment	Model	Max Events	P(Null) Min	P(Null) Max
LIGO I	A[*]	0.07	-	4.76%
	B[*]	94	-	~100.00%
	B	3.4	-	90.8%
	C	0.12	0.0049%	7.96%
	DI	0.74	-	40.0%
	DII	0.009	-	0.64%
	F	0.13	-	8.63%
LIGO IE	A[*]	1700	-	~100.00%
S5	I	0.114	6.96%	7.60%
S6	I	0.259	13.43%	16.4%
Virgo+	I	0.045	2.48%	3.07%
GEO600 (S4/S5)	A[†]	0.48	-	28.2%
	B[*†]	640	-	~100.00%
	B[†]	23.4	-	~100.00%
	C[†]	0.81	0.033%	43.1%
	DI[†]	5.01	-	96.9%
	DII[†]	0.063	-	4.27%
	F[†]	0.88	-	45.8%

[*] indicates old model

[†] indicates LIGO I statistics were applied to the latest runs of GEO600.

There exist several orders of magnitude between individual models. The majority of this variation is due to the merger rate and density of BH-BH events. Excluding the older models, the remaining models are grouped together in table 2.6. With respect to old models, it is clear from the number of events expected that gravitational waves could not exist ($\sigma > 6$). The new models decrease expected rates by three to four orders of magnitude. However, two of the new models also indicate a $\sigma > 6$ for the max event limit, with a third at $\sigma = 3.7$. The current data does not allow for a definitive answer for whether gravitational waves exist, although it does begin to raise doubts. The expected rates are also highly dependent upon the theoretical model. Assuming that these do not vary drastically in the future, the next generation of detectors should be capable of bringing all models to $\sigma > 6$. For example, conservative estimates of Advanced LIGO (LIGO II) project hundreds of events per year. Advanced LIGO and Advanced Virgo are expected to begin operations in 2014, so direct proof will require three to four years as of 2013. Beyond these, the Laser Interferometer Space Antenna (LISA) will provide a new range of frequencies. LISA is not expected to be in operation until after 2020; however, it will be capable of detecting massive BH-BH events if gravitational waves exist. Due to the net BH-BH mass, the waves generated would be several orders of magnitude larger than other sources.

TABLE 2.6. Approximate combined probability

Models	Net Max Events	Net P(Null) Min	Net P(Null) Max	Sigma Max
B,I,I,B[†]	27.2	-	~100.00%	> 6
C,I,I,C[†]	1.35	27.1%	60.8%	1.7
D,I,I,D[†]	6.17	28.8%	98.6%	3.7
E,DII,I,E[†]	41.3	37.0%	~100.00%	> 6
F,I,I, F[†]	1.43	-	62.9%	1.8

Note: The order of listed models is LIGO I, LIGO IE, VIRGO+, GEO600; model E is also included.

2.3. Single Particle Metric

For a massive non-composite particle, the field should be approximately (E_0/r) in the co-moving frame. Since the metric must be isotropic, the solution in spherical coordinates is (117).

$$\boldsymbol{g}_{uv} = \begin{bmatrix} \gamma_g^{-2} & 0 & 0 & 0 \\ 0 & \gamma_g^{2} & 0 & 0 \\ 0 & 0 & (\gamma_g r)^2 & 0 \\ 0 & 0 & 0 & (\gamma_g r)^2 \sin^2\theta \end{bmatrix} \quad (117)$$

The Lorentz scalar (118) is defined as usual, where the far-field approximation is applied.

$$\gamma_g = 1 + \frac{\nabla}{\Delta} \cong 1 + \frac{G_0 M}{r c_0^2} \quad (118)$$

For comparison, the Lorentz scalar relative to the Schwarzschild metric is written as (119).

$$\gamma'_g = \frac{1}{\sqrt{1 - 2\dfrac{G_0 M}{r c_0^2}}} \quad (119)$$

The geodesic equations are applied to determine the motion of a single particle inside the previous potential. Using space-like convention $(-+++)$, the space-time interval is defined as (120).

$$(ds)^2 = g_{\mu\nu} dx^\mu dx^\nu \quad (120)$$

Expanding the geodesic equations results in the proper acceleration for each component (121), $(x^0)^2$ must be replaced with $-(c_0 t')^2$.

$$\ddot{t}' = -2\Gamma^0_{01}\dot{t}'\dot{r}'$$
$$\ddot{r}' = c_0^2\Gamma^1_{00}\dot{t}'^2 - \Gamma^1_{11}\dot{r}'^2 - \Gamma^1_{22}\dot{\theta}'^2 - \Gamma^1_{33}\dot{\varphi}'^2$$
$$\ddot{\theta}' = -2\Gamma^2_{12}\dot{\theta}'\dot{r}' - \Gamma^2_{33}\dot{\varphi}'^2 \quad (121)$$
$$\ddot{\varphi}' = -2\Gamma^3_{13}\dot{r}'\dot{\varphi}' - 2\Gamma^3_{23}\dot{\theta}'\dot{\varphi}'$$

The geodesic equations become relative to the metric after applying the following relations (122).

$$: \frac{dx'^\alpha}{d\tau} = \gamma\frac{dx'^\alpha}{dt'} \qquad : \frac{d^2x'^\alpha}{d\tau^2} = \gamma^3\frac{d^2x'^\alpha}{dt'^2} \quad (122)$$

The Christoffel symbols are determined for an isotropic, spherical vacuum field in table 2.7. To compare the radial acceleration as derived from the geodesic equations to the algebraic results (29), the motion of a particle can be restricted to the radial direction (123); i.e. $\dot{\theta}$ and $\dot{\varphi}$ are 0.

$$\ddot{t}' = -\frac{2G_0 M}{(rc_0)^2\gamma_g}\dot{t}'\dot{r}'$$
$$\ddot{r}' = -\frac{G_0 M}{r^2\gamma_g^5}\dot{t}'^2 + \frac{G_0 M}{(rc_0)^2\gamma_g}\dot{r}'^2 \quad (123)$$

For a massive particle moving at escape velocity relative to the metric, $\dot{r}'$ is replaced by (27); $\dot{t}'$ is defined as (124), where $k = 1$ and $\gamma = \gamma_g$.

$$\dot{t}' = k\,\gamma_g^2 \quad (124)$$

The acceleration at escape velocity is (125) or (29).

$$a = \frac{d^2r'}{dt'^2} = -\frac{G_0 M}{r^2\gamma_g^4} \quad (125)$$

TABLE 2.7. Christoffel symbols between theories

$\Gamma^{\mu}_{\nu\sigma}$	Single Particle	Schwarzschild
$\Gamma^0_{01}, \Gamma^0_{10}$	$\dfrac{G_0 M}{\gamma_g(rc_0)^2} \cong \dfrac{1}{r}\dfrac{\nabla}{\Delta}$	$\gamma'_g{}^2\dfrac{G_0 M}{(rc_0)^2}$
Γ^1_{00}	$-\dfrac{G_0 M}{\gamma_g^5(rc_0)^2} \cong -\dfrac{1}{r\gamma_g^4}\dfrac{\nabla}{\Delta}$	$-\dfrac{G_0 M}{\gamma'_g{}^2(rc_0)^2}$
Γ^1_{11}	$-\dfrac{G_0 M}{\gamma_g(rc_0)^2} \cong -\dfrac{1}{r}\dfrac{\nabla}{\Delta}$	$-\gamma'_g{}^2\dfrac{G_0 M}{(rc_0)^2}$
$\Gamma^2_{12}, \Gamma^2_{21}$	$\dfrac{1}{\gamma_g r}$	$\dfrac{1}{r}$
Γ^1_{22}	$-\dfrac{r}{\gamma_g}$	$-\dfrac{r}{\gamma'_g{}^2}$
$\Gamma^3_{13}, \Gamma^3_{31}$	$\dfrac{1}{\gamma_g r}$	$\dfrac{1}{r}$
Γ^1_{33}	$-\dfrac{r}{\gamma_g}\sin^2\theta$	$-\dfrac{r}{\gamma'_g{}^2}\sin^2\theta$
$\Gamma^3_{23}, \Gamma^3_{32}$	$\cot\theta$	$\cot\theta$
Γ^2_{33}	$-\sin\theta\cos\theta$	$-\sin\theta\cos\theta$

Note: Single particle refers to massive and non-composite.

2.4. Gravitational Force and Potential

From sections (**1.3, 2.3**), it was observed that the gravitational potential is dependent upon a variation in the effective background vacuum energy density. For static fields, classical energy conservation does not depend upon the path taken between two points. The proper force (**126**) upon a particle is therefore similar to the relativistic Newtonian perspective. If a particle's geodesic path follows the gradient of $\overline{\mathbb{V}}$, the problem is always reduced to the covariant derivative of the scalar field; i.e. the vector $\vec{g}_1$ will point in the direction of $\nabla\overline{\mathbb{V}}$.

$$\vec{f} = -\nabla_{\vec{g}_1} U = -\frac{E_0}{\Delta}\nabla_{\vec{g}_1}\overline{\mathbb{V}} = -\frac{E_0}{\overline{\Delta}}\nabla\overline{\mathbb{V}} \tag{126}$$

The gravitational potential energy (U) is derived by equating $\gamma_G = \gamma$ as applied in section (**1.3**); the potential is therefore defined as (**127**).

$$\Phi = -c_0{}^2\frac{\overline{\mathbb{V}}}{\Delta} \tag{127}$$

Vacuum field theory requires that the metric of space-time is isotropic, while EFEs are anisotropic. The choice of isotropy or anisotropy is crucial for motion as observed by a distant observer. This is not locally detectable since any observer ($g^{\mu\nu}$) deforms with respect to the space-time metric ($g_{\mu\nu}$). Under the assumption that vacuum energy density is conserved, the vacuum far-field energy of a non-composite particle should at most remain constant or decrease when moving through an external field.

Conservation of classical energy does not always ensure conservation of vacuum energy density. The problem is complicated since actual particles will consist of an infinite amount of vacuum energy. However, it is possible to compare configurations of the vacuum field to determine if vacuum energy density is conserved. In this case, only the far-field is applied for simplicity. The conservation of vacuum energy density is discussed relative to the transformed vacuum fields of an anisotropic and isotropic metric. Since a realistic gravitational field will complicate the field dynamics, a Cartesian coordinate system will instead be applied so that $(r, \theta, \emptyset) \to (x, y, z)$. The potential along the x-axis is anisotropic in the sense that it only increases in a single direction ($\hat{x}$), similar to the Schwarzschild metric ($\hat{r}$). It is difficult to consider a test particle initially placed at an infinite distance from the field. The problem is simplified by introducing an artificial potential as depicted in figure 2.1.

A massive particle placed where the local field is zero ($\eta_{\mu\nu}$) has a far-field approximated by (**128**); this is equivalent to $r \to \infty$ for a spherical metric.

$$\overline{\mathbb{V}}(r_n) = \frac{E_0}{r_n} \tag{128}$$

As the test particle moves into the gravitational potential, it gains quantized energy. This variation in energy is due to an influx of vacuum energy density rather than a net increase (**129**).

$$\overline{\mathbb{V}}(r, \theta) = \frac{E}{r_n}\frac{1}{\sqrt{(\gamma\cos\theta)^2 + (\sin\theta)^2}} \tag{129}$$

This means that the particle has gained quantized energy relative to a stationary observer; however, relative to $\eta_{\mu\nu}$ vacuum energy must be conserved. Since the anisotropic transformation is similar to the special relativistic version, it can be directly substituted into (**129**).
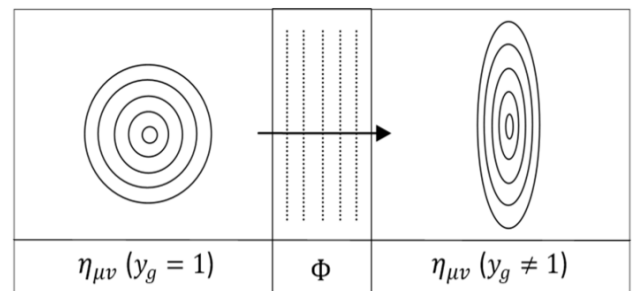
Figure 2.1. Sections of a localized field are illustrated relative to an initial and final state. The fields relative to the preferred reference frame ($\eta_{\mu\nu}$) are described by the space-time metric and Lorentz transformation.

The resulting effective field (**130**) is once again relative to $\eta_{\mu\nu}$ or the preferred reference frame.

$$\overline{\nabla}(r,\theta) = \frac{E_0}{r_n} \frac{\gamma}{\sqrt{(\gamma\gamma_g \cos\theta)^2 + \sin^2\theta}} \qquad (130)$$

Since the test particle will be traveling at escape velocity, $\gamma = \gamma_g$ can be applied. After reorienting the coordinate system, the Cartesian equivalent is defined as (**131**) with motion along the z-axis.

$$\overline{\nabla}(\vec{x}) = \frac{E_0}{\sqrt{\left(\frac{x}{\gamma}\right)^2 + \left(\frac{y}{\gamma}\right)^2 + (\gamma z)^2}} \qquad (131)$$

Equation (**131**) can further be put in spherical coordinates (**132**), allowing a shells net energy to be compared between configurations.

$$\overline{\nabla} = \frac{E_0}{r_n}\left[\left(\frac{\sin(\varphi)}{\gamma}\right)^2 + (\gamma\cos(\varphi))^2\right]^{-1/2} \qquad (132)$$

Volumetric integration between two radii results in shell energy for the anisotropic case (**133**),

$$\overline{\nabla}_{shell}\Big|_A^B = \frac{\pi\gamma(A^2 - B^2)}{\alpha}[LN(\gamma^2 - \alpha) - LN(\gamma^2 + \alpha)] \qquad (133)$$

where α is defined as (**134**).

$$\alpha = \sqrt{\gamma^4 - 1} \qquad (134)$$

The original field configuration (**129**) reduces to (**135**) after solving for shell energy.

$$\overline{\nabla}_{shell}\Big|_A^B = 2\pi(B^2 - A^2) \qquad (135)$$

For comparison, the variation in field energy for any shell can be defined with a factor between the two configurations. Therefore, the original field is multiplied by a function of the Lorentz scalar, defined as (**136**) for the anisotropic case.

$$k = \frac{\gamma}{2\alpha}[LN(\gamma^2 + \alpha) - LN(\gamma^2 - \alpha)] \qquad (136)$$

For an isotropic metric with identical setup, the field relative to the reference frame ($\eta_{\mu\nu}$) is defined by (**137**).

$$\overline{\nabla}(r,\theta) = \frac{E_0}{r_n\gamma_g} \frac{\gamma}{\sqrt{(\gamma\cos\theta)^2 + (\sin\theta)^2}} \qquad (137)$$

At escape velocity, the same $\gamma = \gamma_g$ relation can be applied resulting in (**138**).

$$\overline{\nabla}(\vec{x}) = \frac{E_0}{\sqrt{(x)^2 + (y)^2 + (\gamma z)^2}} \qquad (138)$$

After integration, the shell energy for the isotropic metric is (**139**).

$$\overline{\nabla}_{shell}\Big|_A^B = \frac{\pi(A^2 - B^2)}{\sigma}[LN(\gamma + \sigma) - LN(\gamma - \sigma)] \qquad (139)$$

Where σ is defined as (**140**).

$$\sigma = \sqrt{\gamma^2 - 1} \qquad (140)$$

The factor between the initial configuration (**135**) and isotropic case is therefore (**141**).

$$k = \frac{1}{2\sigma}[LN(\gamma - \sigma) - LN(\gamma + \sigma)] \qquad (141)$$

Considering vacuum energy density conservation, the isotropic and anisotropic cases are compared. As the far-field is rearranging, the peak energy of the field must also increase proportional to the classical quantized energy. There must be an influx of field energy into the central region, which is assumed smooth and finite. For field energy to be conserved, the far-field energy must be equivalent to or less than the original configuration. Plotting both (**136**, **141**) shows that only isotropic metrics are valid, i.e. the anisotropic case initially increases far-field energy for $\gamma \cong [1, 2.7]$. When $k = 1$ (or $\gamma \cong 2.7015$), the anisotropic metric begins to lose far-field vacuum energy density. This decrease must however occur at $\gamma = 1$ as demonstrated by the isotropic metric. Anisotropic space-time metrics therefore cannot conserve vacuum energy density.

2.5. Arbitrary Space-Time Metric

In order to determine the space-time metric from quantized fields, vacuum field theory must be applied. A coordinate basis is chosen so that $g_{\mu\nu}$ is diagonal with each term proportional to the general Lorentz scalar (γ_g). From the gradient of $\nabla(x^\alpha)$, the fundamental coordinate line is defined at each point in space with the base vector $\hat{e}_1$. If the gradient is zero, then the space is locally flat ($\eta_{\mu\nu}$). For example, if $\nabla \cong E_0/r$ then each point would have the fundamental coordinate line parallel to the radial direction ($\hat{r}$). The other base vectors would then be represented by any two orthogonal vectors perpendicular to $\hat{e}_1$. For other cases, the remaining orthogonal base vectors must be determined by the following methods.

Depending on choice of coordinates the field perpendicular to $\hat{e}_1$ can vary, requiring that at least one other principle direction exists. Each aligns with the planes of maximum and minimum curvature relative to constant ∇ surfaces. The additional bases are therefore eigenvectors of the shape operator (**142**), which is defined by the first and second fundamental forms.

$$W = I^{-1}II = \frac{1}{EG - F^2}\begin{bmatrix} LG - MF & MG - NF \\ ME - LF & NE - MF \end{bmatrix} \quad (142)$$

The first and second fundamental forms relative to the tangent plane of each surface $R^2 \in R^3$ is (**143**).

$$: I = \begin{bmatrix} E & F \\ F & G \end{bmatrix} \qquad : II = \begin{bmatrix} L & M \\ M & N \end{bmatrix} \quad (143)$$

If two unique principle directions exist beyond the initial gradient, vectors tangent to coordinate lines are (r_u, r_v). Since the first base vector's ($\hat{e}_1$) direction is determined by the normalized gradient of ∇, n is the normal to the surface (**144**)[AF].

$$n = \frac{\nabla\nabla}{\|\nabla\nabla\|} = \frac{r_u \times r_v}{\|r_u \times r_v\|} \quad (144)$$

From this notation, the two vectors (r_u, r_v) are not necessarily of unit length. Vacuum field theory is however locally isotropic, i.e. the space-time metric is determined from a single scalar field or vacuum energy density. The previous vectors are therefore directly proportional to the curvilinear basis, i.e. $r_\alpha = \gamma_g e_\alpha$. The first fundamental form is also equivalent to the metric tensor, i.e. each component is the scalar product ($g_{\mu\nu} = g_\mu \cdot g_\nu$). The variables become $E = r_u \cdot r_u$, $F = r_u \cdot r_v$, $G = r_v \cdot r_v$. This can be extended to three dimensions, where the first fundamental form (**145**)[AF] is represented in quadratic form.

$$I(dx, dy, dz) = \begin{bmatrix} dx \\ dy \\ dz \end{bmatrix}^T \begin{bmatrix} A_{11} & A_{21} & A_{31} \\ A_{12} & A_{22} & A_{32} \\ A_{13} & A_{23} & A_{33} \end{bmatrix} \begin{bmatrix} dx \\ dy \\ dz \end{bmatrix} \quad (145)$$

The components ($A_{\mu\nu} = r_\mu \cdot r_\nu$) can be defined in terms of partial derivatives of ∇ (**146**)[AF]; where ($dx \rightarrow dx^1$), ($dy \rightarrow dx^2$), ($dz \rightarrow dx^3$) and partial derivatives are written as $\nabla_i \nabla_{jk} = {}_{i,jk}$.

$$: A_{11} = {}_{2,31} - {}_{3,21} \qquad : A_{22} = {}_{3,12} - {}_{1,32}$$

$$: A_{33} = {}_{1,23} - {}_{2,13}$$

$$: A_{21} = A_{12} = (1/2)({}_{3,11} - {}_{1,31} + {}_{2,32} - {}_{3,22}) \quad (146)$$

$$: A_{31} = A_{13} = (1/2)({}_{2,33} - {}_{3,23} + {}_{1,21} - {}_{2,11})$$

$$: A_{32} = A_{23} = (1/2)({}_{1,22} - {}_{2,12} + {}_{3,13} - {}_{1,33})$$

The second fundamental form is now introduced, which when combined with the first allows the other principle directions to be determined. From the two dimensional II (**143**), the variables can be defined as $L = r_{uu} \cdot n$, $M = r_{uv} \cdot n$, $N = r_{vv} \cdot n$, or as a tensor $B_{\mu\gamma} = r_{\mu\gamma} \cdot n$. Using the following method, the second fundamental form can be written in terms of partial derivatives of the vacuum energy density scalar field (**147**).

$$II(dx, dy, dz) = \nabla_x dx + \nabla_y dy + \nabla_z dz \quad (147)$$

For an implicit surface where $\mathbf{\nabla}(x,y,z) = 0$, both fundamental forms are equal to zero. If the partial derivative of the field with respect to a given component is non-zero, that component can be solved for within $II(dx, dy, dz)$ and substituted into $I(dx, dy, dz)$, arriving at the third fundamental form (III). The idea is to factor the new expression so that it is quadratic with respect to the two remaining components. If $\mathbf{\nabla}_z \neq 0$, then $(\mathbf{148})^{[AF]}$ becomes a function of $(dx,\ dy)$.

$$III(dx, dy) = U(dx)^2 + V dx dy + W(dy)^2 = 0 \quad (\mathbf{148})$$

The discriminant of this equation is defined as $\Delta = V^2 - 4UW$, which can be used to determine the remaining principle directions $(\mathbf{149})^{[AF]}$.

$$\mathbf{T} = \begin{bmatrix} (-V \pm \sqrt{\Delta})\mathbf{\nabla}_z \\ 2U\mathbf{\nabla}_z \\ (V \mp \sqrt{\Delta})\mathbf{\nabla}_x - 2U\mathbf{\nabla}_y \end{bmatrix} \quad (\mathbf{149})$$

These vectors can be solved for in other cases where $\mathbf{\nabla}_z = 0$ by cyclic permutation of the components[AF]. The components of $\mathbf{A}_{\mu\gamma}$ remain constant, although U, V and W must each be recalculated and the components of $\mathbf{T}$ rearranged. For example, if $\mathbf{\nabla}_x \neq 0$ were true instead, the correct principle directions are defined as $(\mathbf{150})$, i.e. $(x \to y), (y \to z), (z \to x)$.

$$\mathbf{T} = \begin{bmatrix} (V \mp \sqrt{\Delta})\mathbf{\nabla}_y - 2U\mathbf{\nabla}_z \\ (-V \pm \sqrt{\Delta})\mathbf{\nabla}_x \\ 2U\mathbf{\nabla}_x \end{bmatrix} \quad (\mathbf{150})$$

The complete curvilinear basis is therefore defined as $(\mathbf{151})$.

$$:\hat{e}_1 = \frac{\nabla \mathbf{\nabla}}{\|\nabla \mathbf{\nabla}\|} \qquad :\hat{e}_2 = \frac{\mathbf{T}_1}{\|\mathbf{T}_1\|} \qquad :\hat{e}_3 = \frac{\mathbf{T}_2}{\|\mathbf{T}_2\|} \quad (\mathbf{151})$$

In general, the initial coordinate system used for the gradient and partial derivatives must be orthogonal. The resulting curvilinear coordinates will also consist of an orthogonal basis, which follows the

coordinate lines of the metric tensor $(\mathbf{g}_{uv})$. To transform from the curvilinear basis $\hat{e}_\alpha$ to $\vec{g}_\alpha$ requires a tensor so that $(\mathbf{152})$ is true. Since each component is already aligned, $\mathbf{F}$ is diagonally symmetric and varies only in magnitude.

$$\vec{g}_\alpha = \mathbf{F}_{v\alpha}\hat{e}_v \quad (\mathbf{152})$$

Due to the parameterization of effective vacuum fields with metric distance, the transformation must be isotropic. In comparison to the relativistic case where the field is compressed in a single direction, the presence of background vacuum energy warps a particles manifold equivalently in all directions at each point. Without this feature, the perceived space-time metric cannot be attributed to a relative medium upon space, further induced by vacuum energy density or a scalar field. From the isotropic nature of general field transformations, the previous tensor $\mathbf{F}$ can be written as $(\mathbf{153})$.

$$\mathbf{F} = \begin{bmatrix} \gamma_g & 0 & 0 \\ 0 & \gamma_g & 0 \\ 0 & 0 & \gamma_g \end{bmatrix} = \gamma_g \eta_{\mu v} \quad (\mathbf{153})$$

The tensor $(\mathbf{153})$ is extended to a Minkowski space via $(\mathbf{154})$.

$$\mathbf{F} = \begin{bmatrix} \gamma_g^{-1} & 0 & 0 & 0 \\ 0 & \gamma_g & 0 & 0 \\ 0 & 0 & \gamma_g & 0 \\ 0 & 0 & 0 & \gamma_g \end{bmatrix} \quad (\mathbf{154})$$

Therefore, an arbitrary space-time metric $(\mathbf{155})$ can be defined relative to the curvilinear basis.

$$g_{\mu v} = \begin{bmatrix} \gamma_g^{-2} & 0 & 0 & 0 \\ 0 & \gamma_g^{\,2} & 0 & 0 \\ 0 & 0 & \gamma_g^{\,2} & 0 \\ 0 & 0 & 0 & \gamma_g^{\,2} \end{bmatrix} \quad (\mathbf{155})$$

To determine the proper space-time metric for any object, the effective vacuum energy density must first be calculated; see section $(\mathbf{2.6})$. The curvilinear basis is then determined for time dependence.

2.6. Numerical Methods

Since solutions are based upon each individual particles influence on local fields, realistic objects must be numerically determined. Each particle further consists of a localized field relative to a preferred reference frame ($\eta_{\mu\nu}$). Therefore, the field of a single particle does not follow the metric induced by its own vacuum field. It instead follows the background vacuum field depicted by all other particles and free fields. This is applied to determine the effective space-time metric of any object using quantized variables. For first-order methods, the field of each particle will undergo isotropic deformations. The magnitude of these transformations will be proportional to the general Lorentz scalar at the classical position. Therefore, each particle has a unique general Lorentz scalar (**156**) due to the effective field of every other particle; note that ($r_n = 0$) is equivalent to (d_n).

$$\gamma_{g,n} = 1 + \frac{1}{\Delta} \sum_{m=1}^{N} \overline{\mathbb{V}}_{mn} (r_n = 0) \qquad (156)$$

For two particles at rest relative to the space-time metric, the effective fields are defined as (**157**).

$$: \overline{\mathbb{V}}_1(r_1) = \frac{E_1}{r_1 \gamma_{g,2}} \qquad : \overline{\mathbb{V}}_2(r_2) = \frac{E_2}{r_2 \gamma_{g,1}} \qquad (157)$$

In Planck units, the Lorentz scalars (**156**) can be written as continuous fractions (**158**).

$$\gamma_{g,1} = 1 + \frac{E_1}{d_1} \cfrac{1}{1 + \cfrac{E_2}{d_2} \cfrac{1}{\gamma_{g,1}}} \qquad (158)$$

Setting $a = E_1/d_1$ and $b = E_2/d_2$ results in (**159**).

$$x = 1 + \cfrac{a}{1 + \cfrac{b}{x}} \qquad (159)$$

The effective Lorentz scalar is therefore (**160**).

$$\gamma_{g,1} = \frac{1}{2}\left(\sqrt{a^2 + 2a - 2ab + (1+b)^2} + a - b + 1 \right) \qquad (160)$$

If both particles have equivalent rest mass ($E_0 = E_n$), the effective field of each is (**161**); where d is the distance between particles.

$$\overline{\mathbb{V}}_n(r_n) = \frac{2E_0}{r_n} \frac{1}{\left(1 + \sqrt{1 + 4\frac{E_0}{d}}\right)} \qquad (161)$$

Assuming the gradient of the local vacuum field is small, the first order approximation is useful for determining the field of large objects. However, systems with more than two particles are more difficult to deal with. The objective is to develop an iterative numerical method that is equivalent to the algebraic results.

The constant isotropic deformation is retained for dust solutions. Assuming each particle is stationary relative to the effective metric ($g_{\mu\nu}$), the algorithm for two particles is the following.

1. Start with the constant, non-effective field of both particles; i.e. E_1/r_1 and E_2/r_2.
2. Determine $\gamma_{g,1}$ and $\gamma_{g,2}$ from (**156**), relative to the non-effective fields defined in **1**.
3. Iterate by updating effective fields defined as $E_1/(r_1 \gamma_{g,1})$ and $E_2/(r_2 \gamma_{g,2})$.
4. Determine $\gamma_{g,1}$ and $\gamma_{g,2}$ relative to the effective fields calculated in **3**.
5. Loop back to **3**.

This can also be calculated by hand, where the first few iterations are (**162**) in arbitrary units.

$$: \mathbb{V}_1 = \frac{E_1}{r_1} \qquad (\text{I1}) : \overline{\mathbb{V}}_1 = \frac{E_1}{r_1} \cfrac{1}{1 + \cfrac{E_2}{d_2 \Delta}}$$

$$(\text{I2}) : \overline{\mathbb{V}}_1 = \frac{E_1}{r_1} \cfrac{1}{1 + \cfrac{E_2}{d_2 \Delta} \cfrac{1}{1 + \cfrac{E_1}{d_1 \Delta}}} \qquad (162)$$

The previous iterative method is equivalent to solving the continuous fractions of equation (**156**) and can be extended to N particles.

Expanding equation (**156**) by hand matches the iterative method for three particles, although the equations become relatively large. The effective Lorentz scalars will always be linear combinations of nested, continuous fractions. This structure is preserved by applying the iterative method outlined in figure 2.2 for any amount of particles.

```
// STEP 1 //
DOUBLE RE[N];        // Rest Energy
DOUBLE EF[N];        // Effective Energy
DOUBLE P[N][3];      // Position
DOUBLE G_C = Δ;      // Reference Energy
DOUBLE lorentz_scalar[N];

// STEP 2 //
FOR(INT A = 0, A < N, A++) {
  y_temp = 0;

  FOR(INT B = 0, B < N, B++) {
    IF(A != B) {
      dx = P[A][0] - P[B][0];
      dy = P[A][1] - P[B][1];
      dz = P[A][2] - P[B][2];
      D = sqrt(dx*dx + dy*dy + dz*dz);

      y_temp += RE[B]/D; }
  }

  lorentz_scalar[A] = 1+y_temp/G_C;

  // STEP 3 //
  EF[A] = RE[A]/lorentz_scalar[A];
}

// STEPS 4-5 //
WHILE(KEEP_ITERATING == TRUE) {
 FOR(INT A = 0, A < N, A++) {
   y_temp = 0;

   FOR(INT B = 0, B < N, B++) {
     IF(A != B) {
       dx = P[A][0] - P[B][0];
       dy = P[A][1] - P[B][1];
       dz = P[A][2] - P[B][2];
       D = sqrt(dx*dx + dy*dy + dz*dz);

       y_temp += EF[B]/D; }
   }

   EF[A] = RE[A]/(1+y_temp/G_C);
 }
}
```

Figure 2.2. C-code for calculating the effective vacuum field of composite objects with first order methods.

The exact vacuum field can be determined by applying the proper, active transformation (**163**) to each particle.

$$r'_n = r_n + \frac{1}{\Delta} \int_0^{r_n} \left(\sum_{m=1}^N \bar{\nabla}_{mn}(r_n) \right) dr_n \qquad (163)$$

When the first-order approximation was defined, γ_g was held constant; i.e. the transformed radius (**164**) in all directions became isotropic.

$$r'_n = \int_0^{r_n} \gamma_{g,n}(r_n)\delta(r_n)\,dr_n = r_n\gamma_{g,n}(0) \qquad (164)$$

The exact vacuum field cannot be obtained without the unified field theory, which defines ∇_{mn}. The far-field approximation is instead applied, which is in agreement with classical theory. The far-field approximation however naturally has singularities, so each particle's field must have a cut-off (**165**) when $\bar{\nabla}_{mn}$ surpasses the maximum quantized value or classical energy.

$$\bar{\nabla}_{mn} = \begin{cases} \bar{\nabla}_{mn} & : \bar{\nabla}_{mn} \leq \bar{\nabla}_{max} \\ \bar{\nabla}_{max} & : \bar{\nabla}_{mn} > \bar{\nabla}_{max} \end{cases} \qquad (165)$$

Now that the fields are finite at all points, it is possible to integrate along the effective field of each. For an exact solution, memory requirements drastically increase since the effective field of each particle must be known at each point in space. This is because each particle's field is relative to the background field of all other particles and free fields. This can be optimized by assuming many particles exist, so that the influence one has on the others is negligible. Therefore, only one effective field is defined based upon the contribution from all particles; i.e. a continuum approximation is made similar to EFEs. Identical numerical methods can be applied with respect to figure 2.2, where the initial configuration converges towards the effective field.

2.7. Relativistic Pressure and Bulk Flow

Temperature is a scalar quantity that depicts a system's internal kinematic energy. For a system at equilibrium, the energy distribution of individual particles is related to temperature via the Maxwell-Juttner equation (**166**)[AG].

$$f(\gamma) = \gamma\sqrt{\gamma^2 - 1}\frac{e^{-\gamma/\theta}}{\theta K_2(1/\theta)} \qquad (166)$$

$K_2(z)$ is a modified Bessel function of the second kind (**167**) and $\theta = k_B T/E_0$.

$$: K_2(z) = \frac{z^2}{3}\int_1^\infty e^{-zx}(x^2 - 1)^{3/2}\,dx \qquad (167)$$

The average Lorentz scalar for the Maxwell-Juttner equation (**166**) is calculated via (**168**).

$$\gamma_{avg} = 3\theta\frac{\int_1^\infty \gamma\left(e^{-\gamma/\theta}\gamma\sqrt{\gamma^2 - 1}\right)d\gamma}{\int_1^\infty e^{-k/\theta}(k^2 - 1)^{3/2}dk} \qquad (168)$$

For the classical limit, (**168**) can be approximated by Taylor expansion resulting in (**169**).

$$\gamma_{avg} = \frac{3}{2}\theta + 1 = \frac{3}{2}\frac{k_B T}{E_0} + 1 \qquad (169)$$

This reduces to the classical relation between average kinematic energy and temperature (**170**).

$$E_k \cong \frac{3}{2}k_B T \qquad (170)$$

By applying the Maxwell-Juttner equation, the average kinematic energy of particles does not remain proportional to temperature. Therefore, the kinematic energy must be related to the proper force or pressure instead. When dealing with pressure at the atomic scale, a particle that collides with a perpendicular wall will experience a change in momentum via (**171**).

$$\Delta p_x = 2m_0 c\sqrt{\gamma^2 - 1} \qquad (171)$$

The number density depicts the amount of particles per unit volume. Normalizing this so there is only one particle per finite volume (V) allows the metric to be determined. For objects at equilibrium, each particle will be confined to its own respective volume. The one-dimensional force on the plane of another particle's volume is defined by (**172**).

$$f_x = \frac{m_0 c^2}{V^{1/3}}\frac{(\gamma^2 - 1)}{\gamma} = \frac{E_0}{V^{1/3}}\left(\gamma - \frac{1}{\gamma}\right) \qquad (172)$$

Proper pressure assumes that the particle has an equal probability of hitting the other two walls; i.e. the proper pressure is (**173**).

$$P = \frac{E_0}{3V}\left(\frac{E}{E_0} - \frac{E_0}{E}\right) = \frac{m_0\gamma v^2}{3V} = \frac{E\beta^2}{3V} = \frac{\epsilon\beta^2}{3} \qquad (173)$$

Temperature is related to pressure by an averaged Lorentz scalar (**267**), determined from the beta factor ($\beta = v/c_0$) and proper energy density (ϵ). Pressure itself is only dependent upon average particle energy and the volume attributed to each.

With the averaged Lorentz scalar, the effective field due to pressure can be determined. A massive particle moving with respect to a field will have a vacuum field defined by (**174**).

$$\overline{\mathbb{V}}(r,\theta) = \frac{E_0\gamma}{r}\frac{1}{\sqrt{(\gamma\cos\theta)^2 + \sin^2\theta}} \qquad (174)$$

Since each particle's velocity has an arbitrary direction, the field must be averaged over $d\Omega$. As with section (**2.4**), the coordinates are reoriented so that the correct integral is (**175**).

$$\overline{\mathbb{V}}_{avg} = \frac{E_0}{4\pi r}\int_{d\Omega}\frac{\gamma\sin(\varphi)\,d\theta d\varphi}{\sqrt{(\gamma\cos\varphi)^2 + \sin^2\varphi}} \qquad (175)$$

Integrating over $\theta: [0, 2\pi]$ and $\varphi: [0, \pi]$ provides the averaged field for each particle (**176**) with respect to the statistical distribution of velocities (**168**).

$$\overline{\mathbb{V}}_{avg} = \left(\frac{E_0\gamma}{2r}\right)\frac{LN\left(\gamma^2 + \sqrt{\gamma^4 - 1}\right) - LN\left(\gamma^2 - \sqrt{\gamma^4 - 1}\right)}{\sqrt{\gamma^4 - 1}} \qquad (176)$$

Reducing an object to its individual particles allows the effective field to be approximated with the iterative methods discussed in section (**2.6**). Determining the effective field of a gas under bulk flow requires a vector field ($\vec{\boldsymbol{v}}$) relative to the space-time metric. Considering a system of particles under bulk flow, the effective field of each particle must be relative to the effective field of all others. Bulk flow is therefore the transportation of kinematic energy density along the space-time metric. The averaged distribution of velocities from (**166**) must be properly added to the bulk flow ($\vec{\boldsymbol{v}}$). This is equivalent to applying a Lorentz boost in arbitrary directions of $\vec{\boldsymbol{u}}$. Under the assumption that bulk flow moves freely in the forward direction, the problem can always be reduced to an addition of velocities. Proper velocity addition relative to the angle between a particle's velocity ($\vec{\boldsymbol{u}}$) and bulk flow ($\vec{\boldsymbol{v}}$) is (**177**)[B].

$$
\vec{\boldsymbol{u}} \oplus \vec{\boldsymbol{v}} = \frac{\vec{\boldsymbol{u}}\left[1 + \frac{v}{u}\cos(\theta)\left(1 - \frac{1}{\gamma(u)}\right)\right] + \frac{\vec{\boldsymbol{v}}}{\gamma(u)}}{1 + uv\cos(\theta)} \quad (177)
$$

The first step is determining the final velocity relative to the metric after applying (**177**) for all directions of $\vec{\boldsymbol{u}}$. This can be accomplished with an active rotation derived from the Rodrigues' rotation formula (**178**)[AH]. $\vec{\boldsymbol{K}}$ is the axis of rotation and $\mathbf{M} = \boldsymbol{K}\boldsymbol{K}^T$; the trigonometric functions are written as $\sin(x) \to S_x$ and $\cos(x) \to C_x$ to shorten notation.

$$
\mathbf{R} = S_\alpha \begin{bmatrix} 0 & -K_3 & K_2 \\ K_3 & 0 & -K_1 \\ -K_2 & K_1 & 0 \end{bmatrix} + C_\alpha(\mathbf{M} + \mathbf{I}) + \mathbf{M} \quad (178)
$$

By restricting the axis of rotation to the x-y plane and applying a 2-dimensional rotation to $\vec{\boldsymbol{K}}$, (**177**) can be mapped to the unit sphere (**179**).

$$
\mathbf{R} = \begin{bmatrix} C_\beta{}^2 + C_\alpha S_\beta{}^2 & S_\beta C_\beta(C_\alpha - 1) & -S_\alpha S_\beta \\ S_\beta C_\beta(C_\alpha - 1) & S_\beta{}^2 + C_\alpha C_\beta{}^2 & -S_\alpha C_\beta \\ S_\alpha S_\beta & S_\alpha C_\beta & C_\alpha \end{bmatrix} \quad (179)
$$

Since the choice of $\boldsymbol{u_0}$ is arbitrary, it will be set parallel to the bulk flow vector field ($\vec{\boldsymbol{v}}$). Therefore, the proper velocity of each particle under the (α, β) parameterization is (**180**).

$$
\vec{\boldsymbol{w}} = \frac{u + vC_\alpha\left(1 - \frac{1}{\gamma(\boldsymbol{u})}\right)}{1 + uvC_\alpha} \begin{bmatrix} -S_\alpha S_\beta \\ -S_\alpha C_\beta \\ C_\alpha \end{bmatrix} + \frac{\left(\frac{v}{\gamma(\boldsymbol{u})}\right)}{1 + uvC_\alpha} \begin{bmatrix} 0 \\ 0 \\ 1 \end{bmatrix} \quad (180)
$$

From the composite velocities, the effective field for each is defined as (**181**).

$$
\bar{\mathbb{V}}(x', y', z') = E_0\left(\left(\frac{x'}{\gamma(\boldsymbol{w})}\right)^2 + \left(\frac{y'}{\gamma(\boldsymbol{w})}\right)^2 + (z')^2\right)^{-1/2} \quad (181)
$$

However, the coordinates within (**181**) are with respect to the direction $\vec{\boldsymbol{w}}$. These must be mapped back to the reference frame, where the bulk flow $\vec{\boldsymbol{v}}$ is defined. This can be accomplished by finding the parameters of the mapping from the direction of $\vec{\boldsymbol{w}}$ to the z-axis via (**182**).

$$
\begin{bmatrix} w_x \\ w_y \\ w_z \end{bmatrix} = \begin{bmatrix} C_b{}^2 + C_a S_b{}^2 & S_b C_b(C_a - 1) & -S_a S_b \\ S_b C_b(C_a - 1) & S_b{}^2 + C_a C_b{}^2 & -S_a C_b \\ S_a S_b & S_a C_b & C_a \end{bmatrix} \begin{bmatrix} 0 \\ 0 \\ \|w\| \end{bmatrix} \quad (182)
$$

After obtaining (a, b), the transformed coordinates are determined via (**183**).

$$
\begin{bmatrix} x' \\ y' \\ z' \end{bmatrix} = \begin{bmatrix} C_b{}^2 + C_a S_b{}^2 & S_b C_b(C_a - 1) & -S_a S_b \\ S_b C_b(C_a - 1) & S_b{}^2 + C_a C_b{}^2 & -S_a C_b \\ S_a S_b & S_a C_b & C_a \end{bmatrix} \begin{bmatrix} x \\ y \\ z \end{bmatrix} \quad (183)
$$

Inserting the solutions from (**183**) into the primed coordinates of (**181**) provides $\bar{\mathbb{V}}(r, \theta, \varphi, \alpha, \beta)$. The last step involves integrating over the various configurations in order to arrive at the averaged vacuum field (**184**).

$$
\bar{\mathbb{V}}_{avg}(r, \theta, \varphi) = \frac{1}{4\pi} \int_0^{2\pi} \int_0^{\pi} \bar{\mathbb{V}}(r, \theta, \varphi, \alpha, \beta) \, d\alpha \, d\beta \quad (184)
$$

The problem can also be viewed as a super-position of an infinite number of configurations relative to each ($\vec{\boldsymbol{u}}$). With spherical point picking, a finite amount of these can be rotated in a 3-dimensional space and averaged.

3. The Universe

The big bang theory is currently the most widely accepted cosmological model, with the 2011 Nobel Prize awarded for the discovery of accelerated expansion[BM]. The model however contains several anomalies, unexplained observations and various non-classical assumptions. These aspects can be resolved by abandoning an expanding model in favor of one that is simultaneously expanding and contracting, i.e. a steady state. Current observations are already sufficient for ruling out an expanding universe. Difficulty of arriving at such conclusion arises from the recent acceptance of non-classical assumptions and lack of theoretical constraints. Dark energy for example is not predicted by the standard model and cannot be directly detected. It is widely assumed dark energy exists solely because it allows an expanding model to fit redshift versus distance modulus. The inferred expansion however is an illusion from the local deflection of geodesics, which produces a nearly spherical projection.

With insight from recent observations, aspects that conclusively rule out an expanding universe can be focused upon. Two characteristics that stand out are incorrect predictions of large-scale curvature and the perspective of time versus redshift; these are discussed throughout sections (**3.3**, **3.5**). It is proven that the observed abundance of faint blue galaxies is due to ΛCDM's incorrect predictions for the curvature of the universe. Additional constraints allow all explanations for the $2 - 3x$ abundance of faint blue galaxies to be ruled out. These range from evolution of the local luminosity function to drastic mergers. ΛCDM further underestimates the size of the faint blue galaxies by $2 - 5x$ relative to their angular size versus luminosity. Number densities of weak MgII absorbing galaxies in section (**3.6**) are also in agreement with the prior conclusion. These incorrect predictions by ΛCDM result in systematic lensing errors as discussed in section (**3.4**).

Since all explanations can be ruled out relative to ΛCDM, the faint blue galaxy abundance is proof rather than evidence. Although proof exists against ΛCDM, there also exists strong evidence against an expanding universe. The purposed theory predicts for distant galaxies to be older than local ones. An expanding model predicts the opposite, which is contrary to observations. For example, galaxies are observed to cool with increasing redshift. Distant quasars contain relatively higher FeII:MgII ratios, depicting increased metallicity with redshift. There are many other firmly grounded observations not compatible with an expanding universe such as the in-fall velocity of the Bullet cluster. For clarity, the first half of chapter **3** will focus on the foundations of the continuous model. The remaining sections discuss the various proofs against ΛCDM, including a statistical comparison between models.

The new cosmological theory only requires the standard model and corrections to general relativity herein. From this short introduction alone, the new model is superior with respect to Occam's razor. In other words, the simplest theory that agrees with all observations is the correct theory. Similar to initial motivation behind an expanding model, the shape of the universe can be fit with a single constant. The inferred accelerated expansion is nothing more than local geodesics deflecting towards the center of an asymptotically flat, linear universe. Dark energy is therefore not required to explain redshift versus distance modulus. The trend is better fit by distant galaxies falling into an asymptotically flat universe, depicted by relativistic redshift and gravitational acceleration. The cosmic background radiation must therefore originate from the central region of an asymptotically flat universe. Classical assumptions insist that this black body radiation is emitted from a central core, which is not compatible with theories that predict event horizon such as EFEs.

3.1. The Big Bang Theory

Georges Lemaitre, a Belgian priest, was the first to purpose the big bang theory, originally named "hypothesis of the primeval atom"[AK]. Although Lemaitre was the first to discover the "Hubble constant", it was named after Edwin Hubble. Hubble's observations in 1929 also showed a linear relationship between the distance and redshift of local galaxies[AL]. The Hubble constant and linear trend provided the initial motivation behind an expanding model, where redshift is attributed to the recession velocity of local galaxies. According to the Hubble model, the relation between redshift and metric distance is (**185**).

$$d' = \frac{c}{H_0}\left[\frac{(z+1)^2 - 1}{(z+1)^2 + 1}\right] = \frac{v}{H_0} \qquad (185)$$

Due to the inverse square law, metric distance is related to distance modulus (μ) by equation (**186**).

$$d' = 10^{\mu/5+1} \qquad (186)$$

Combining equations (**185**, **186**) and subtracting the result from observations, the disagreement becomes apparent. Figure 3.1 provides the error relative to the initial big bang model.
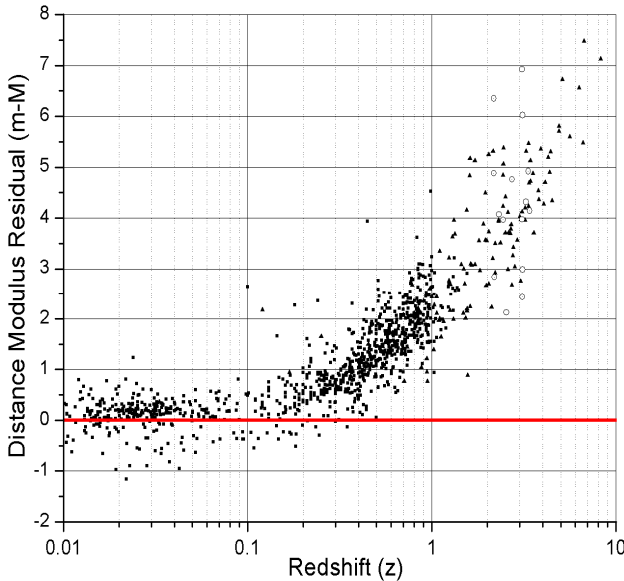
Figure 3.1. Data is from the NED database[AJ] and linear trend from equation (**185**) with $H_0 = 73.8\,(km/s)/Mpc$ [AI].

The initial big bang model is only valid under Hubble's and Lemaitre's limited observations, i.e. for local galaxies with redshift below $z \approx 0.15$. It is clear that beyond this point, an expanding universe depicted by the big bang theory would need to be accelerating. Assuming the universe began as a point of infinite energy density that consequently erupted into an expanding sphere of energy, there are two plausible scenarios for recession velocity. For a homogenous universe, any initial acceleration from pressure or bulk flow should be constrained to relatively high redshift. Therefore, the first scenario requires that the mass of the universe is large enough to collapse back onto itself. The second assumes the kinematic energy imparted to matter from a big bang event is large enough to continue expansion at a constant or decreasing rate. Neither possibility fits observations, requiring the ad-hoc introduction of dark energy.

From the previous chapters, several constraints have been placed upon vacuum field theory. These include the conservation of vacuum energy density, its connection to the space-time metric and the localized nature of particles. With these additional aspects, it is clear dark energy has characteristics similar to vacuum energy density. For example, dark energy in ΛCDM does not force matter to become repulsive; it instead acts to expand the space-time metric. This only provides the illusion of acceleration since all observers view the universe relative to the space-time metric. With respect to only experimentally confirmed contributions to an object's redshift, there exist two explanations for current observations. Either the universe consists almost entirely of undetectable energy and matter causing accelerated expansion, or this improperly inferred expansion is an illusion due to the universe being asymptotically flat. It is therefore important to distinguish between the angular scales and time-dependence of each model.

3.2. Redshift and Distance Modulus

The redshift of distant objects can be described in terms of relativistic redshift due to a variation in gravitational potential. Vacuum field theory is not required for determining redshift versus distance; however, it is necessary for large-scale curvature. The relation $\gamma = \gamma_g$ is applied to determine the average relative velocity (**187**) that is induced from a change in vacuum energy density between source and local observer.

$$v = \left(\frac{c_0}{\frac{\nabla}{\Delta}+1}\right)\sqrt{\frac{\nabla}{\Delta}\left(\frac{\nabla}{\Delta}+2\right)} \qquad (187)$$

The Doppler effect requires for any relative velocity to result in a redshift (**188**).

$$z_1 = \sqrt{\frac{1+\beta}{1-\beta}} - 1 \qquad (188)$$

Plugging equation (**187**) into (**188**) results in the relativistic redshift (**189**) from a change in ∇.

$$z_1 = \frac{1}{\Delta}\sqrt{\left(\sqrt{\nabla(\nabla+2\Delta)}+\nabla+\Delta\right)^2 - 1} \qquad (189)$$

There is also a general redshift due to variations in vacuum energy density, i.e. the second component is defined by (**190**).

$$z_2 = \frac{\nabla}{\Delta} \qquad (190)$$

Summing both components results in the effective redshift (**191**) for distant galaxies and clusters.

$$z_{net} = \frac{1}{\Delta}\left(\sqrt{\nabla(\nabla+2\Delta)}+2\nabla\right) \qquad (191)$$

The above relation has a single free variable and depicts a nearly perfect linear trend for all non-local redshift. This not only provides strong evidence for an asymptotically flat universe, but also justifies the linearity of vacuum field theory.

From numerical methods, it is observed that an asymptotically flat universe will generate a field that appears nearly linear with respect to metric distance or local observers. When this is integrated to provide a plot of metric distance versus vacuum energy density, the field becomes approximately linear. Applying equation (**191**) to the spectral redshift of distant SNIa/GRB demonstrates a linear trend as depicted in figure 3.4. Prior to discussing actual data from SNIa and GRB observations, an ensemble of asymptotically flat universes (**192**) is provided in figure 3.2.

$$\nabla(r) = \frac{E}{r^n} \qquad (192)$$

They demonstrate that any realistic, asymptotically flat universe will appear nearly linear relative to a local observer or space-time metric.
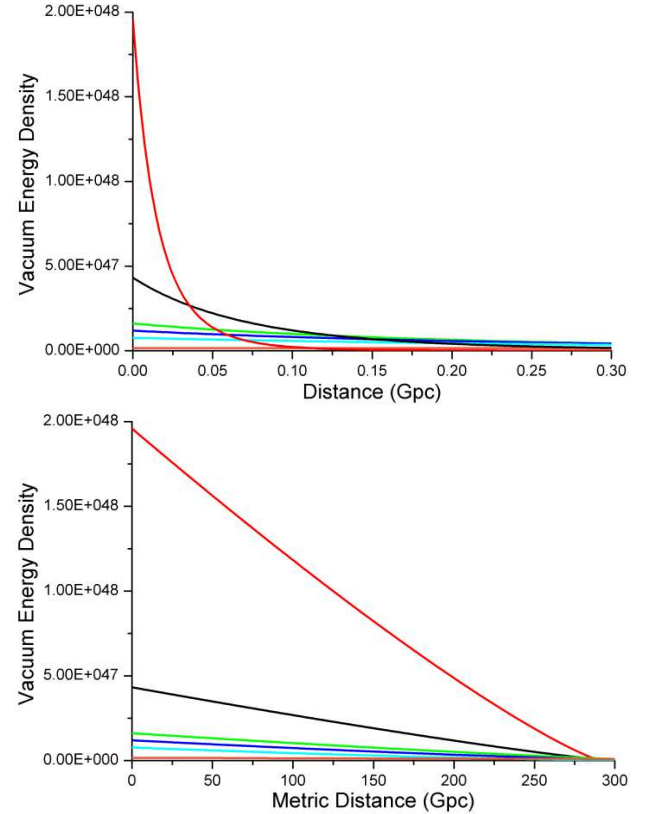
Figure 3.2. Each function (**192**) is indexed by the following colors n = 1, 2, 3, 4, 5, 6. Total metric distance is held at approximately 300 Gpc. (Top) Ensemble of asymptotically flat universes relative to the preferred reference frame and (Bottom) relative to local observers or metric distance.

The derivative of figure 3.2 with respect to metric distance provides a more accurate representation of the linear variations in figure 3.3. This linear trend is crucial for explaining dark energy or the illusion of accelerated expansion. From the NED database, metric distance to each object is determined from distance modulus. The previous net redshift relation (**191**) is then applied to the data, resulting in figure 3.4. The best fitting trend is with respect to data beyond 0.15z, which results in a constant slope of $S_0 = 3.248 \pm 0.047 \cdot 10^{42} \, (kg \, m \, s^{-2})/Gpc$ and y-intercept $y_0 = 0.375 \pm 0.161 \, Gpc$. Since the flow towards central core is directionally dependent, the y-intercept depicts the average distance to the start.
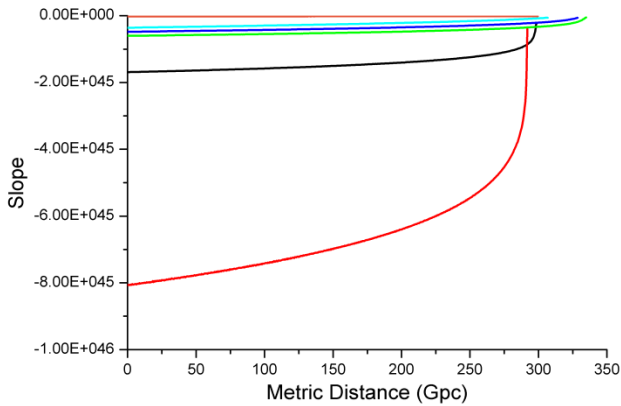
Figure 3.3. The slope of each function has origin at the center of the universe. Note that the deviations are minimal when the observer is inside the localized universe, becoming less linear as the edge is approached.
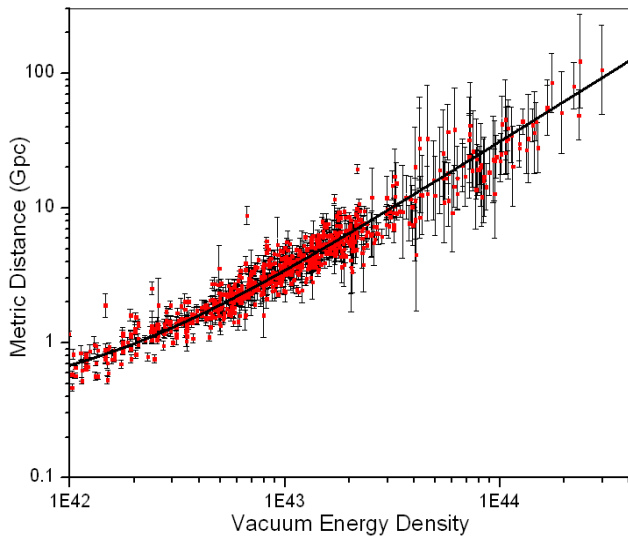
Figure 3.4. Logarithmic plot of metric distance versus vacuum energy density with respect to Earth.

From the linear slope relative to the space-time metric, an upper limit on metric or luminosity distance to the central core can be determined. The slope may slightly vary as the core is approached; however, this is not noticeable within currently observable distances ($< 100 \, Gpc$). From analyzing the redshift of the core's black body spectrum, the vacuum energy density at the surface is determined with respect to the local space. In other words, the observed spectrum is shifted until it matches the spectral distribution at emission. The core is found to have a redshift of $z \approx 1089$ with a surface temperature around $3000 K^{[AN]}$. Since this form of redshift is solely due to variations in vacuum energy density, the change in ∇ can be determined from equation (**193**).

$$\nabla = \Delta z \tag{193}$$

Therefore, the variation in vacuum energy density from Earth to the core's surface is approximately $1.315 \cdot 10^{47} (kg \cdot m \cdot s^{-2})$. With the best fitting linear slope (all data beyond $z > 0.15$), the maximum metric distance to the central core is determined from equation (**194**).

$$S_0 d' = \nabla = \Delta z \tag{194}$$

Solving for d' places the core's surface at a metric distance of about $40.6 \, Tpc$. Modern telescopes are only capable of detecting light from the most luminous objects up to $0.1 \, Tpc$, i.e. a small portion of the universe is observable. For comparison, the far-field of a universe with perfect linear slope relative to metric distance can be written as an exponential function (**195**), where ∇_0 is the vacuum energy density at the observer's position. With respect to the ensemble plotted in figure 3.2, the function has a different form. However, they all produce nearly constant slopes relative to a local observer or metric distance.

$$\nabla(r) = (S_0 d' + \nabla_0 + \Delta)e^{-rS_0/\Delta} \tag{195}$$

Relative to an asymptotically flat universe and observed cosmic background radiation (CMBR), it is clear that something large has or had existed prior to the present. If distant galaxies and clusters are falling into an asymptotically flat universe, then there must be a mechanism that transports matter from the central region outwards. A situation similar to that of an explosion is not completely out of the question. However, a mechanism already exists that can replace spherical expansion. Relativistic jets emanating from black holes are not well understood, but have been observed from numerous sources with varying intensity and duration[AM]. The first step in producing the model that agrees with all observations is assuming the local space emerged from such jet. In this perspective, distant galaxies and clusters fall back into the equatorial regions of the central core at relativistic speeds. Due to the conservation of momentum, in falling matter is ejected at the polar regions in the form of dense quark matter. This quark matter further decays into hot, x-ray emitting gas commonly seen in young clusters and galaxies. The local jet is later discussed in section (**3.8**) with respect to the dark flow and cleaned CMBR image.

Black holes that emit polar jets are known to exist after such events. When considering finite black holes, the best approximations available are QCD and vacuum field theory. If the CMBR is to be taken as black body radiation from a massive but cooled object, then the surface must be finite. One could argue that Hawking radiation is already theorized to be emitted from the surface of non-finite black holes. However, temperature in this perspective is inversely proportional to mass. For an Einstein black hole to emit a 3000K blackbody temperature, it would need to be several orders of magnitude less massive than the Moon. This is clearly impossible with respect to a central core, as countless black holes exist locally that are much more massive. Although the various proofs against

an expanding universe have not yet been discussed, they would clearly nullify current interpretations of the CMBR. In other words, the CMBR cannot be due to a period of recombination. It is instead classical black body radiation emitted from the central core. In an asymptotically flat universe, geodesics will begin to deflect from the local space as distance increases. After sufficient distances, the majority of local geodesics will turn towards the center of the universe. Although the projection is not perfectly spherical, it creates the illusion of accelerated expansion. The CMBR is therefore projected onto all local directions of space, as it originates from the center of the universe.

Putting all of the pieces together, a self-consistent model of the universe emerges in figure 3.5. For any steady state model to be valid, the universe must conserve energy and act as a perpetual machine. Other models similar to the cyclic big bang inherently describe the universe as such. However, they suffer from incorrect large-scale curvature similar to ΛCDM. This is later discussed relative to the size and number densities of distant galaxies. Galactic merger times and properties of distant clusters also insist that the universe is in a steady state. In other words, there is a constant flow of matter from the central core to the outer regions, which further flows back to the central region. This requires for distant galaxies and clusters to be older than local populations when observed from Earth.
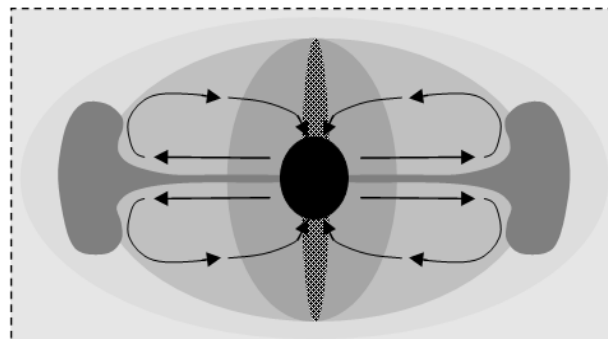
Figure 3.5. A cross section of an asymptotically flat universe in a steady state. The structure takes the form of a Y_2^0 spherical harmonic with two polar jets and annihilation boundary between hemispheres.

3.3. Revised Galaxy Evolution

As inferred from section (**3.2**), distant galaxies are older than local populations. This is contrary to an expanding model, where objects are predicted to be younger as redshift increases. Distant galaxies and clusters with respect to Earth should therefore contain higher fractions of cold baryonic matter, increased star formation rates and high metallicity. Relative to the local space, galaxies and clusters display characteristics that are evident of an origin from hot, x-ray emitting gas. The x-ray emitting gas is the product of decaying quark matter as inferred from its connection to the dark flow. Both ΛCDM and the purposed model are similar in the sense that the local space emerged from dense quark matter. Relative to an expanding model, it is expected that high redshift clusters and galaxies are hotter than similar local populations; observations however depict the exact opposite. For example, local x-ray emitting clusters transform into lyman-alpha blobs beyond $2z$. To temporary resolve this problem, it is usually assumed that drastic major mergers take place and heat up the intergalactic medium. However, it is illogical to have two cool clusters with high metallicity merge into a single hot cluster with low metallicity.

As the local jet of quark matter begins to cool and expand, it decays into a dense non-metallic gas. The oldest stars known to date are metal poor, indicating that they formed some time after this phase. All elements heavier than helium are usually produced through nuclear fusion. The following population II stars are abundant in both globular clusters and elliptical galaxies[AP]. Most elliptic galaxies contain only population II stars and large amounts of x-ray emitting gas[AT]. The source of x-rays $(0.5 - 1.5\ keV)$ is thermal bremsstrahlung due to hot ionized gas (5 to $> 15\ keV$)[AZ]. Young stars often undergo supernova after billions of years, enriching the surrounding medium with metallic elements. Around this point, the x-ray emitting gas originating from the core's relativistic jet begins to drastically cool. Metal-rich population I stars then form in the dense but cooler regions of galaxies and nebulas. Beyond Earth's current position in the flow, baryonic matter is observed to become increasingly colder and more metallic. Due to the abundance of preferred fuel[AQ], galaxies between a redshift of $0.5z - 3z$ will demonstrate intense star formation[AR]. Late-type galaxies commonly have regions of active star formation, which is favored due to cold, dense baryonic matter[AQ][AU]. The cold interstellar gas required to ignite these galaxies was recently observed. A letter to Nature states that galaxies at redshift of $1.2z$ and $2.3z$ consist of 34% and 44% cold baryonic matter respectively, which is $3 - 10x$ more than local late-type galaxies[AQ]. Beyond the overly abundant blue field galaxies, red and ultra-red galaxies dominate[AV][AW][AX]. The red and ultra-red colors are an indication of abundant dust or mature star populations[AX], both being characteristics of older galactic populations. Several of the distant red galaxies within the Hubble deep field image are also undergoing mergers, which is consistent with half of normal galaxies experiencing a major merger by $0.75z$.

The previous overview of star formation does not drastically differ from current models. It is instead the evolution of galaxies that must be heavily revised. Although the purposed model and ΛCDM both insist the local universe originated from dense quark matter, their perspective of time versus redshift are opposite. This will vary the inferred evolution of galaxies with respect to observations. For example, predicted time-scales drastically differ between models. To explain galactic formation with respect to ΛCDM, large amounts of dark matter are required. These processes should instead occur over $50 - 100\ Gyr$, which is why excessive amounts of dark matter are required. Time-dependence is later reinforced by comparing simulated and observed merger times; discussed in section (**3.5**).

Relative to the purposed model or ΛCDM, the initial environment will consist of decaying quark matter. Galactic formation will therefore take place in a hot, non-metallic gas. With any classical gas, the system will move towards equilibrium with respect to density and pressure. As thermal pressure is overcome by gravity, regions will begin to collapse. Due to the conservation of momentum, any radial collapse will be transferred into angular momentum. The properties of galaxies also depict an evolution from early to late-type; i.e. an older galaxy will be more metallic, contain vast amounts of cold baryonic matter and be less symmetric in shape. This transition from early-type galaxies into late-type is depicted in figure 3.6.

It is commonly debated whether disk galaxies merge to form ellipticals[AP]. However, mergers are insignificant with respect to galactic evolution prior to $1z$. A large elliptical galaxy was also discovered to contain a rotating disk of x-ray emitting gas[AS]. In addition, elliptic galaxies at $0.5z$ are observed to be on average rotating faster than those in the local space[AY]. Distributions of star populations further agree with the purposed model of evolution[BA]. Due to flawed foundations however, various modern theories must be discarded. This includes drastic merger rates and dark matter, as the cooling of x-ray emitting gas and unstable rotational curves are the mechanisms behind galactic evolution.

Approximately 60% of major galaxies are disk within the local supercluster, while the remaining are mostly elliptical. From a redshift of $0.5z - 2.0z$ intense blue galaxies dominate, which continuously transform into blue irregulars beyond $1z$[AR]. It is important to notice however that galactic evolution is minimal for those involved in the faint blue galaxy problem, i.e. ones in the range of $0.3 - 0.7z$. This includes luminosity, color and size variations. Application of modern literature must also proceed with caution, as old calculations do not take into account the proper curvature of the universe. For example, a constant number density of elliptic galaxies out to $1z$ with respect to ΛCDM[BH] would indicate a relative decrease after considering proper large-scale curvature.

Another aspect of galactic evolution arises from the statistically significant dark flow. With the bulk of galaxies and clusters falling towards the center of the universe, there must be another local flow that replenishes these populations. From WMAP, small variations in the cosmic background radiation were measured and analyzed[AZ]. These variations are due to scattering from clusters of galaxies containing large amounts of x-ray emitting gas. It is clear that hot, x-ray emitting galaxies and clusters should be younger and therefore closer to the local jet. The dark flow is therefore not only expected by the new model, but a necessity.

Figure 3.6. (**A**) Galaxies initially form from hot x-ray emitting gas, which begins to collapse after sufficient cooling. (**B**) Early galaxies obtain a preferred axis of rotation due to local or global gravitational fields. Young metal poor stars form in the bulge due to preferred density. (**C**) Young metal rich stars later form in the remaining bulge (**D**, **E**) while older populations are transported outwards due to unstable rotational curves.

Figure 3.7. (**A**) Central core with jet consisting of hot, dense quark matter. (**B**, **C**) After the quark matter decays into hot x-ray emitting gas, low metallicity clusters, galaxies and stars begin to form. (**C**, **D**) Figure 3.6 overviews galactic evolution. (**E**) Increased merger fractions, metallicity and cold baryonic matter with respect to the local space.

The last part of this section will focus on deriving the time dependence of distant galaxies and clusters. Since all objects not in the dark flow will be falling into an asymptotically flat universe, the redshift equation can be applied to determine kinematics. The goal is to approximate the total amount of proper time a galaxy experiences while following a geodesic originating from Earth's present position, i.e. the reference frame is relative to Earth. Metric distance (**196**) is defined from the slope of the universe and y-intercept, although only the slope depicts the actual shape.

$$d' = (3.0788 \cdot 10^{-43})\mathbb{V} + 0.3748 \quad (\textbf{196})$$

Solving equation (**196**) in terms of vacuum energy density results in equation (**197**).

$$\mathbb{V} = (3.248 \cdot 10^{42})d' - 1.217 \cdot 10^{42} \quad (\textbf{197})$$

Plugging equation (**197**) into the redshift equation (**191**) provides the relation between redshift and metric distance. Directional dependence for local redshift however must also be considered, where the y-intercept provides the average distance to the start of flow towards central core.

To determine the time dependence of non-local galaxies, the change in redshift with respect to proper time must be determined. Each distant galaxy or cluster relative to Earth took τ amount of proper time to arrive at the position where currently observed light was emitted. Therefore, the time it took for a light ray to travel from source to observer is not necessary relative to a steady state model. Directional dependence for local redshift (<0.2z) can also be considered by varying y_0 from 0 to $0.54\ Gpc$. For all directions relative to Earth, the average change in vacuum energy density between the start of flow (d'_0) and finite amount of metric distance (D') is defined as (**198**).

$$\Delta\mathbb{V} = (3.248 \cdot 10^{42})D' \quad (\textbf{198})$$

From the initial position, a change in vacuum energy density can be made relative to the averaged start of flow at $d' \cong 0.375\ Gpc$. After normalizing units ($\Delta = 1$), the y-intercept can be negated by applying $\mathbb{V} = 0.02683 \cdot D'$. The normalized redshift equation (**199**) is then applied to relate an objects spectral redshift to a variation in metric distance D' with respect to Earth.

$$z_{net} = \sqrt{\mathbb{V}(\mathbb{V}+2)} + 2\mathbb{V} \quad (\textbf{199})$$

Since galactic evolution is relative to proper time, proper velocity must be applied (**200**).

$$u = \frac{dx'}{d\tau} = v(\mathbb{V}+1) = c_0\sqrt{\mathbb{V}(\mathbb{V}+2)} \quad (\textbf{200})$$

With both (**199**, **200**), the proper velocity and redshift are coupled to metric distance (D') as the only free variable. The proper velocity versus redshift provides all information necessary in order to determine the duration of proper time a distant object has experienced. Proper velocity is relative to the amount of metric distance traveled with respect to a moving objects perspective of time. The averaged proper velocity over metric distance D' is (**201**). Carrying out the integral of equation (**201**) and applying the relation $u_{avg} = \Delta x'/\Delta\tau$ provides the total proper time each galaxy has experienced without considering directional dependence.

$$u_{avg} = \frac{1}{D'}\int_0^{D'} u(D')\, dD' \quad (\textbf{201})$$

It is also important to realize that younger galaxies and clusters exist with respect to the local jet, observed in the form of the dark flow. Neither Hubble's law nor the new redshift equation are capable of modeling this since it has a separate origin. Therefore, the error with respect to the relative age of local objects becomes large due to this uncertainty. However, the majority of objects will follow the previously derived time dependence.

Due to matter emerging from and falling back towards the central core at relativistic speeds, there must be a turning point where relative motion is minimal. The CMBR dipole moment provides a velocity of $627 \pm 22 \ km \ s^{-1}$ for the local group[AZ]. This is approximately 0.209% the speed of light, which is both insignificant and expected for regions that are distant from the central core. If the metric distance from Earth's current position to the central core is about $40.6 \ Tpc$, the most distant 98% of metric space would account for only 7.8% of all proper time experienced. The most distant objects currently observable are approximately 140 billion years older than the local group ($z \approx 8.0z$). For comparison, the Sun would take about 100 billion years to consume all of its hydrogen fuel. Although this would not actually occur, it is clear that the depletion of interstellar hydrogen occurs over long time-scales. For example, UDFy-38135539 is a distant galaxy observed in the Hubble Deep Field and demonstrates strong lyman-alpha emission[BB]. The light being emitted by the object is passing through dust that has been reionized beyond what can be explained by an expanding model. The presence of neutral hydrogen gas would only be plausible if the universe is cooling as redshift increases. In addition, the galaxies redshift ($8.55z$) would correspond to a proper age of about $144 \ Gyr$ with respect to the local group.

Since baryonic matter is already observed to be cooling from the local region up to $2.3z$, evidence supports the aging of galaxies with increasing redshift. This abundance of cold baryonic matter further induces intense star formation, which is observed for distant late-type galaxies ($0.5z$ to $3z$). These redshift correspond to proper times between 28 and $92 \ Gyr$ with respect to local populations. Therefore, the epoch of intense star formation is in agreement with the continuous model and expected conditions. Minimal evolution however occurs prior to $0.7z$ ($35.7 \ Gyr$), which is later discussed through-

out section (**3.5**). With respect to proper time, ΛCDM predicts that the current age of the universe is $13.75 \pm 0.13 \ Gyr$[AO]. Since Earth's position is in proximity to the CMBR dipole turning point, the total proper time experienced from the core's jet back to the surface is twice that of future proper time. From figure 3.8, the amount of proper time experienced up to the surface of the central core with respect to Earth is approximately $230 \ Gyr$. The total time experienced by an observer in the bulk of flow is therefore $460 \pm 100 \ Gyr$ relative to a complete cycle external to the core.
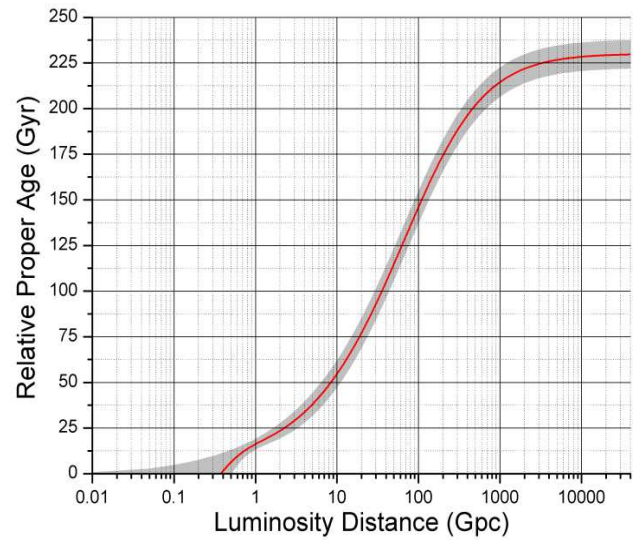
Figure 3.8. Proper age (τ) versus luminosity distance (D_L). Error is derived from uncertainty in slope, with the y-intercept ranging from $0 \ Gpc$ to $0.54 \ Gpc$.
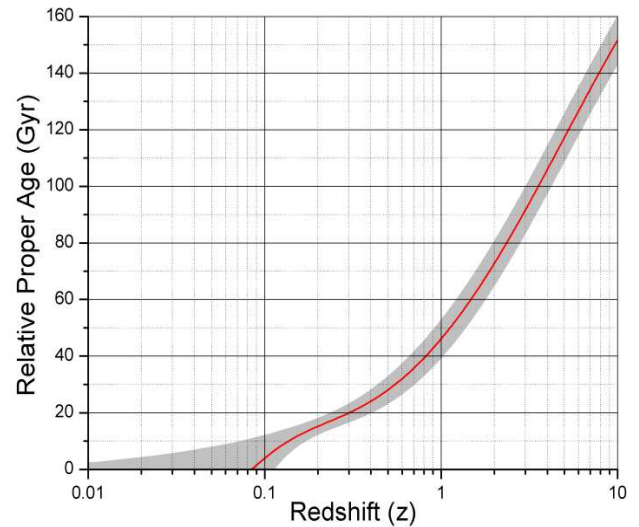

Figure 3.9. Proper age versus effective redshift with respect to Earth; constraints are identical to figure 3.8.

3.4. Angular Scales and Weak Lensing

Although many characteristics can differentiate between models, the curvature of the universe is the only one that offers conclusive proof with current observations. The angular scale versus redshift for ΛCDM was obtained from recent constraints[BN]. The angular scale or scale-factor ($kpc/''$) of an asymptotically flat universe is derived from the following method. The distance to an object is determined from its luminosity or metric distance. Considering that local geodesics begin to curve towards the center of the universe at relatively short distances, the projection of distant space will appear almost spherical relative to Earth. The only missing factor is the variations in metric volume induced by the vacuum field of an asymptotically flat universe. From vacuum field theory, the space-time metric is locally isotropic and defined by a scalar field. The circumference of a sphere projected from distant space (**202**) can therefore be scaled by γ_g relative to Earth's perspective.

$$C = 2\pi d' \gamma_g \qquad (202)$$

Figure 3.10 provides a comparison between ΛCDM and the continuous model.
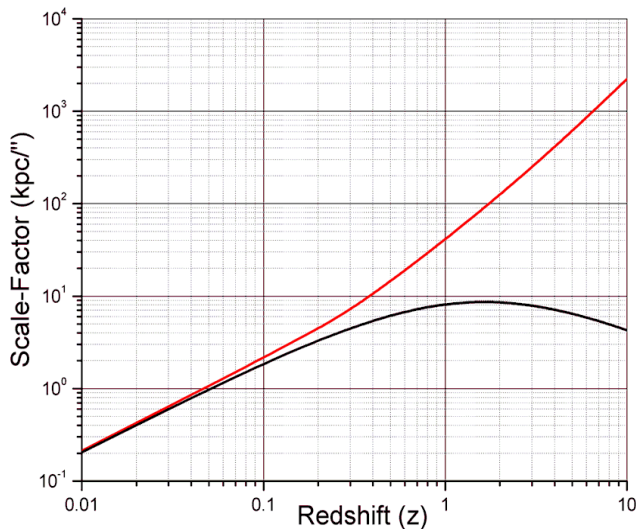
Figure 3.10. The continuous model is depicted in red with ΛCDM in black. Due to local directional dependence, Hubble expansion with $H_0 = 68.7$ is applied for redshift below $0.2z$. The continuous model however is in agreement with local redshift when applying the full range of y_0.

Plotting the scale-factor ratio between models in figure 3.11 provides several important constraints. This variation is key to ruling out an expanding universe. Although the models are opposite in several aspects, acceptance of poorly constrained hypothesis makes it difficult to rule out ΛCDM. For example, the amount of cold baryonic matter is observed to drastically increase from the local space to $1.2z$ and $2.3z$. With only classical assumptions, galaxies should cool as they age. Although mergers can heat up ISM or ICM, such drastic increase in cold baryonic matter with redshift should be taken as strong evidence against ΛCDM. The processes that occur in the cooling or heating of normal galaxies however are poorly constrained. Ruling out an expanding universe therefore requires aspects that are fully constrained. This is why the angular scales are crucial, as ΛCDM cannot explain the $2 - 3x$ excess of faint blue field galaxies or the disagreement between their size and luminosity. Incorrect predictions of large-scale curvature also induce systematic lensing errors, which currently provide the only direct evidence for dark matter. The continuous model on the other hand does not require the non-classical assumptions of dark matter and dark energy.
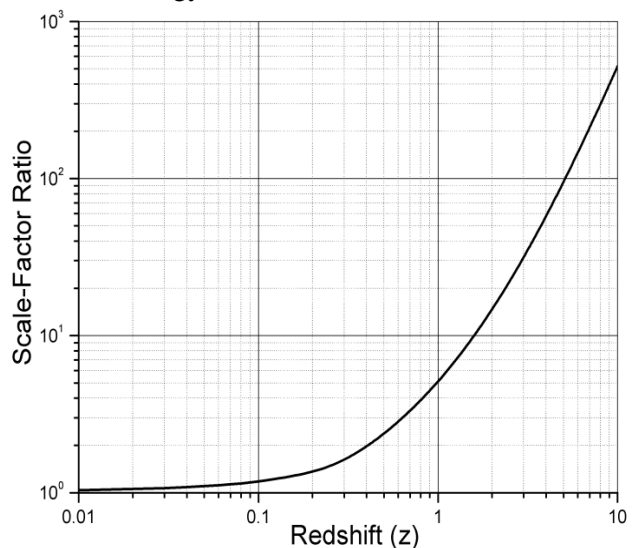
Figure 3.11. Scale-factor ratio between the continuous model and ΛCDM with respect to redshift. A $5x$ disagreement exists by $1z$ further increasing to $100x$ around $5z$.

The disagreement between each models scale-factor allows distant gravitational lenses to appear stronger than expected from only visible matter. With respect to an expanding universe, there are three distance scales. These consist of angular diameter distance (D_A), comoving distance (D_C) and luminosity distance (D_L). The angular diameter distance corresponds to the visual size of an object at a given redshift, written as (**203**)[BO].

$$D_A(z) = \frac{c_0}{H_0} \frac{1}{(1+z)} \int_0^z \frac{dz'}{\sqrt{\Omega_m(1+z)^3 + \Omega_\Lambda}} \qquad (203)$$

The remaining distances are related to bolometric luminosity and flux via (**204**)[BO].

$$D_L \equiv \sqrt{\frac{L}{4\pi F}} = (1+z)D_c = (1+z)^2 D_A \qquad (204)$$

The continuous model does not require comoving distances since the universe is in a steady state. With respect to distant galaxies and clusters falling into an asymptotically flat universe, the angular diameter distance will vary from that of ΛCDM. Distant objects in an expanding universe appear larger with respect to a flat, steady state projection. The continuous model predicts the exact opposite, where metric volume increases with distance or redshift. Distant objects will therefore appear much smaller in comparison to a flat space-time metric. Luminosity distance in this case is still equivalent to the classical flux definition; however, the angular diameter distance becomes (**205**).

$$D_A = D_L \gamma_g \cong D_L \left(1 + \frac{S_0 G_0}{c_0^4}(D_L - y_0)\right) \qquad (205)$$

The slope (S_0) was discussed in section (**3.2**), with the y-intercept (y_0) providing the average distance to the start of flow towards central core. Redshift becomes directionally dependent due to the local deflection of geodesics; on average, this distance is about $0.375\ Gpc$. The right side of equation (**205**) should therefore have D_A set equal to D_L prior to y_0.

With respect to dark matter, the only evidence for its existence is gravitational lensing from distant clusters. Although proof that the universe is not expanding is not discussed until section (**3.5**), large variations between scale-factors will clearly induce systematic lensing errors. In general, an expanding universe will overestimate distant lens efficiency with respect to visible matter. Dark matter is also self-contradictory with observations. For example, the Train Wreck cluster has lumps of dark matter that coincide with both galaxies and ICM[BP]. This is strong evidence for systematic lensing errors, as dark matter should not interact beyond gravitation. Regardless, dark matter is always located around baryonic matter. This is expected when systematic lensing errors are involved, i.e. only the visible matter existed to begin with.

Properties of the Bullet cluster with respect to ΛCDM are also contradictive, where it is claimed to be proof of dark matter[BQ]. At the same time, the existence of this cluster is not compatible with ΛCDM[BR]. Observations that are incompatible with a theory cannot be seen as proof for a specific aspect of it. The remaining reason dark matter has been inferred are the unstable rotational curves of galaxies. Assuming the virial theorem is valid in this case originates from an ad-hoc attempt at forcing observations to agree with an expanding model. This assumption is flawed as inferred from observed galactic evolution. The formation of galaxies does not begin from reionized plumes of hydrogen gas anchored to dark matter, but instead hot x-ray emitting gas. Without large amounts of dark matter, galaxies could not have formed within the time-scales predicted by an expanding model. From section 3.3, the age of the local space is well over $100\ Gyr$ more than what an expanding model predicts. This disagreement increases with redshift, where time is viewed in the reverse of actuality. The inferred existence of dark matter therefore originates from improper foundations.

A spherically symmetric lens can be applied to compare the continuous model and ΛCDM. The inferred magnification of a lens is dependent upon the angular diameter distances (D_A). As previously stated, current observations support the conclusion of systematic lensing errors, which arises from the incorrect shape of the universe. Since vacuum field theory simplifies to EFE's weak field limit, the formulation is equivalent. Therefore, the equation for a spherically symmetric lens is (**206**)[BS].

$$\beta = \theta - \frac{D_{LS}}{D_{OL}D_{OS}}\frac{4G_0M}{c_o{}^2\theta} = \theta - k\frac{4G_0M}{c_o{}^2\theta} \qquad (206)$$

The free variables are D_{OL}, D_{LS} and η; these depict the distance from observer to lens, observer to source and the horizontal offset of the source respectively. The remaining variables represent the angular offset of the source (β) and image (θ). The magnification due to a spherical lens is therefore determined by equation (**207**).

$$\mu = \frac{\theta}{\beta}\frac{d\theta}{d\beta} \qquad (207)$$

From the initial conditions, $D_{OS} = D_{OL} + D_{LS}$ and β is determined from equation (**208**).

$$\beta = \arctan\left(\frac{\eta}{D_{OS}}\right) \qquad (208)$$

Solving the lens equation (**206**) results in (**209**).

$$\theta = \frac{1}{2}\left(\beta \pm \sqrt{\beta^2 + k\frac{16G_0M}{c_o{}^2}}\right) \qquad (209)$$

Table 3.1 provides a comparison between the Train Wreck cluster (0.201z) and Bullet cluster (0.296z).

Table 3.1. *k* factor between continuous model and ΛCDM

Redshift	Continuous Model		ΛCDM	
	k (0.201z)	k (0.296z)	k (0.201z)	k (0.296z)
0.500z	0.7424	0.3487	0.6749	0.3537
1.000z	0.9574	0.5637	0.8673	0.4996
2.000z	1.036	0.6423	0.8976	0.5299
3.000z	1.055	0.6614	0.8506	0.4829
4.000z	1.063	0.6691	0.7856	0.4179
5.000z	1.067	0.6730	0.7140	0.3464

Although the disagreement between models is relatively small prior to $1z$, the systematic error becomes apparent from moderate to high redshift. The ratio of distances provides a single variable (k) that directly scales the mass in equation (**209**). This indicates that ratios between each models k is equal to the inferred abundance of mass. Figure 3.12 depicts this abundance relative to several spherical lenses. The majority of lensed sources range from $3 - 5z$, where the disagreement becomes apparent. For example, the Train Wreck cluster would be inferred to have 49% more mass at $5z$ than actually exists with respect to ΛCDM. The Bullet cluster would instead be inferred to have 94% more mass at identical redshift.

As previously discussed, the initial motivation behind dark matter originates from applying the virial theorem to disk galaxies. Unstable rotational curves and cooling of x-ray emitting gas however are the mechanisms behind galactic evolution. This is reinforced by observations of entropy, angular size, number densities and stellar populations. To avoid circular reasoning, only lensing data should be compared to the visible baryonic matter within clusters. Section (**3.5**) further demonstrates that an expanding model or ΛCDM predicts incorrect large-scale curvature. This invalidates current lensing data and claimed proof of dark matter.
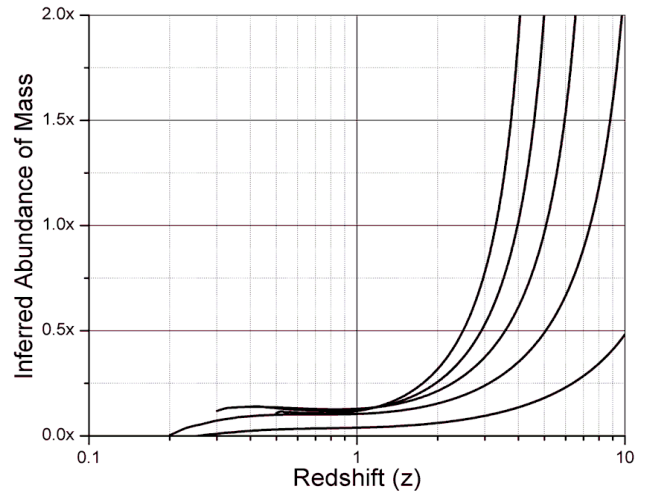

Figure 3.12. Spherical lenses are plotted from top to bottom at $0.5z$, $0.4z$, $0.3z$, $0.2z$ and $0.1z$ respectively. The abundance is relative to the continuous model versus ΛCDM.

3.5. The Faint Blue Galaxy Problem

The abundance of faint blue galaxies (FBG) up to moderate redshift is known as a grand cosmological problem[BT]. With observed merger fractions and the angular size of these galaxies, the problem can be resolved with only classical assumptions. From the LDSS deep redshift survey, an $2x$ abundance exists up to $M_B = 22.5$ with respect to no evolution[BU]. The survey provides an average redshift of $0.32z$ at $M_B = 21.8$. More distant surveys indicate an $2 - 3x$ abundance within the limits of $M_B = [22.5, 24]$[BV]. The majority of recent studies also focus on the B-band, where most of the FBGs with M_B ranging from 23 to 24 exist prior to $1.0z$[BW]. With high-resolution imaging, distant FBGs are found to be consistent with local disk and irregular galaxies[BX]. On average, this dataset provides a similar redshift versus M_B of 21.9 at $< 0.34z >$. The observed OII widths of distant FBGs also indicate intense star formation across the entire disk[BX]. Many of the local FBGs $(< 0.3z)$ however are dwarfs. To the contrary, distant FBGs are not dwarf galaxies but instead intermediate disks and irregulars. Applying the purposed model with FBG surveys produces the various plots in figure 3.13[BU][BZ].
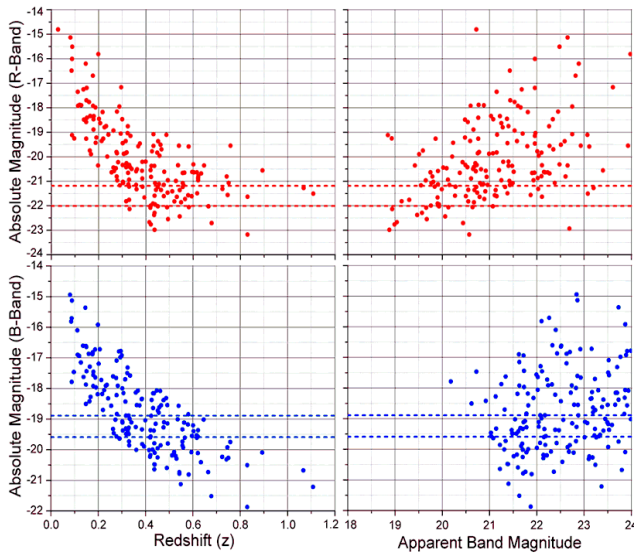
Figure 3.13. Applying a $B - V$ filter to local surveys results in disk and irregular galaxies on average having m_B ranging from -18.89 to -19.59; m_R in comparison ranges from -21.19 to -22.01. After combining several faint blue galaxy surveys, it is observed that many of the FBGs between $0.3z$ and $0.7z$ are either normal disks or irregulars.

Due to the various attempts at explaining the abundance of field galaxies, each will be discussed in detail. The local FBG abundance is completely compatible with no evolution with respect to their redshift distribution[CA]. Many have purposed that either drastic mergers or evolution of the luminosity function must take place. However, number counts in the K, R and B bands rule out evolution in the faint end of the luminosity function[CA]. Additional studies have also concluded that any evolution at the bright end of the luminosity function must be minimal below $0.5z$[BY]. Therefore, the observed $2x$ abundance placed around $0.5z$ ($22.5\ M_B$) cannot be explained by evolution of the luminosity function. Furthermore, recent constraints on merger fractions limit the total amount of major mergers in these regions to $< 30\%$ by $0.5z$. This would in return only reduce the $2x$ abundance to $1.7x$. The FBG anomaly is known as a grand cosmological problem because there is no self-consistent way to explain the abundance with respect to ΛCDM[BT]. The local abundance of FBGs is crucial for ruling out an expanding model since the various aspects are well constrained. When the observed evolution of local blue galaxies is applied to the continuous model however, the $2x$ abundance is in perfect agreement with predictions.
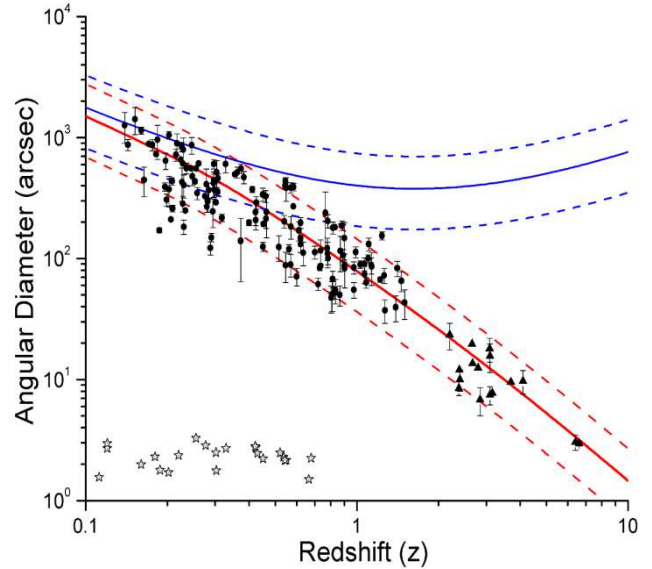
The FBG problem at moderate redshift becomes problematic as they display properties of normal sized disk and irregular galaxies. However, ΛCDM predicts that they are $2 - 5x$ smaller than similar local populations. This has lead to distant FBGs being improperly inferred to as dwarf galaxies. The luminosity function however does not drastically evolve, so this cannot be true. Taking the average of absolute magnitudes from $0.3z$ to $1.0z$ results in $< m_B > = -19.51$ and $< m_R > = -20.96$. This further supports distant FBGs being common late-type galaxies. From high-resolution imaging of FBGs, there is no evidence for an abundance of dwarfs undergoing intense star formation[BX]. Observations clearly rule out the purposed solutions to the ΛCDM faint blue galaxy problem.

Several surveys allow the size of FBGs to be compared to their absolute B-band magnitudes. The available data is limited, with the majority lacking reliable redshift. Edge detection with difference of gaussians was instead applied to high resolution FBGs[BX]. This provides major-axis diameters with respect to absolute B-band magnitude as depicted in figure 3.14. Absolute magnitude is related to metric distance derived from spectroscopically confirmed redshift. As previously stated, the distant FBGs are not dwarfs. Bolometric limitations force galaxies with faint absolute magnitudes to be closer, while the remaining are more distant. This is observed in figure 3.14, where disagreement between models increases as m_B decreases. Half of the FBGs are observed to have mild to moderate star formation, usually across the entire disk. The rest range from common young to late-type disk, some of which are very blue or bulge dominated[BX]. ΛCDM is below even the most extreme cases from the local space. Combined with the lack of luminosity evolution, an expanding universe is ruled out due to incorrect predictions of large-scale curvature. Observations instead insist that the universe is asymptotically flat.

Further insight can be obtained from the most massive objects visible at various redshift ($< 7z$). Locally these are hot x-ray emitting clusters, while the more distant populations consist of reionized hydrogen known as lyman-alpha blobs[CC][CD]. As predicted by the continuous model, distant clusters are older with respect to local clusters. The angular diameter of 148 clusters was further measured to demonstrate that the curvature of an asymptotically flat universe agrees with observations. The diameter of each is measured with respect to x-ray emissions up to 3σ above background rates. For more distant clusters, the extent of lyman-alpha emission was instead applied. Figure 3.15 provides a plot of these clusters and expected size assuming no evolution. The majority of objects were observed by Chandra ACIS-I[CE] and the XMM cluster survey[CF]. Since the angular scale was previously verified with FBG luminosity out to $0.7z$ in figure 3.14, there must be minimal change in cluster size up to this redshift. Mergers in figure 3.15 are depicted by large errors, where uncertainty provides the minor to major axis diameters. A major merger will peak at 30% above initial angular diameter, with an error around 25%.

Figure 3.14. Black stars depict several local starburst galaxies, with the remaining circles being normal spiral, dwarf and irregulars. Red are the high resolution FBGs with respect to the continuous model, while blue is with respect to ΛCDM. The dashed trend line is relative to local galaxies with the standard logarithmic fit[CB]: $m_B = -5.5 \cdot \text{LOG}(A) - 11.9$

Figure 3.15. 148 massive clusters with diameters determined by averaging the minor and major axis of each. Red is relative to the continuous model with a cluster size of $3.25^{+2.75}_{-1.75}\ Mpc$ and blue is with respect to ΛCDM. Circles depict x-ray emitting clusters, while triangles have lyman-alpha emission. Stars at the bottom represent the FBGs from figure 3.14.

The FBG problem becomes more apparent when observed merger fractions are examined. Several recent studies focus on calculating merger fractions by surveying distant galaxies. For moderate redshift ($< 1.2z$), galaxies with low to intermediate mass are inferred to have merger fractions of 5 – 10%[CG]. From a survey of massive galaxies, the merger fraction ranges from 0.03 to 0.14[CH]. Another finds a morphological merger fraction less than 6% for massive disk galaxies prior to $1z$[CI]. An in-depth survey focusing on both active and prior mergers allows uncertainty in merger duration to be ignored. It is observed that major mergers such as those between two medium-sized disks occur once on average by $1.4z$[CJ]. Minor mergers between satellite galaxies and their host are about three times as abundant. However, these do not explain the excess of intermediate sized FBGs. In other words, the FBGs are not satellite galaxies. Distant FBGs are fully consistent with common late-type galaxies, with local populations being dwarfs similar to NGC 4214 or NGC 1310. Without drastic merger rates, there are no remaining explanations with respect to an expanding model. The purposed model however predicts for the excess to exist due to the curvature of the universe.

Merger fractions beyond $1z$ increase in response to the time-scales involved, i.e. these objects are at least $45\ Gyr$ older than the local group. Red and ultra-red galaxies are found at moderate redshift. The Hubble Ultra Deep Field (HUDF) shows many of these galaxies undergoing mergers, resulting in deformed galaxies with tails or multiple cores[AW]. Products of major mergers are not consistent with local ellipticals, explaining why these red galaxies are fitted with extended star formation histories and abundant dust[CK]. From the HUDF, a peak merger fraction of 30% occurs around $2z$ with massive galaxies[CL]. High merger fractions of 40% to 50% are observed beyond $2.5z$, where the objects are consistent with Lyman-break galaxies[CM].

Comparing proper time between $0z$ and $1z$, the continuous model has an additional $38.3 \pm 6.6\ Gyr$. Current studies based upon ΛCDM should therefore have observed merger times $4.1 - 5.8x$ quicker than expected from simulations. These simulations rely on fundamental physics, making it difficult to explain how the process would be occurring at five times the expected rate. Many also underestimate merger times due to the inclusion of dark matter. There is however no proof or direct evidence for dark matter, at least not in any exotic forms. Direct attempts at locally detecting dark matter have also failed[CN][CO]. Instead, dark matter is the result of systematic lensing errors and improper foundations. Without dark matter, the expected mass of galaxies and clusters will decrease. Therefore, merger times from prior simulations are likely underestimated.

From one study, the first pass on average occurs at $0.72\ Gyr$ for Sbc galaxies. Max separation occurs on average by $1.20\ Gyr$, while galaxies merge at $< 1.88\ Gyr >$. After $< 2.88\ Gyr >$ have passed the galaxy is considered to be a merger remnant[CP]. With the merger fractions applied on the next page, the one merger per galaxy by $1.4z$ fits with an average merger time of $4.0\ Gyr$. Both values can be compared to inferred merger times with respect to ΛCDM. Several estimates for $< \tau_{obs} >$ range from $0.2\ Gyr$ to $1.0\ Gyr$[CQ], which is in disagreement by $2.9x$ to $17.5x$ with simulations. A more precise ratio can be obtained from table 3.2. Taking the average of several surveys results in an average merger time of $0.65\ Gyr$, which results in a $4.4x$ to $5.4x$ disagreement with numerical models.

Table 3.2. Merger times of close galaxy pairs

Reference[CQ]	$< z >$	$< \tau_{obs} >_{S08}$	$< \tau_{obs} >_{C06}$
Patton & Atfield	0.05	0.36	0.37
Lin et al.	0.79	0.63	0.63
de Ravel et al.	0.72	1.61	1.50
Kartaltepe et al.	0.70	0.33	0.35
Bundy et al.	0.83	0.32	0.35
Average	**0.62**	**0.65**	**0.64**

Several sets of merger fractions are available from recent literature. Some of these could however be overestimated for several reasons. For example, mature disk or irregular galaxies can demonstrate several areas of intense star formation, which may be improperly interpreted as remnant cores from a previous merger[CR]. The application of maximum likelihood techniques also tends to overestimate merger fractions[CI]. A rough estimate is obtained by assuming one major merger per galaxy at $1.4z$. Since merger times relative to ΛCDM are under-estimated, the averaged value from simulations is applied ($2.88\ Gyr$). Time dependence is with respect to the purposed model as discussed in section (**3.3**). The fractional merger rate is defined by equation (**210**), depicting the fraction of galaxies completing a major merger per proper merger time.

$$R_\tau = \frac{f_m}{<\tau_m>} \tag{210}$$

For a given redshift, the change in total galaxies is related to the fractional merger rate and number density by equation (**211**).

$$\frac{dN}{d\tau} = -R_\tau N \tag{211}$$

Solving equation (**211**) for number density results in exponential decay (**212**).

$$N(\tau) = N_0 e^{-R_\tau \tau} \tag{212}$$

Assuming the merger rate is constant relative to proper time, R_τ is determined with respect to one major merger per galaxy by $1.4z$; this results in $R_\tau = 0.012 \pm 0.002\ Gyr^{-1}$. The $2.88\ Gyr$ merger time translates to a constant merger fraction of 0.035 relative to the continuous model. If the $4.00\ Gyr$ value is applied, the constant merger rate varies to 0.048. However, redshift and time are not directly proportional. For example, about 64% of proper time prior to $1.4z$ occurs before $0.7z$. The merger fraction with respect to redshift would therefore be approximately < 0.035 prior to $0.7z$ and greater than beyond.

With proper time as derived from the continuous model, local merger fractions are easily constrained below 0.04. For example, the fractional merger rate (R_τ) derived from a constant merger rate provides merger fractions (f_m) ranging from 0.030 to 0.040. Distant close pair merger fractions however range from 0.066 to beyond 0.10 throughout the various surveys. Local close pair surveys provide merger fractions between 0.005 and 0.02. Therefore, the approximation of $R_\tau = 0.0120$ is overestimated for redshift below $0.7z$. Even after applying this value with respect to ΛCDM, the 2x abundance of FBGs at $0.5z$ only decreases by 28.6%. If the number density at $0.5z$ is 200 galaxies per metric volume, the final amount of galaxies would decrease to 143 by $0.0z$. ΛCDM or an expanding model is therefore off by 43% when overestimating major mergers prior to $0.5z$.

Merger fractions above 0.04 for the local space are clearly too high. The survey that is found to be the most consistent focuses on galaxy pairs with $M_V < -19.8$[CQ]; this limit coincides with common Sb/Sc disk galaxies. The projected radius for these close pairs ranges from 5 to $20\ kpc$ (Kartaltepe et al. 2007). With respect to the average merger time obtained from simulations[CP], the ensemble of Sbc mergers has the majority of runs starting at $11\ kpc$. A few runs have much greater initial radius ranging from 44 to $50\ kpc$. Some of the merger times in table 3.2 also apply such large distances (de Ravel et al. 2009), indicating that the ratio of expected versus observed merger time is consistent with prior parameters. Extrapolating data from Kartaltepe et al. (2007) provides table 3.3. These fractions are applied with proper time to determine the redshift dependence of major mergers.
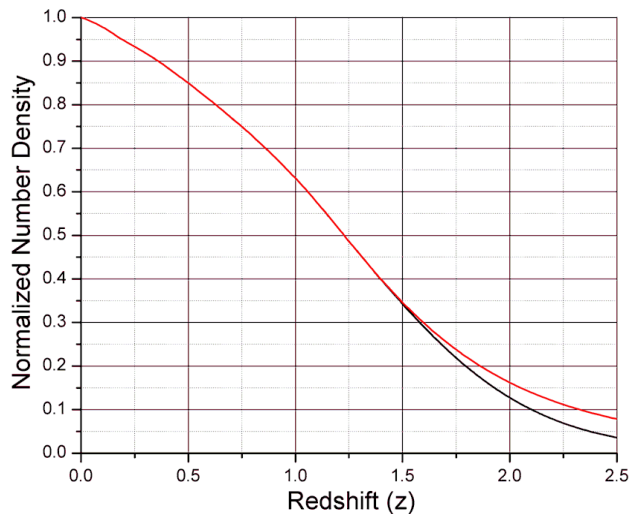
Table 3.3. Merger fractions with respect to redshift

| Redshift	f_m	Redshift	f_m
0.15z	0.012	0.75z	0.045
0.25z	0.018	0.85z	0.054
0.35z	0.025	1.00z	0.073
0.45z	0.030	1.15z	0.102
0.55z	0.034	1.30z	0.129
0.65z	0.039	-	-

Relative to the local space, merger fractions as determined from morphology require that 3% of local galaxies are merger remnants[CS]. Averaging several local pair studies places the merger fraction at 0.018, while Kartaltepe et al. (2007) provide 0.007. Relative to the purposed model, one merger on average at $1.4z$ should also include mergers that have already occurred prior to the local space. This requires that $3\% \pm 1.8\%$ of the local population has already undergone mergers, which is insignificant. To include merger fractions beyond $1z$, the data was extrapolated with an average between several surveys. These vary between 0.19 and 0.22 at $2.5z$, with a maximum fraction for any reference being 0.30 at $2.0z$. Applying these additional constraints with respect to the continuous model provides the relative amount of galaxies for a particular redshift in figure 3.16. The one major merger per galaxy occurs at a redshift of $1.2z$ instead of the previously referenced $1.4z$. The $4.4 - 5.4x$ disagreement with expected merger times makes it difficult to plot the amount of galaxies with respect to ΛCDM. The normalized distribution of proper time between models however is nearly proportional at low z. The $3x$ abundance around $0.8 - 1.0z$ would therefore decrease by 32%, i.e. ΛCDM is off by $104\% \pm 25\%$ in effective number density. The $2x$ abundance at $0.5z$ indicates an error of $70\% \pm 15\%$.

The ratio of scale-factors can be applied to the normalized number density in order to determine the expected abundance of FBG, depicted in figure 3.17. The $2x$ abundance at $0.5z$ is in agreement with prior constraints including lack of drastic merger fractions and minimal luminosity evolution. The abundance peaks beyond the observed $2 - 3x$ disagreement relative to $M_B = [22.5, 24]$. Apparent magnitudes of FBGs versus redshift were further predicted from the absolute B-band distribution of local blue galaxies. With the continuous model and observed mergers, $22.5\ M_B$ and $24.0\ M_B$ correspond on average to $0.54z$ and $1.01z$ respectively.

Although observations such as baryonic matter cooling with increasing redshift can be blamed on various hypothesis, there is no answer for the $2x$ to $3x$ abundance of FBGs. Combined with luminosity characteristics, they should be nearly the same size as local late-types. However, the sizes inferred from ΛCDM are $2 - 5x$ smaller than would be expected. The nearly equal disagreement between both of these aspects must be due to improper curvature of the universe. Occam's razor alone would support this conclusion; however, all viable explanations have also been ruled out.

Figure 3.16. Number density of galaxies with mergers only.
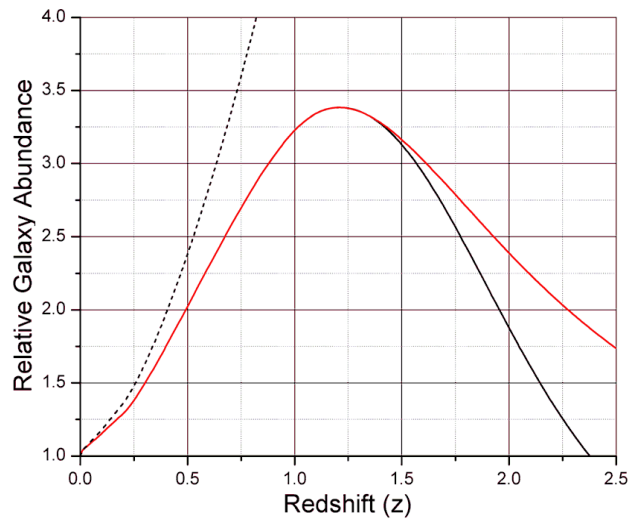
Figure 3.17. The expected abundance of galaxies with respect to no evolution ΛCDM is represented with a dashed line. Red corresponds to the continuous model with the merger fractions provided in table 3.3 and $< \tau > = 2.88\ Gyr$. Black is maximum merger fractions extrapolated beyond $1.3z$[CM].

3.6. Metallicity

Nuclear entropy is also useful for differentiating between the purposed model and ΛCDM. There are several properties of galaxies that can determine the redshift dependent evolution of metallicity. The focus therefore changes from that of large-scale curvature back to time dependence versus redshift. ΛCDM or an expanding model requires galactic age to decrease with distance, while the continuous model predicts the opposite. Time-scales involved were also found to agree with the purposed model after comparing simulations to observed merger times. FeII:MgII ratios and variations in magnesium within galaxies further provide strong evidence for the continuous model. Since the models provide opposite predictions for time dependence, evidence for the purposed model is evidence against ΛCDM.

The evolution of metallicity can be inferred from galactic morphology, which trends from early-type in the local space to late-type for the more distant galaxies. Early-type galaxies consist of ellipticals and lenticulars, usually in clusters containing large amounts of hot, x-ray emitting intercluster medium (ICM). Clusters such as Abell 1367 demonstrate how galaxies contained within regions of hot ICM lack active star formation, i.e. they are considered to be passive[CT]. The majority of galaxies on the perimeter of the ICM region are either active or starburst. Similar clusters such as Abell 1656 are common in the local space, containing primarily early-type galaxies and a few late-type populations. The observed epoch of intense star formation is from $0.5z$ to $3z$, in agreement with x-ray emitting gas inhibiting stellar formation. The ISM is also about $3.8x$ cooler by $1.2z$ relative to local galaxies. It was previously discussed how lyman-alpha blobs have dimensions similar to local x-ray emitting clusters. An expanding model however provides the wrong dimensions of these objects by several orders of magnitude. The lyman-alpha blobs are instead massive clusters that have cooled over $\geq 50\ Gyr$. All of these observations agree with the continuous model and purposed revisions to galactic evolution.

Local merger fractions are too insignificant to play a role in the thermal or nuclear entropy of galaxies prior to $1.0z$. Even with a major merger, the nuclear entropy of a galaxy cannot drastically vary. Early-type galaxies for example contain an abundance of population II stars, which are metal poor. Middle-aged spiral galaxies on the other hand contain a mixture of population II and I stars. These galaxies are not metal poor, containing dust and much less x-ray emitting gas. A collision between two disk galaxies may increase the temperature of ISM; however, it will not reverse nuclear entropy or eliminate prior population I stars. There is also no clear transition from disk to elliptical galaxies in surveys. NGC 6240 is a good example of a major merger between two disks. It is similar to the major mergers occurring with red and ultra-red galaxies in the HUDF. These red populations have abundant dust, which is not similar to the x-ray emitting gas in local elliptical galaxies. They instead have very luminous cores with tails or peculiar shapes. Time-dependence of galactic entropy clearly disagrees with ΛCDM when considering observations.

From moderate to distant redshift ($2 - 4z$), the purposed model predicts $60 - 110\ Gyr$ of evolution from the local space. Therefore, dense regions of intense star formation should begin to deplete primordial hydrogen and helium. This however does not imply that regions without star formation will become metal rich, i.e. distant galaxies or clusters are usually embedded within regions of reionized hydrogen. Galactic star formation will also depict the evolution of ISM. Type II supernova events are associated with metal poor stars, where the final Fe:Mg ratio is about $1.65x$. Type Ia events are more metallic, producing Fe:Mg ratios far above type II events ($393x$). The size and degeneracy of stars also play roles in the type of supernova. For example, type Ia events are inferred to occur from massive stars and are much more energetic than other types. The location of SNIa are also consistent with the continuous model, which uses them to track the flow towards central core.

The iron and magnesium concentrations in ISM play a crucial role in determining the relative age of distant galaxies. Nuclear entropy naturally favors the production of iron over long time-scales, with magnesium slightly lower with respect to nuclear potential. Both are created from nuclear fusion and should be subjected to similar environments. For example, any mechanism besides nuclear fusion that varies FeII will proportionally vary MgII. Since rotational curves are observed to be unstable, it is unlikely that supermassive black holes at the center of galaxies will substantially vary the surrounding metallicity. Therefore, distant galaxies are expected to have increased metallicity and higher FeII:MgII ratios relative to similar local populations.

Prior to discussing FeII:MgII ratios, evidence of increasing metallicity can be inferred through other methods. The absorption of distant sources by local galaxies demonstrates an abundance of MgII. These galaxies are observed from the local space up to about $0.9z$[CU]. Weak MgII absorbers are further observed in abundance from 0.7 to $2.2z$, while vanishing beyond $2.7z$[CV]. With observed merger fractions and continuous model, the relative amount of weak MgII absorbers is depicted in figure 3.18.
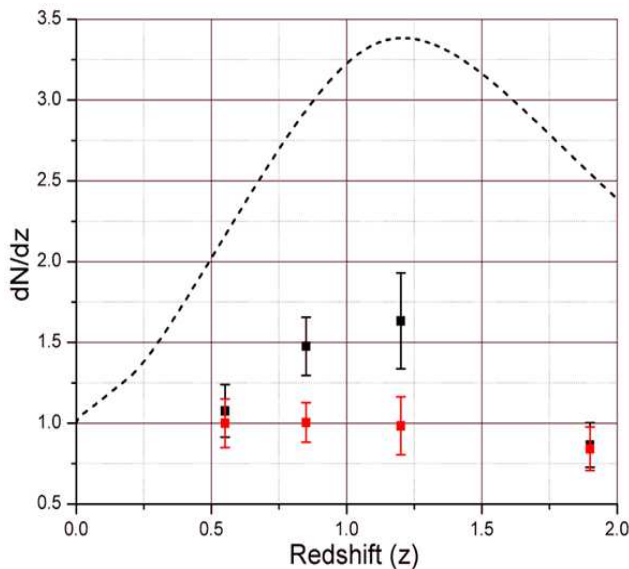
Figure 3.18. The dashed line represents the inferred abundance with mergers from section (**3.5**). Black indicates the averaged dN/dz from ΛCDM surveys and the continuous model with evolution is in red. dN/dz in this case refers to the number density multiplied by the proper geometric cross section[CV].

The spectrum of quasars also provides valuable information relevant to metallicity. Quasars are some of the most luminous and distant objects in the observable universe. Similar to SNIa, quasars display characteristics of highly degenerate matter. These however are related to active galactic nuclei, which harbor supermassive black holes. Relative to the continuous model, highly degenerate objects are older and therefore in the flow towards central core. Several studies were combined in figure 3.19 to determine the evolution of FeII:MgII with respect to redshift[CW][CX][CY][CZ]. The high ratios observed at $6z$ are indicative of galaxies that have already undergone intense star formation[CZ]. For the ISM to be enriched with an abundance of these elements, several generations of stars must have undergone supernovas. Relative to ΛCDM, the proper age of the universe is less than $1\ Gyr$ at $6z$. Considering that the region of intense star formation is observed from $0.5z$ to $3z$, ΛCDM does not fit observations. Other observations such as increasing cold baryonic matter with redshift, number densities, galactic evolution and the dark flow agree with galactic age increasing with redshift. An expanding universe on the other hand would violate several fundamental laws of physics including the second law of thermo-dynamics and nuclear entropy.
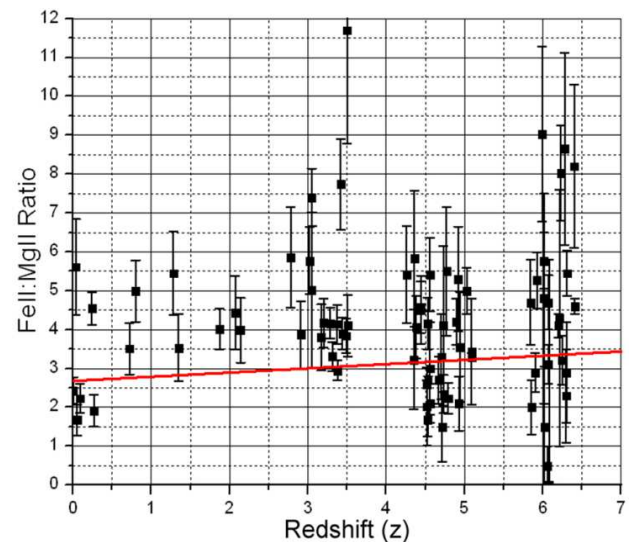

Figure 3.19. High FeII:MgII ratios at extreme redshift are indicative of older galaxies. A statistically significant trend is also observed with a slope of 0.108 ± 0.03.

3.7. Statistical Analysis

Although an expanding universe is conclusively ruled out from incorrect predictions of large-scale curvature, it is possible to compare redshift versus distance modulus between ΛCDM and the purposed model. Distinction between models at low redshift arises in the form of dispersion due to directional dependence. This is predicted by the continuous model from varying y_0 over its complete range (0 Gpc to > 0.54 Gpc). Relative to section (**3.2**), the slope of the universe and average y-intercept are determined from type Ia supernova (SNIa) and gamma ray burst (GRB). SNIa are superior for determining cosmological distances due to their nearly uniform properties. GRB are less reliable, but can still be used to constrain redshift versus luminosity distance. SNIa and GRBs both display characteristics of highly degenerate matter, which is an indication of relatively older galaxies. These events will therefore be statistically more abundant along the flow towards central core, where the continuous model predicts for objects to be older than the local group.

With respect to Occam's razor, the purposed model fits the shape of the universe with a single constant (S_0). ΛCDM usually needs two constants in the form of dark energy and matter. Dark energy however cannot be directly detected and has no connection to the standard model. It is inferred to exist solely because it allows an expanding model to match observations. Although these non-classical modifications fit redshift versus distance modulus, they fail to agree with the observed shape of the universe. Occam's razor is therefore a necessity for arriving at the proper theory, as anyone can force a model to agree with observations by introducing purely mathematical constructs. Failure to reach parsimony and over-reliance on confirmation rather than refutation are dangerous practices for this reason. From these aspects alone, the models cannot be put on equal footing. The continuous model contains the least amount of free variables and non-classical assumptions.

ΛCDM and the continuous model have similar redshift versus distance modulus predictions from 0.5z to about 10z. Disagreement between models in this region peaks at 0.25μ around 2.5z, making it difficult to differentiate between the two. ΛCDM is constrained by an interpretation of the CMBR and baryon acoustic oscillation data[BN]. These provide $H_0 = 70.4^{+1.3}_{-1.4}$, $\Omega_b = 0.0456 \pm 0.0035$, $\Omega_c = 0.222 \pm 0.026$ and $\Omega_\Lambda = 0.728^{+0.015}_{-0.016}$. Figure 3.20 depicts an ensemble within these limits for $\Omega_m = \Omega_b + \Omega_c$ and $\Omega_\Lambda = 1 - \Omega_m$. The purposed model applies the best fitting slope and y-intercept, including uncertainties previously provided in section (**3.2**). Since SNIa are considered standard candles, observations from 0.1z to 0.5z can easily rule out an expanding universe. The disagreement for local redshift once again arises from directional dependence due to an asymptotically flat universe. The majority of events beyond 1.0z consist of GRB, which suffer from circularity problems. In other words, most methods require that a prior cosmological model be selected in order to determine the luminosity distance to GRB sources. Attempts to avoid this problem apply various relations between GRB parameters and extrapolating SNIa data. However, some of these methods are also found to be model dependent and should not be used to independently determine cosmological distances.
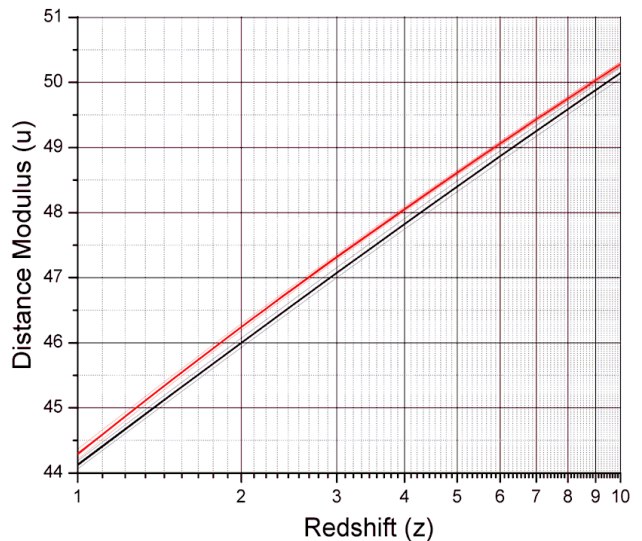

Figure 3.20. Red is the continuous model within limits of error, while black is ΛCDM within limits of error.

A more detailed comparison between models can be achieved from the distance modulus residual with respect to the continuous model. However, it is determined that the dataset obtained from NED redshift independent calculations was contaminated with respect to a few GRBs. The problem arises due to the lack of standardization for GRB sources and inclusion of fiducial data; this is apparent in figure 3.21 from $2.0z$ to $5.0z$. Prior to $1.0z$, uncertainty is too small to be fit with homogeneous expansion. For example, a portion of data is outside of either models best fit by more than $\pm 0.50\mu$. However, the trends for the continuous model in figure 3.21 only include uncertainty in slope and average distance to the start of flow towards central core. Considering the shortest path instead begins at $0.0\ Gpc$ and others at distances greater than y_0, the continuous model explains this dispersion relatively well. The purposed model is also centered on the bulk of available SNIa data prior to $1z$ indicating a superior fit. To the contrary, homogeneous expansion does not fit observations from $0.1z$ to $0.5z$. Extrapolating SNIa data under the assumption of ΛCDM will therefore produce incorrect predictions for GRBs beyond available SNIa data.
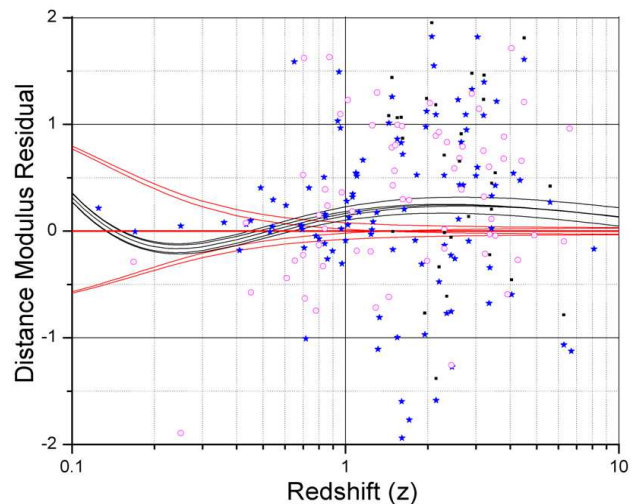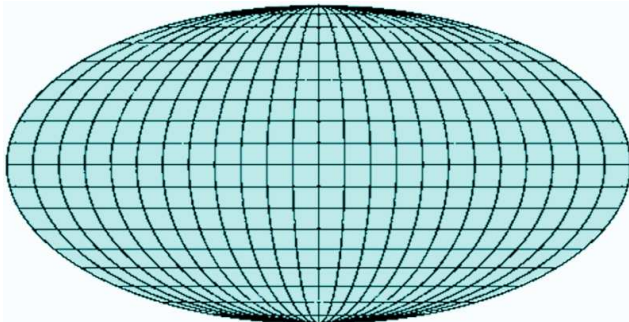
Although the dataset applied from the NED database is claimed to be redshift independent, some of the data is fiducial; i.e. metric distance is determined assuming the big bang model is correct. For example, there are several data points in figure 3.21 that are anomalously clustered around the ΛCDM trend from $2.0 - 5.0z$. To demonstrate this, the residual is plotted in figure 3.22 with respect to several studies. As would be expected from an average error of $\pm 1.11\mu$ beyond $2.0z$, the anomaly no longer exists. After applying solely SNIa events for all available redshift, the slope $(3.216 \cdot 10^{42})$ and average y-intercept $(0.313\ Gpc)$ are still within previous limits. Several contaminated data points are related to improper methods. GRB 051109A for example contains 3 of 8 values from 2009MNRAS. Removing these from the average increases distance modulus to 46.426μ, with the continuous model predicting 46.429μ. Issues with these references also include the circularity problem and use of the Amati relation. The Amati relation is found to suffer from selection effects and should not be used to probe distance[DD]. This is applied in 2010JCAP, although the data is in better agreement with SNIa. 2009MNRAS extrapolates only 55% of SNIa data with fiducial methods. This systematically offsets the 2009MNRAS GRBs with respect to the more accurate SNIa dataset between redshift of $0.015z$ and $1.55z$.

Table 3.4. Average SNIa/GRB error versus redshift

Redshift	Avg. Error	Redshift	Avg. Error
$0.1 - 0.5z$	$\pm 0.21\mu$	$1.0 - 2.0z$	$\pm 0.69\mu$
$0.5 - 1.0z$	$\pm 0.27\mu$	$\geq 2.0z$	$\pm 1.11\mu$
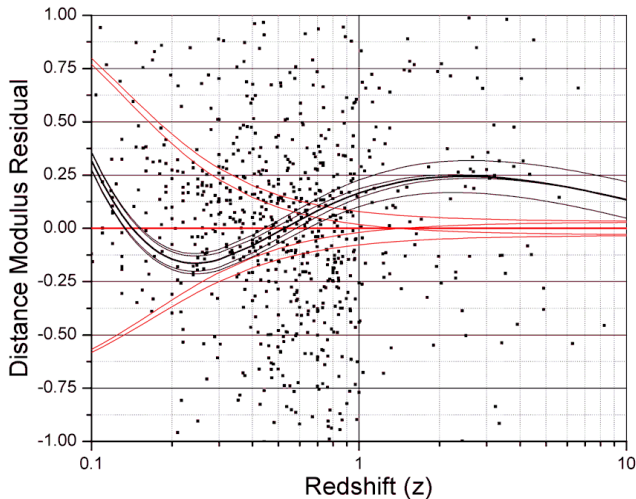
Figure 3.21. A plot of the combined SNIa/GRB dataset used to determine the slope of the universe and average y-intercept.

Figure 3.22. Several sets of gamma ray burst are plotted from ★ 2010JCAP[DA], ◯ 2009MNRAS[DB] and ■ 2009EPJC[DC].

3.8. The Cosmic Background Radiation

The big bang theory claims that the CMBR is due to a period of recombination after the initial creation of space-time. At this point, the universe cooled until space became transparent to free photons. The big bang theory also claims that the observed blackbody radiation in all directions of space is not a free electromagnetic field, but instead localized packets of electromagnetic energy. To understand why this is not true, the source of blackbodies must be understood. All finite objects with a temperature will emit a spectrum of radiation that peaks at a given wavelength. When an object emits this blackbody spectrum, it is due to the internal kinematic energy or temperature. The free field emitted from massive objects therefore obeys a statistical distribution of internal energy, which is released at the surface boundary. Converting the observed CMBR temperature as depicted by figure 3.23 into the relative value at emission, the core's surface temperature is $3000\,K$. In comparison, the Sun's surface has a temperature of about $5778\,K$, indicating that the core likely consists of dense quark matter. Relative to an Einstein black hole with event horizon, the surface will theoretically emit black body radiation in the form of Hawking radiation. The temperature is inversely proportional to mass with a coefficient of $6.1686 \cdot 10^{-8}\,M_\odot \cdot K$. A $3000\,K$ central core with respect to an Einstein black hole would have a mass of $2.056 \cdot 10^{-11}\,M_\odot$, compared to $3.694 \cdot 10^{-8}\,M_\odot$ for the Moon.
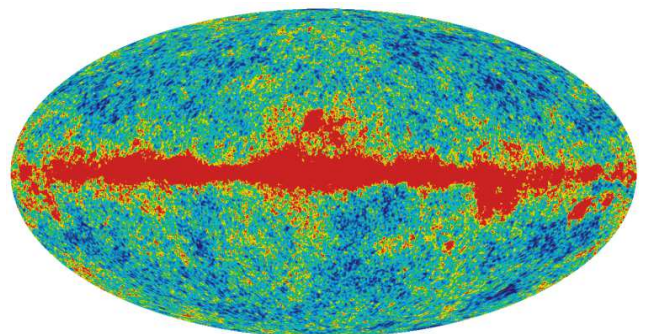
The CMBR shows peculiarities such as a dipole moment, large-scale bulk flows and additional fluctuations from interaction with external matter. The CMBR temperature prior to subtracting the average value is $2.72548 \pm 0.00057\,K$[BC]. Figure 3.24 depicts the dipole moment observed after subtracting the average temperature; figure 3.25 is the CMBR with the dipole subtracted. The dipole moment is due to Earth's motion relative to the CMBR source or the core's surface. Since a spherical body will emit blackbody radiation at a nearly constant z or radius, only the Doppler Effect applies. Relative to the source of the CMBR, the solar system is moving at $369.0 \pm 2.5\,km \cdot s^{-1}$ towards $(l,\ b) = (264.26° \pm 0.33°, 48.22° \pm 0.13°)$[AZ]. Taking into account the local group's motion, this velocity becomes $627 \pm 22\,km \cdot s^{-1}$ towards the direction $(l, b) = (276° \pm 3°, 30° \pm 3°)$[AZ].
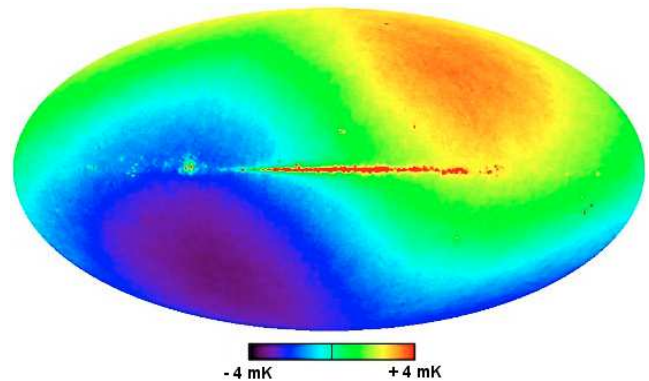

Figure 3.24. After subtracting the average temperature from the sample measured by COBE, the dipole dominates. **Image credited to NASA/WMAP Science Team**[BD]

Figure 3.23. The locally observed cosmic background radiation with a temperature of approximately $2.725K$ after redshift.

Figure 3.25. After subtracting the dipole moment from figure 3.24, the remaining fluctuations in the CMBR occur externally from the core. Image is provided from WMAP (2003). **Image credited to NASA/WMAP Science Team**[BD]
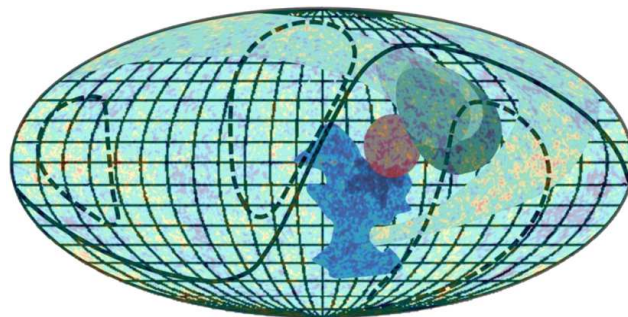
Remaining fluctuations in the CMBR are from the Milky Way and scattering of electromagnetic by matter external to the core's surface. Figure 3.26 is the CMBR after removing local foreground sources; it depicts two hot stripes and a central cold patch. The source of the CMBR itself should be at a nearly constant temperature of 3000K. Variations within the cleaned CMBR image instead occur between the foreground and background due to scattering from the x-ray emitting gas of massive clusters. The relativistic charged particles boost the black body spectrum to higher energy levels. This increases the observed black body temperature from deep blue to green and red. Analysis of x-ray emitting clusters has also shown a statistically significant bulk flow extending from the local group to ~$0.77\ Gpc$[AZ]. The velocity is estimated to be [600, 1000] $km\ s^{-1}$ from the thermal S-Z effect[AZ]; however, free field radiation undergoes Thomson scattering. Although many of the directions in local space lead back to the central core, there must logically be a flow of younger galaxies and clusters into Earth's present region. This is necessary to remain consistent with the foundations used in deriving non-local redshift, i.e. the universe is in a stead state. With the medium of galaxies and clusters progressing from hot x-ray emitting gas into cold metallic dust, the dark flow should consist of relatively younger clusters.
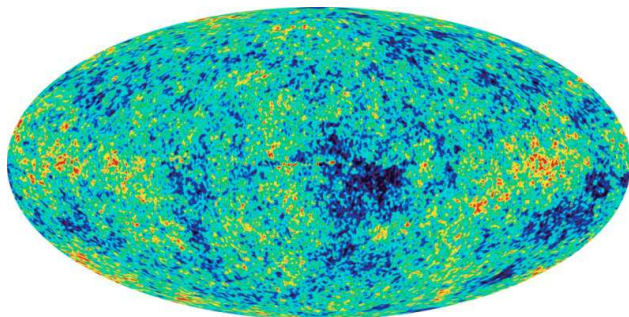
Conventional theory attributes the CMBR to an epoch of recombination, where photon decoupling takes place. This explanation is only valid for an expanding universe, which has a specific shape and angular scale. Section (**3.5**) however proved that both galaxy number densities and angular scales are incompatible with an expanding universe. This is easily observed from $0.3z$ to $0.7z$, becoming more drastic beyond. Since an expanding model can be conclusively ruled out, current foundations for the CMBR are invalid. It was further demonstrated in sections (**3.5, 3.6**) that the purposed model fits the correct shape of the universe with respect to number densities, angular size and several other aspects.

The purposed or continuous model requires two polar jets originating from a central core in order to explain current observations of entropy. If the core acts as a mechanism for baryon asymmetry, an annihilation boundary should also be observed between hemispheres. The inferred local jet is depicted in figure 3.27. Anomalies may distort the cleaned image, possibly beyond use in some regions. The elliptic plane for example runs through the far right side of the local jet, which on average becomes cooler than the surrounding areas. It also correlates with zodiacal dust and several features such as quadrupole/octupole alignment and the cold strips or "fingers" in the southern hemisphere[BI].

Figure 3.26. The cleaned CMBR is observed to contain a large hot strip originating from a central cold patch. An annihilation boundary or hot ring is surrounding the central cold patch. The base of the local jet should be visible, with the hot strip to the right being a continuation of the dark flow at extreme redshift. **Image credited to NASA/WMAP Science Team**[BD]

Figure 3.27. The dark flow is depicted in shades of gray, where lighter shades are more distant[BK]. Since SNIa are used to measure the flow towards central core, an observed SNIa bulk flow is in red[BL]. Hemispherical power asymmetry[BJ] could be due to the local jet, where temperature and resolution variations are more extreme closer to the central region.

3.9. Baryon Asymmetry

Section (**3.5**) demonstrated that an expanding universe is incompatible with observations. The previous sections also provide sufficient evidence for an asymptotically flat universe with central core. It is therefore important to discuss the consequences of having an always existent, steady state universe in terms of entropy and stability. The concept of an absolute beginning of reference time is flawed. Reference time in this perspective is relative to a space-time with no vacuum energy. For example, it is known that metric distance becomes infinite as an event horizon is approached with respect to the preferred reference frame. Therefore, nothing can reach the surface boundary within a finite amount of reference time. Relative to proper time, an observer falling into an event horizon would do so in a finite amount. This is an illusion since the observer will cease to evolve as the surface is approached. In comparison to a photon, the problem can still be defined in terms of metric distance. Since the photon will be travelling along a null geodesic, it must travel an infinite amount of metric distance prior to reaching the surface.

It is possible to take the limit of the inferred state of an expanding universe as $t \to -\infty$. With either Einstein's field equations or vacuum field theory, matter will converge at a single region in space until it is infinitesimally close to forming an event horizon. With respect to the preferred reference frame, a discontinuity forms. For any event horizon, time is undefined due to infinite vacuum energy density. From the other direction, the collapsing system cannot form into a conical singularity within a finite amount of reference time. This discontinuity between time prior to a big bang scenario and formation of event horizon indicates that an initial singularity could have never existed with respect to the reference frame. On the other hand, one could argue that the universe began at some infinite time ago as an object infinitesimally close to a conical singularity; i.e. the interpretation of accelerated expansion is still viable. If this were true, Hubble's law would remain valid for all redshift rather than just the local. In addition, this perspective requires galaxies to become older as redshift increases, which is contrary to several recent observations. The most important of these is the increase in cold baryonic matter with redshift. Even beyond this, an expanding theory requires several non-classical assumptions such as dark matter and dark energy. It fails to explain observations of galactic evolution, number densities or the size of distant galaxies and clusters. Therefore, ΛCDM or an expanding model should be abandoned.

An always-existent universe has other properties based upon boundary conditions. If at some time prior to the present the universe was unstable and energy could escape, the instability would have existed at some prior point in time. With respect to a quantum system, there will be a distribution of possible events occurring over a finite period. If the system has a finite probability distribution, then it is impossible for any instability to have not occurred prior to a finite time before present. In other words, any instability must have existed for an infinite period and according to probability, any finite distribution requires that the universe is stable at $t \to -\infty$. This also relates to the null existence of event horizon. For example, all observations agree with a central core existing in the present universe. If black holes had event horizon as predicted by EFEs, the universe would clearly not exist in the current state. As matter approaches a central event horizon, some would be captured while the rest is ejected. Over an infinite amount of reference time prior to the present, the central event horizon would capture all matter within the universe. The CMBR temperature further provides direct proof against the existence of event horizon and Hawking radiation.

In order for an always existent universe to be in its present form, the laws of thermodynamics must be missing something. The last piece of the puzzle was previously beyond comprehension due to the belief in an expanding universe and event horizon. Since all massive objects must have finite vacuum fields, the gravitational force aids in completing the thermodynamic cycle. The entire process can be viewed as beginning from the surface of the central core in the form of a dense relativistic jet. From this point to Earth's present position in the universe, the usual thermodynamic principles apply. Dense quark matter for example will decay into x-ray emitting gas. Radiation emitted over this transition follows geodesics back to the central core, ensuring the universe is stable. However, an asymptotically flat universe by definition will have finite vacuum energy density at all points in space. The only requirement is that the universe remains localized for an infinite period, i.e. it exists in a steady state. Beyond Earth's present position, population I stars are abundant due to increased metallicity and cold baryonic matter. The bulk flow continues to move towards entropy as galaxies gain momentum falling into the center of the universe. The missing piece is where matter falls back into the central core and momentum is conserved via two polar jets. The universe therefore exists in an anisotropic state of entropy as depicted by figures 3.5 and 3.7.

The laws of thermodynamics demand that the entropy of a closed system can never be reversed without external energy. From figure 3.5, it is clear that entropy is constant for all time relative to the preferred reference frame. Therefore, the laws of thermodynamics are not violated since the universe acts as a perpetual machine. The actual mechanism that creates relativistic jets is speculated upon with QCD and modern MHD simulations. Compared to the local region of space that Earth currently resides in, the jets emanating from the central core should be extremely large. With respect to the amount of galaxies and clusters falling into the central core, it likely contains the mass of millions or billions of galaxies and clusters. The center of the core should therefore exist in a dense, color superconducting state. The central region of the core is assumed to consist of top, bottom and charm quarks due to sheer size. With respect to modern theory, compact stars are already predicted to exist in a non-CFL color superconducting state[BF]. The layer directly adjacent to the core's central region will also likely exist in a superfluid state (CSL, Planar, A/Polar). The center could possibly rotate, further inducing a magnetic field from the London moment.

Comparing the bare mass of quarks, the core should have layers depicted by chemical potentials. For example, the up and down quarks exist within the $2 - 15\ Mev$ range. The strange quark has a bare mass between $100 - 300\ Mev$, while the remaining quarks exist from $1000\ Mev$ and beyond. Baryon asymmetry is speculated to originate from the strange quark/anti-quark layer. Considering that the core acts as a perpetual machine, the energy needed to produce the jets must be provided by the inflow alone. Due to the asymmetric shape of the universe, matter enters the equatorial regions and is funneled inwards. As density increases, the quarks at each radius become more massive until a strange diquark layer is reached. This type of condensate should be favored due to the gap between quark masses and single quark flavor. The CSL, planar or A/polar single flavor states also demonstrate superfluidity and the Meissner effect[BE]. As matter approaches the center, the magnetic field energy density begins to surpass kinematic energy density[AM]. At this point, it is expected that the inflow stops moving with the bulk of material, effectively producing a toroidal magnetic field[AM]. Due to lorentz forces, the $< ss >$ condensates are accelerated in one direction with $< \overline{ss} >$ in the opposite.

Putting things into perspective, the structure of the core should be similar to figure 3.28. After applying the methods discussed in section (**3.3**) to derive proper time, matter approaching the surface of the core will be traveling at 99.999988% the speed of light. In consideration of momentum conservation and the internal magnetic field, the rate of inflow alone is capable of explaining the energy behind each jet. The bulk of material ejected should originate from the strange diquark layer due to its insulating property. As the quark matter begins to cool into mesons and baryons, the jet pointing in the direction of $\uparrow N$ will consist of K^0, $K^-, \pi^\pm, \pi^0, p^+, n^0, \Lambda^0, \Sigma^\pm, \Sigma^0, \Xi^-$ and Ξ^0; although not exclusively. These pairings occur naturally since baryons containing a mixture of quarks and anti-quarks have not been observed experimentally. However, the anti-quarks must still be paired with something external to the surface. The resulting mesons decay into photons, electrons and neutrinos; table 3.5 provides the most common decay modes. The amount of material ejected from each shell of the core depicts the ratio of electrons and neutrinos to baryonic matter, although the composition of each layer must also be known.
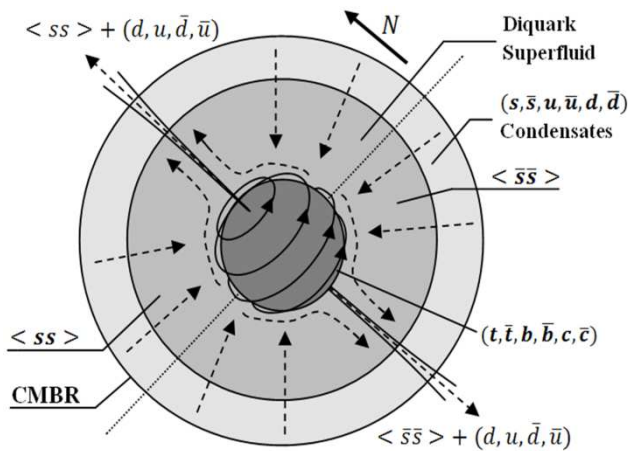
Figure 3.28. A simplified section of a central core that would induce baryon asymmetry. The focus is placed upon the strange diquark layer, which is theorized to exist due to the gap in mass between quarks. In a steady state model, the core must have a constant inflow and outflow. This process creates an abundance of $(p^+,\ e^-)$ in one hemisphere and $(p^-,\ e^+)$ in the other.

The decay of unstable baryons in the northern hemisphere of the universe also results in products that are observed in abundance locally. Table 3.6 provides the common decay modes for the main constituents. This process creates an abundance of protons and electrons $(p^+,\ e^-)$ in the northern hemisphere, with an abundance of anti-matter $(p^-,\ e^+)$ in the other. It is concluded that Earth currently resides in the northern hemisphere beyond the point where the relativistic proton, electron and neutrino gas has cooled. For any steady state model in the current universe, a perpetual machine and explanation for the CMBR are required. With the corrections to general relativity, event horizon are no longer possible. Therefore, an asymptotically flat universe containing a central core would emit a $3000\ K$ black body spectrum as observed. The purposed configuration further explains the hot ring surrounding the central cold spot in the cleaned CMBR image, the mechanics behind a steady state and origin of the dark flow.

Table 3.5. Common decay modes of mesons and fermions[BG].

Particle(s)	Decay Mode(s)	Particle(s)	Decay Mode(s)
$\pi^-\ (\overline{u}d)$	$(\mu^- + \overline{v}_\mu),$ $(e^- + \overline{v}_e)$	$\pi^+\ (u\overline{d})$	$(\mu^+ + v_\mu),$ $(e^+ + v_e)$
$\pi^0 \left(\dfrac{u\overline{u} - d\overline{d}}{\sqrt{2}}\right)$	2γ	$K^0\ (\overline{d}s)$	$\Lambda^0 + \gamma$
$K^-\ (\overline{u}s)$	$(\mu^- + \overline{v}_\mu),$ $(\pi^- + \pi^0),$ $(e^- + \overline{v}_e + v_\mu)$	μ^-	$e^- + \overline{v}_e + v_\mu$
		$e^+ + e^-$	2γ

Table 3.6. Common decay modes of baryons[BG].

Baryon	Decay Mode(s)	Baryon	Decay Mode(s)
$p^+\ (uud)$	Stable	$\Sigma^0\ (uds)$	$\Lambda^0 + \gamma$
$n^0\ (udd)$	$p^+ + e^- + \overline{v}_e$	$\Sigma^-\ (dds)$	$n^0 + \pi^-$
$\Lambda^0\ (uds)$	$(p^+ + \pi^-),$ $(n^0 + \pi^0)$	$\Sigma^+\ (uus)$	$(p^+ + \pi^0),$ $(n^0 + \pi^+)$
$\Xi^0\ (uss)$	$\Lambda^0 + \pi^0$	$\Xi^-\ (dss)$	$\Lambda^0 + \pi^-$

References

[A] Edmund, Whittaker. **"A History of the Theories of Aether and Electricity from the Age of Descrates to the Close of the Nineteenth Century"**. Dublin, Ireland: Hodges, Figgis. 1910

[B] Jackson, John. **"Classical Electrodynamics"**. New York: Wiley, 1999.

[C] Griffiths, David. **"Introduction to Quantum Mechanics"**. Upper Saddle River: Pearson Prentice Hall, 2005.

[D] Born, Max. **"The Statistical Interpretation of Quantum Mechanics"**. Nobel Lecture, December 11, 1954. Link (^)

[E] Dirac, Paul. **"Theory of Electrons and Positrons"**. Nobel Lecture, December 12, 1933. Link (^)

[F] Hestenes, David. **"The Zitterbewegung Interpretation of Quantum Mechanics"**. 1990. Link (^)

[G] Hestenes, David. **"Real Dirac Theory"**. 1996. Link (^)

[H] Pollock, M.D. **"The Dirac Equation in Curved Space-Time"**. March 11, 2010. Link (^)

[I] Gaberdiel, Matthias; Ridder, Aude. **"Quantum Field Theory II"**. July 15, 2011. Link (^)

[J] Ellis, John. **"Standard Model of Particle Physics"**. Link (^)

[**K**] Grünewald, Martin. **"The LEP Electroweak Working Group"**. Link (^)

[**L**] **"End of the Line for LEP"**. November 8, 2000. Link (^)

[M] **"God particle may not exist"**. December 6, 2001. Link **(^)**

[N] **"Higgs hunting at 144GeV"**. July 27, 2011. Link (^)

[O] **"Higgs signal sinks from view"**. August 22, 2011. Link (^)

[P] **"Detectors home in on Higgs boson"**. December 13, 2011. Link (^)

[Q] **"Physicists find new particle, but is it the Higgs?"**. July 3, 2012. Link (^)

[R] Mammadov, Gulmammad. **"Reissner-Nordstrom Metric"**. May 4, 2009. Link (^)

[S] Stoica, Ovidiu-Cristinel. **"Analytic Reissner-Nordstrom Singularity"**. April 19, 2012. Link (^)

[T] Taylor, Joseph. **"Binary Pulsars and Relativistic Gravity"**, Nobel Lecture, December 8, 1993. Link (^); Huse, Russell. **"The Discovery of the Binary Pulsar"**, Nobel Lecture, December 8, 1993. Link (^)

[U] Brady, Patrick. **"Astrophysical Sources of Gravitational Radiation"**. 1999. Link (^)

[V] Belczynski, Chris. **"Double Compact Object Mergers: Short-hard GRBs and Gravitational-wave Signals"**. 2007. Link (^)

[W] Dent, Thomas. **"Searching for Inspiraling and Merging Binaries in LIGO-Virgo Data"**. 2011. Link (^)

[X] Belczynski, Chris. **"Double Black Holes: Recent Observations and Predictions"**. March 24, 2011. Link (^)

[Y] Brown, Duncan. **"Searches for Gravitational Waves from the Inspiral of Binary Neutron Stars and Black Holes"**. April 13, 2008. Link (^).

[Z] Gondek-Rosinska, Dorota. **"Perspective of Discovering Gravitational Waves from Astrophysical Sources"**. 2011. Link (^)

[AA] Nikhef, Jo van den Brand. **"Gravitational Wave Detection"**. June 3, 2009. Link (^)

[AB] Coward; Lilley; Howell; Burman; Blair. **"The 'Probability Event Horizon' for Neutron Star Merger Detection with Advanced LIGO"**. 2004. Link (^)

[AC] Corvino; Ferrari; Marassi; Schneider. **"Compact Binaries Detection Rates from Gravitational Wave Interferometers: Comparison of Different Procedures"**. June 18, 2012. Link (^)

[AD] Waldman, Samuel. **"Status of LIGO at the Start of the Fifth Science Run"**. June 2006. Link (^)

[AE] The LIGO Scientific Collaboration and The Virgo Collaboration. **"Sensitivity Achieved by the LIGO and Virgo Gravitational Wave Detectors during LIGO's Sixth and Virgo's Second and Third Science Runs"**. March 15, 2012. Link (^)

[AF] Rolland, L. **"The Status of Virgo"**. January 2009. Link (^)

[AG] Fafone, Viviana. **"VIRGO: Where We Come From, Where We Are Going"**. June 7, 2011. Link (^)

[AH] Strain, Ken. **"The Status of GEO600"**. July 2007. Link (^)

[AF] Che, Wujun; Paul, Jean-Claude; Zhang, Xiaopeng. **"Lines of Curvature and Umbilical Points for Implicit Surfaces"**. April 16, 2007. Link (^)

[AG] Kremer; Devecchi. **"Thermodynamics and Kinetic Theory of Relativistic Gases in 2-D Cosmological Models"**. February 7, 2002. Link (^)

[AH] Belongie, Serge. **"'Rodrigues' Rotation Formula"**. Mathworld, Wolfram. Link (^)

[AI] Reiss; Macri; Casertano; Lampeitl; Ferguson; Filippenko; Jha; Li; Chornock. **"A 3% Solution: Determining the Hubble Constant with the Hubble Space Telescope and Wide Field Camera"**. March 10, 2011. Link (^)

[AJ] This research has made use of the NASA/IPAC Extragalactic Database (NED) which is operated by the Jet Propulsion Laboratory, California Institute of Technology, under contract with the National Aeronautics and Space Administration. Link (^)

[AK] Gamow, George. **"The Creation of the Universe"**. Mineola, N.Y: Dover Publications, 2004.

[AL] Hubble, Edwin. **"A Relation Between Distance and Radial Velocity Among Extra-Galactic Nebulae"**. January 17, 1929. Link (^)

[AM] Mirabel, Felix; Rodriguez, Luis. **"Sources of Relativistic Jets in the Galaxy"**. February 4, 1999. Link (^)

[AN] Riess; Strolger; Casertano; Ferguson; Mobasher; Gold; Challis; Filippenko; Jha; Li; Tonry; Foley; Kirshner; Dickinson; MacDonald; Eisenstein; Livio; Younger; Xu; Dahlen; Stern. **"New Hubble Space Telescope Discoveries of Type Ia Supernovae at z ≥ 1: Narrowing Constraints on the Early Behavior of Dark Energy"**. December 20, 2006. Link (^)

[AO] Jarosik; Bennett; Dunkley; Gold; Greason; Halpern; Hill; Hinshaw; Kogut; Komatsu; Larson; Limon; Meyer; Nolta; Odegard; Page; Smith; Spergel; Tucker; Weiland; Wollack; Wright. **"Seven-Year Wilkinson Microwave Anisotropy Probe (WMAP1) Observations: Sky Maps, Systematic Errors, and Basic Results"**. January 26, 2010. Link (^)

[AP] **"Encyclopedia of astronomy and astrophysics"**. Bristol Philadelphia London New York: Institute of Physics Pub. Nature Pub. Group, 2001.

[AQ] Tacconi; Genzel; Neri; Cox; Cooper; Shapiro; Bolatto; Bouché; Bournaud; Burkert; Combes; Comerford; Davis; Förster Schreiber; Garcia-Burillo; Gracia-Carpio; Lutz; Naab; Omont; Shapley; Sternberg; Weiner. **"High molecular gas fractions in normal massive star-forming galaxies in the young Universe"**. December 22, 2009. Link (^)

[AR] Driver, Simon. **"Hubble Deep Fever: A faint galaxy diagnosis"**. February 26, 1998. Link (^)

[AS] Ohio University. **"Discovery Of Giant X-Ray Disk Sheds Light On Elliptical Galaxies"**. December 19, 2002. Link (^)

[AT] Sarazin, Craig; **"X-ray Emission from Elliptical Galaxies"**. December 5, 1996. Link (^)

[AU] Dekel; Birnboim; Engel; Freundlich; Goerdt; Mumcuoglu; Neistein; Pichon; Teyssier; Zinger. **"Cold streams in early massive hot haloes as the main mode of galaxy formation"**. January 16, 2009. Link (^)

[AV] Harvard-Smithsonian Center for Astrophysics. **"Strange new 'species' of ultra-red galaxy discovered"**. ScienceDaily, December 1, 2011. Web. 14 Jul. 2012. Link (^)

[AW] NASA. **"Hubble Finds Hundreds of Young Galaxies in Early Universe"**. April 2006. Link (^)

[AX] Smithsonian Astrophysical Observatory. **"Mysterious Red Galaxies"**. December 9, 2011. Link (^)

[AY] Marel, Roeland; Dokkum, Pieter. **"Dynamic models of elliptical galaxies in z=0.5 clusters: I. Data-model comparison and evolution of galaxy rotation"**. November 17, 2006. Link (^)

[AZ] Kashlinsky; Atrio-Barandela; Kocevski; Ebeling. **"A measurement of large-scale peculiar velocities of clusters of galaxies: technical details"**. February 4, 2009. Link (^)

[BA] Clayton, D. (1983). **"Principles of Stellar Evolution and Nucleosynthesis"**. Chicago: University of Chicago Press.

[BB] Lehnert; Nesvadba; Cuby; Swinbank; Morris; Clement; Evans; Bremer; Basa. **"Spectroscopic Confirmation of a Galaxy at Redshift z=8.6"**. October 20, 2010. Link (^)

[BC] Fixsen. **"The Temperature of the Cosmic Microwave Background"**. November 30, 2009. Link (^)

[BD] Images are credited to NASA/WMAP Science Team. **"WMAP Calibration"**. Link (^). **"Three-Year WMAP View of Early Universe"**. Link (^). **"WMAP Resolves the Universe"**. Link (^)

[BE] Shovkovy, Igor. **"Transport Properties of Stellar Quark Matter"**. September 25, 2008. Link (^)

[BF] Bowers, Jeffrey. **"Color Superconducting Phases of Cold Dense Quark Matter"**. 1998. Link (^)

[BG] J. Beringer (Particle Data Group), J. Phys. D**86**, 010001 (2012). Link (^)

[BH] Totani, Tomonori; Yoshii, Yuzuru. **"Does the Number Density of Elliptical Galaxies Change at z < 1?"**. May 20th, 1998. Link (^)

[BI] Bennett, C. L.; Hill, R. S.; Hinshaw, G.; Larson, D.; Smith, K. M.; Dunkley, J.; Gold, B.; Halpern, M.; Jarosik, N.; Kogut, A.; Komatsu, E.; Limon, M.; Meyer, S. S.; Nolta, M. R.; Odegard, N.; Page, L.; Spergel, D. N.; Tucker, G. S.; Weiland, J. L.; Wollack, E.; Wright, E. L. **"Seven-Year Wilkinson Microwave Anisotropy Probe (WMAP) Observations: Are There Cosmic Microwave Background Anomalies?"**. January 3rd, 2011. Link (^)

[BJ] Hoftuft, J.; Eriksen, H. K.; Banday, A. J.; Gorski, K. M.; Hansen, F. K.; Lilje, P. B.. **"Increasing Evidence for Hemispherical Power Asymmetry in the Five-Year WMAP Data"**. April 20th, 2009. Link (^)

[BK] NASA/Goddard/A. Kashlinsky, et al. **"Mysterious Cosmic 'Dark Flow' Tracked Deeper into Universe"**. Link (^)

[BL] Turnbull, Stephen J.; Hudson, Michael J.; Feldman, Hume A.; Hicken, Malcolm; Kirshner, Robert P.; Watkins, Richard. **"Cosmic flows in the nearby universe from Type Ia Supernovae"**. November 7th, 2011. Link (^)

[BM] **"The Nobel Prize in Physics 2011"**. Nobelprize.org. Accessed November 4th, 2012. Link (^)

[BN] Jarosik, N.; Bennett, C. L.; Dunkley, J.; Gold, B.; Greason, M. R.; Halpern, M.; Hill, R. S.; Hinshaw, G.; Kogut, A.; Komatsu, E.; Larson, D.; Limon, M.; Meyer, S. S.; Nolta, M. R.; Odegard, N.; Page, L.; Smith, K. M.; Spergel, D. N.; Tucker, G. S.; Weiland, J. L.; Wollack, E.; Wright, E. L.. **"Seven-Year Wilkinson Microwave Anisotropy Probe (WMAP) Observations: Sky Maps, Systematic Errors and Basic Results"**. January 26th, 2010. Link (^)

[BO] Hogg, David. **"Distance Measures in Cosmology"**. December 16th, 2000. Link (^)

[BP] Mahdavi, Andisheh; Hoekstra, Henk; Babul, Arif; Balam, David; Capak, Peter. **"A Dark Core in Abell 520"**. February 10th, 2007. Link (^)

[BQ] NASA's Chandra X-ray Observatory. "**NASA Finds Direct Proof of Dark Matter**". August 21st, 2006. Link (^)

[BR] Lee, Jounghun; Komatsu, Eiichiro. **"Bullet Cluster: A Challenge to ΛCDM Cosmology"**. May 22nd, 2010. Link (^)

[BS] Narayan, Ramesh; Bartelmann, Matthias. **"Lectures on Gravitational Lensing"**. 1995. Link (^)

[BT] He, Ping; Zhang, Yuan-Zhong. **"Modelling the Number Counts of Early-Type Galaxies by Pure Luminosity Evolution"**. February 17th, 1998. Link (^)

[BU] Colless, Matthew; Ellis, Richard; Taylor, Keith; Hook, Richard. **"The LDSS Deep Redshift Survey"**. November 14th, 1989. Link (^)

[BV] Driver, Simon; Couch, Warrick. **"The Inferred Redshift Distribution of the Faint Blue Galaxy Excess"**. July 20th, 1996. Link (^)

[BW] Roche, N.; Ratnatunga, K.; Griffiths, R. E.; Im, M. **"Angular Sizes of the Faint Blue Galaxies"**. July 15th, 1996. Link (^)

[BX] Colless, M.; Schade, D.; Broadhurst, T. J.; Ellis, R. S. **"High-Resolution Imaging of Faint Blue Galaxies"**. September 13th, 1993. Link (^)

[BY] Broadhurst, T. J.; Ellis, R. S.; Shanks, T. **"The Durham/Anglo-Australian Telescope Faint Galaxy Redshift Survey"**. July 14th, 1988. Link (^)

[BZ] Glazebrook, K.; Ellis, R.; Colless, M.; Broadhurst, T.; Allington-Smith, J.; Tanvir, N. **"A Faint Galaxy Redshift Survey to B = 24"**. March 8th, 1995. Link (^)

[CA] Loveday, Jon. **"The Local Space Density of Dwarf Galaxies"**. May 19th, 1997. Link (^)

[CB] **"Correlation Between Absolute Magnitude and Diameter"**. Link (^). HOLMBERG, E., Ark. Astr. 3, 387 = Uppsala astr. Obs. Medd., No. 148 (1964).

[CC] Weijmans, Anne-Marie; Bower, Richard G.; Geach, James E.; Swinbank, A. Mark; Wilman, R. J.; Zeeuw, P. T. de; Morris, Simon L. **"Dissecting the Lyman-α emission halo of LAB1"**. November 18th, 2009. Link (^)

[CD] Ouchi, Masami; Ono, Yoshiaki; Egami, Eiichi; Saito, Tomoki; Oguri, Masamune; McCarthy, Patrick J.; Farrah, Duncan; Kashikawa, Nobunari; Momcheva, Ivelina; Shimasaku, Kazuhiro; Nakanishi, Kouichiro; Furusawa, Hisanori; Akiyama, Masayuki; Dunlop, James S.; Mortier, Angela M. J.; Okamura, Sadanori; Hayashi, Masao; Cirasuolo, Michele; Dressler, Alan; Iye, Masanori; Jarvis, Matt. J.; Kodama, Tadayuki; Martin, Crystal L.; McLure, Ross J.; Ohta, Kouji; Yamada, Toru; Yoshida, Michitoshi. **"Discovery of a Giant Ly-α Emitter Near the Reionization Epoch"**. February 21st, 2009. Link (^)

[CE] Mehrtens, Nicola; Romer, A. Kathy; Hilton, Matt; Lloyd-Davies, E. J.; Miller, Christopher J.; Stanford, S. A.; Hosmer, Mark; Hoyle, Ben; Collins, Chris A.; Liddle, Andrew R.; Viana, Pedro T. P.; Nichol, Robert C.; Stott, John P.; Dubois, E. Naomi; Kay, Scott T.; Sahlén, Martin; Young, Owain; Short, C. J.; Christodoulou, L.; Watson, William A.; Davidson, Michael; Harrison, Craig D.; Baruah, Leon; Smith, Mathew; Burke, Claire; Mayers, Julian A.; Deadman, Paul-James; Rooney, Philip J.; Edmondson, Edward M.; West, Michael; Campbell, Heather C.; Edge, Alastair C.; Mann, Robert G.; Sabirli, Kivanc; Wake, David; Benoist, Christophe; da Costa, Luiz; Maia, Marcio A. G.; Ogando, Ricardo. **"The XMM Cluster Survey: optical analysis methodology and the first data release".** June 2012.

[CF] The scientific results reported in this article are based in part on observations made by the Chandra X-ray Observatory

[CG] Hopkins, Philip F.; Croton, Darren; Bundy, Kevin; Khochfar, Sadegh; Bosch, Frank van den; Somerville, Rachel S.; Wetzel, Andrew; Keres, Dusan; Hernquist, Lars; Stewart, Kyle; Younger, Joshua D.; Genel, Shy; Ma, Chung-Pei. **"Mergers in ΛCDM: Uncertainties in Theoretical Predictions and Interpretations of the Merger Rate".** June 2010. Link (^)

[CH] Conselice, Christopher J.; Yang, Cui; Bluck, Asa F. L. **"The Structures of Distant Galaxies - III: The Merger History of over 20,000 Massive Galaxies at z < 1.2".** December 17th, 2008. Link (^)

[CI] Lopez-Sanjuan, Carlos; Balcells, Marc; Perez-Gonzalez, Pablo G.; Barro, Guillermo; Garcıa-Dabo, Cesar Enrique; Gallego, Jesus; Zamorano, Jaime. **"The Galaxy Major Merger Fraction to z~1".** February 23rd, 2009. Link (^)

[CJ] Lotz, Jennifer; Jonsson, Patrik; T.J. Cox; Croton, Darren; Primack, Joel; Somerville, Rachel; Stewart, Kyle. **"Astronomers Pin Down Galaxy Collision Rate".** October 27th, 2011. Link (^)

[CK] Toft, S.; Dokkum, P. van; Franx, M.; Thompson, R. I.; Illingworth, G. D.; Bouwens, R. J.; Kriek, M. **"Distant Red Galaxies in the Hubble Ultra Deep Field".** November 16th, 2004. Link (^)

[CL] Conselice, C. J.; Bluck, A.F.L.; Ravindranath, S.; Mortlock, A.; Koekemoer, A.; Buitrago, F.; Grützbauch, R.; Penny, S. **"The Tumultuous Formation of the Hubble Sequence at z > 1 Examined with HST/WFC3 Observations of the Hubble Ultra Deep Field".** May 12th, 2011. Link (^)

[CM] Conselice, Christopher J.; Bershady, Matthew A.; Dickinson, Mark; Papovich, Casey. **"A Direct Measurement of Major Galaxy Mergers a z ≤3".** June 5th, 2003. Link (^)

[CN] XENON100 Collaboration: Aprile, E.; Arisaka, K.; Arneodo, F.; Askin, A.; Baudis, L.; Behrens, A.; Bokeloh, K.; Brown, E.; Bruch, T.; Bruno, G.; Cardoso, J. M. R.; Chen, W.T.; Choi, B.; Cline, D.; Duchovni, E.; Fattori, S.; Ferella, A. D.; Gao, F.; Giboni, K.L.; Gross, E.; Kish, A.; Lam, C. W.; Lamblin, J.; Lang, R. F.; Levy, C.; Lim, K. E.; Lin, Q.; Lindemann, S.; Lindner, M.; Lopes, J. A. M.; Lung, K.; Undagoitia, T. Marrodan; Mei, Y.; Fernandez, A. J. Melgarejo; Ni, K.; Oberlack, U.; Orrigo, S. E. A.; Pantic, E.; Persiani, R.; Plante, G.; Ribeiro, A. C. C.; Santorelli, R.; Santos, J. M. F. dos; Sartorelli, G.; Schumann, M.; Selvi, M.; Shagin, P.; Simgen, H.; Teymourian, A.; Thers, D.; Vitells, O.; Wang, H.; Weber, M.; Weinheimer, C. **"Dark Matter Results from 100 Live Days of XENON100 Data".** September 7th, 2011. Link (^)

[CO] XENON100 Collaboration. **"Dark Matter Results from 225 Live Days of XENON100 Data".** July 25th, 2012. Link (^)

[CP] Lotz, Jennifer M.; Jonsson, Patrik; Cox, T.J.; Primack, Joel R. **"Galaxy Merger Morphologies and Timescales from Simulations of Equal-Mass Gas-Rich Disk Mergers".** May 8th, 2008. Link (^)

[CQ] Lotz, Jennifer; Jonsson, Patrik; T.J. Cox; Croton, Darren; Primack, Joel; Somerville, Rachel; Stewart, Kyle. **"The Major and Minor Galaxy Merger Rates at z < 1.5".** August 10th, 2011. Link (^)

[CR] Hsieh, B. C.; Yee, H. K. C.; Lin, H.; Gladders, M. D.; Gilbank, D. G. **"Pair Analysis of Field Galaxies from the Red-Sequence Cluster Survey".** April 10th, 2008. Link (^)

[CS] Xu, C. Kevin. **"NIR/Optical Selected Local Mergers - Spatial Density and sSFR Enhancement".** May 4th, 2012. Link (^)

[CT] Edwards, Louise O.V.; Fadda, Dario. **"A Multi-Wavelength Analysis of Spitzer Selected Coma Cluster Galaxies: Star Formation Rates and Masses".** September 14th, 2011. Link (^)

[CU] Churchill, Chris. **"Mg II Absorbers: An On-line Review 'Paper'".** December 1999. Link (^)

[CV] Evans, Jessica L.; Churchill, Christopher W.; Murphy, Michael T. **"The Redshift Distribution of Intervening Weak MgII Quasar Absorbers and a Curious Dependence on Quasar Luminosity".** Draft: July 3rd, 2012. Link (^)

[CW] Dietrich, M.; Hamann, F.; Appenzeller, I.; Vestergaard, M. **"FeII/MgII Emission-Line Ratio in High-Redshift Quasars".** June 27th, 2003. Link (^)

[CX] Rosa, Gisella De; Decarli, Roberto; Walter, Fabian; Fan, Xiaohui; Jiang, Linhua; Kurk, Jaron; Pasquali, Anna; Rix, Hans-Walter. **"Evidence for Non-Evolving FeII/MgII Ratios in Rapidly Accreting Z~6 QSOs".** June 23rd, 2007. Link (^)

[CY] Jiang, Linhua; Fan, Xiaohui; Vestergaard, Marianne; Kurk, Jaron D.; Walter, Fabian; Kelly, Brandon C.; Strauss, Michael A. **"Gemini Near-Infrared Spectroscopy of Luminous z~6 Quasars: Chemical Abundances, Black Hole Masses and MgII Absorption".** July 11th, 2007. Link (^)

[CZ] Maiolino, R.; Juarez, Y.; Mujica, R.; Nagar, N.; Oliva, E. **"Early Star Formation Traced by the Highest Redshift Quasars".** September 8th, 2003. Link (^)

[DA] Wei, Hao. **"Observational Constraints on Cosmological Models with the Updated Long Gamma-Ray Bursts".** August 16th, 2010. Link (^)

[DB] Cardone, V.F.; Capozziello, S.; Dainotti, M.G. **"An Updated Gamma Ray Bursts Hubble Diagram".** July 27th, 2009. Link (^)

[DC] Wei, Hao; Zhang, Shuang Nan. **"Reconstructing the Cosmic Expansion History up to Redshift z = 6.29 with the Calibrated Gamma-Ray Bursts".** August 31st, 2009. Link (^)

[DD] Collazzi, Andrew C.; Schaefer, Bradley E.; Goldstein, Adam; Preece, Robert D. **"A Significant Problem with Using the Amati Relation for Cosmological Purposes".** December 19th, 2011. Link (^)